Design, Manufacturing, and Control of Soft and Soft/Rigid Hybrid Pneumatic Robotic Systems

Hee Doo Yang

Dissertation submitted to the faculty of the Virginia Polytechnic Institute and State University in partial fulfillment of the requirements for the degree of

Doctor of Philosophy
In
Mechanical Engineering

Alan T. Asbeck, Chair
Andrew Kurdila
Reza Mirzaeifar
James Hanna

March 25, 2019
Blacksburg, Virginia

Keywords: manufacturing process, soft robots, soft actuators, soft manipulator, soft pneumatic actuators, textile actuators, bellows actuators

Design, Manufacturing, and Control of Soft and Soft/Rigid Hybrid Pneumatic Robotic Systems

Hee Doo Yang

(ABSTRACT)

Soft robotic systems have recently been considered as a new approach that is in principle better suited for tasks where safety and adaptability are important. That is because soft materials are inherently compliant and resilient in the event of collisions. They are also lightweight and can be low-cost; in general, soft robots have the potential to achieve many tasks that were not previously possible with traditional robotic systems.

In this paper, we propose a new manufacturing process for creating multi-chambered pneumatic actuators and robots. We focus on using fabric as the primary structural material, but plastic films can be used instead of textiles as well. We introduce two different methods to create layered bellows actuators, which can be made with a heat press machine or in an oven. We also describe origami-like actuators with possible corner structures. Moreover, the fabrication process permits the creation of soft and soft/rigid hybrid robotic systems, and enables the easy integration of sensors into these robots. We analyze various textiles that are possibly used with this method, and model bellows actuators including operating force, restoring force, and estimated geometry with multiple bellows. We then demonstrate the process by showing a bellows actuator with an embedded sensor and other fabricated structures and robots.

We next present a new design of a multi-DOF soft/rigid hybrid robotic manipulator. It contains a revolute actuator and several roll-pitch actuators which are arranged in series.

To control the manipulator, we use a new variant of the piece-wise constant curvature (PCC) model. The robot can be controlled using forward and inverse kinematics with embedded inertial measurement units (IMUs). A bellows actuator, which is a subcomponent of the manipulator, is modeled with a variable-stiffness spring, and we use the model to predict the behavior of the actuator. With the model, the roll-pitch actuator stiffnesses are measured in all directions through applying forces and torques. The stiffness is used to predict the behavior of the end effector. The robotic system introduced achieved errors of less than 5% when compared to the models, and positioning accuracies of better than 1cm.

Design, Manufacturing, and Control of Soft and Soft/Rigid Hybrid Pneumatic Robotic Systems

Hee Doo Yang

(GENERAL AUDIENCE ABSTRACT)

Future robotic systems are expected to deal with many tasks in real-world environments. The natural environment is highly unpredictable and unstructured, making manipulation and locomotion challenging for robots. Robots need to rely on adaptability, reconfigurability, and safety. Soft robotic systems have recently been considered as a new approach that is in principle better suited for tasks where safety and adaptability are important. That is because soft materials are inherently compliant and resilient in the event of collisions. They are also lightweight and can be low-cost; in general, soft robots have the potential to achieve many tasks that were not previously possible with traditional robotic systems.

In this paper, we propose a new manufacturing process for creating multi-chambered pneumatic actuators and robots. We focus on using fabric as the primary structural material, but plastic films can be used instead of textiles as well. We introduce two different methods to create layered bellows actuators, which can be made with a heat press machine or household iron, or in an oven. We also describe origami-like actuators with possible corner structures. Moreover, the fabrication process permits the creation of soft and soft/rigid hybrid robotic systems, and enables the easy integration of sensors into these robots. We analyze various textiles that can be used with this method, and make models of bellows actuators including their operating force, restoring force, and estimated geometry with

multiple bellows. We then demonstrate the process by showing a bellows actuator with an embedded sensor and other fabricated structures and robots.

We next present a new design of a multi-DOF soft/rigid hybrid robotic manipulator. It contains a revolute actuator and several roll-pitch actuators which are arranged in series. To control the manipulator, we use a new variant of the piece-wise constant curvature (PCC) model. The robot can be controlled using forward and inverse kinematics with embedded inertial measurement units (IMUs). A bellows actuator, which is a subcomponent of the manipulator, is modeled with a variable-stiffness spring, and we use the model to predict the behavior of the actuator. With the model, the roll-pitch actuator stiffnesses are measured in all directions through applying forces and torques. The stiffness is used to predict the behavior of the end effector.

Acknowledgments

Foremost, I would like to express my sincere gratitude to my advisor Prof. Alan T. Asbeck for the continuous support of my PhD study and research, for his patience, motivation, enthusiasm, and immense knowledge. Over the past four years, I have received invaluable guidance and inspiration from Prof. Alan Asbeck. The rigorous approach toward research and critical thinking I learned from him will provide lasting benefits throughout my future career. I could not have imagined having a better advisor and mentor for my PhD study. I am greatly honored to be his first PhD alumnus from the Assistive Robotics Laboratory (ARL).

Besides my advisor, I would like to thank the rest of my thesis committee: Prof. Andrew Kurdila, Prof. Reza Mirzaeifar, and Prof. James Hanna, for their encouragement, insightful comments, and professional suggestions.

I thank my labmates in Assistive Robotics Laboratory (ARL): Tim Pote, Taylor Pesek, Athulya Simon, Brandyn Greczek, Evan Wood, Mehdi Alemi, Hubert Kim, Hani Awni, and Jack Geissinger for all the fun we have had in the last four years.

Finally, I would like to thank my parents Sang Yong Yang and Mi Hyun Park for their love, prayers, caring and sacrifices for educating and preparing me for my future. My parents always trusted and supported my decision in every step of my life. Also, I express my thanks to my sister Ah Jung Yang for her support and valuable prayers. I believe she will achieve invaluable research in media communication during her PhD degree.

Contents

List of Figures

Chapter 1

Introduction

Most robots are used to serve tasks such as automation in manufacturing. For industrial applications, maximizing productivity has been the primary consideration, so traditional robots have been studied to achieve improving accuracy, precision, and efficiency. In order to accomplish the requirements, the robots have been mostly designed and built from rigid materials since the materials are easily modeled and constructed with discrete joints. The robots have accomplished many tasks using advanced theories including various control methods, design, and motion planning [1], [2]. Despite their benefits, traditional robots often have limited adaptability for safe interaction with humans or deployment in various environments. That is because of their properties, which can include heavy weights, large sizes, and rigidity.

At the present, future robotic systems are expected to carry out complicated tasks in complex and changing environments or to work with humans interacting more safely. It is also anticipated that robots possibly achieve tasks that were not previously possible using traditional robots, including minimally invasive surgery, mobility in unstructured environments, and grasping irregular objects. For the required tasks, new approaches have been investigated.

Among many possible solutions, soft robots are an emerging idea in the field of robotics. It is anticipated that soft robots can have resilience in natural environments or allow for safe interaction with humans. This is due in part to the advantages of soft robots, which include being made from deformable materials that enable compliance matching with the environment. The softness can be intended in various ways: soft movement [3], actuation in friendly and natural interactions with humans [4], and applications supported by the bioinspired approach [5]. Its benefits are attractive for researchers to design soft robots. Otherwise, the soft robot presents many challenges as well. The softness may cause control issues such as low positioning accuracy since the control systems and modeling strategy of the conventional robotic system do not fit for soft-bodied machines. In addition, the materials preclude from using traditional sensors such as a force sensor or an encoder. Therefore, soft robots will require a new design process, a modeling principle, and a control strategy.

Figure 1.1. (A) A untethered soft robot [3]; (B) A fabric-based soft robotic glove for assistance and rehabilitation [4]; (C) A bioinspired actuator with kirigami skins [5].

The field of soft robotics has been focused on researching design processes and modeling principles so far. Current soft actuators and robots are designed with different power sources: pneumatic [6], [7], electrical [8], chemical [9], and cable-driven systems [10]. For example, a robot with an electrical power source can contain shape-memory alloy materials (SMA) in the body, and then it is operated by the deformation of this material when electricity is applied. Alternatively, an actuator, which is controlled by chemical reaction, can contain a poly-hydrogel, and the actuator achieves its motion by the change of mechanical properties of the hydrogel. A third type is a cable driven actuator and a manipulator which often contain soft or rigid structures and origami-like materials in the middle, and then they are operated by pulling or releasing cables.

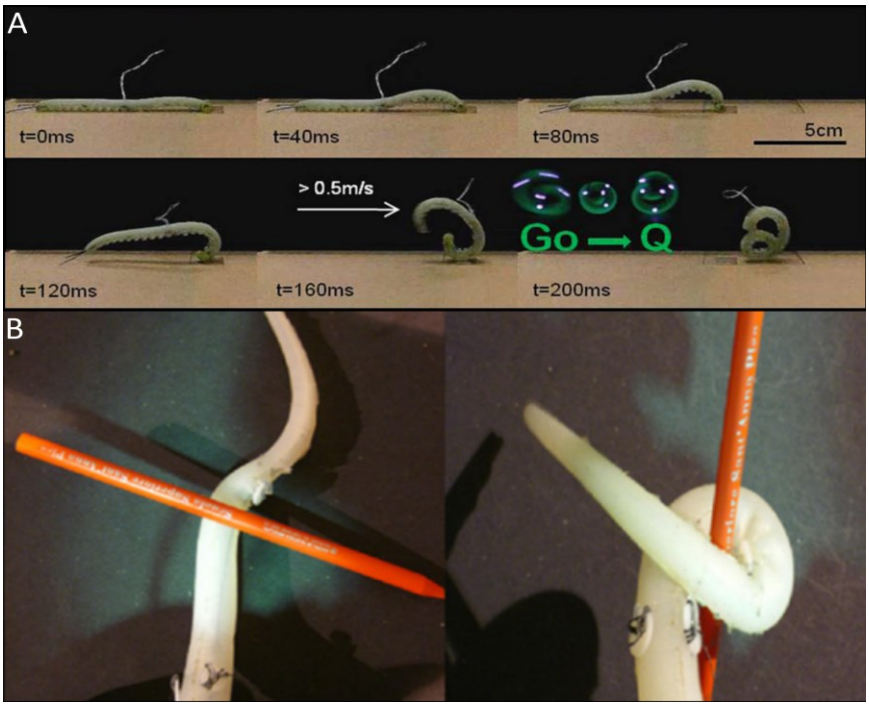

Figure 1.2. (A) A caterpillar-inspired rolling robot [8]; (B) An octopus-bioinspired actuator [10]

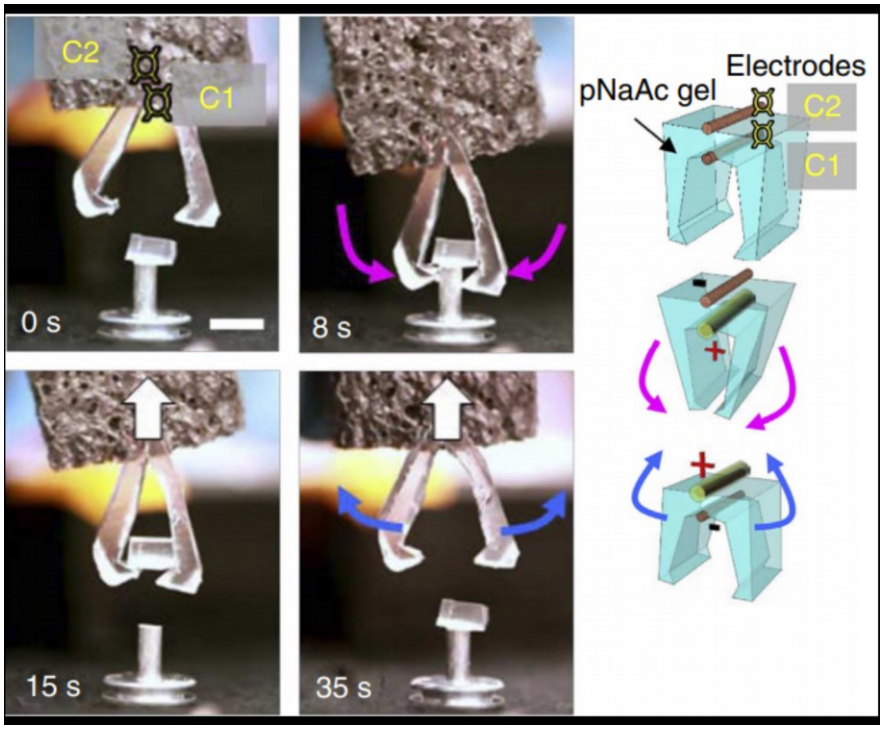

Figure 1.3. A soft actuator with hydrogels [9].

Pneumatic based actuators and robots are common and the most advanced approach in the soft robotics [11]–[13]. The pneumatic actuators are generally made of elastomer-based materials or fabric, and different fabrication processes are required respectively. First, silicone rubber or PDMS are popularly used for soft actuators. Elastomer-based actuators have asymmetrical structures in the body, including extensible or inextensible layers. The extensible layers contain multiple inflatable chambers interconnected via a single air channel. The chambers increase their volume, stretch outer shells, and then change the length of the layer when it is pressurized. Otherwise, the inextensible layers are non-stretchable but flexible, so the actuator bends due to the length difference of two layers. The elastomer actuator and robots can also be designed to provide different operating modes; expansion [14], contraction [15], and twist [16]. As follows

many possible designs, the robots are often researched for a soft robotic gripper [13], a biomimetic manipulator [17], and an endoscope soft manipulator for invasive surgery [18]. A soft robotic gripper can grasp non-uniform or delicate objects such as fruits. A gripper can also contain soft textile sensors, and then it senses touch, pressure, and temperature that cannot be considered by the traditional robots [19]. The biomimetic manipulators and the endoscope manipulator can offer novel approach to solve the limitation in medical robots and industrial robots. That is because the soft manipulator can have high dexterity.

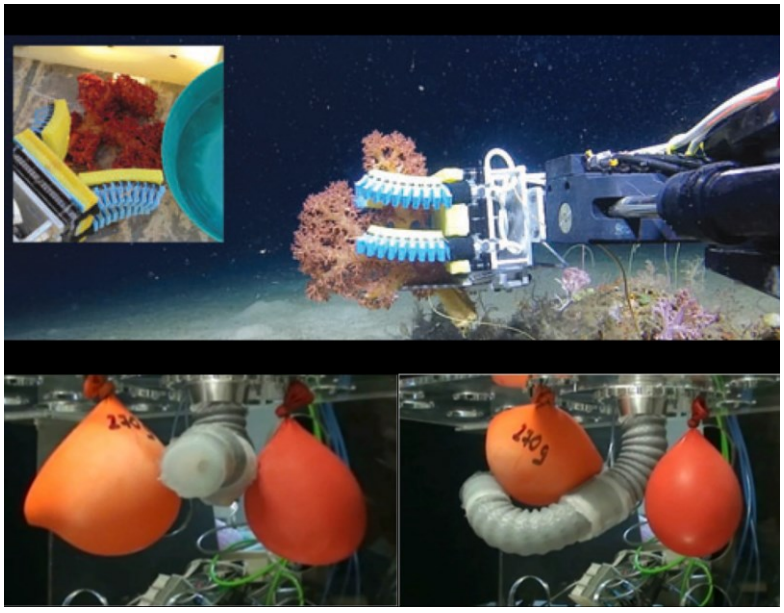

Figure 1.4. (A) A soft pneumatic gripper [13]; (B) A soft manipulator for invasive surgery [18].

Custom 3D mold fabrication processes are generally used to build elastomer actuators [12]. Notably, the open source fabrication method called the Pneu-net approach has been introduced, and it has been widely used for the elastomer-based actuators and robots. The fabrication method needs 3D molds, which are made by a 3D printer, and it requires several steps to construct air-impermeable actuators. First, pour elastomer in the molds, cure and demold a top layer. Next, we need to fill elastomer into the base mold and cure the two parts together. Additionally, a different manufacturing method is developed using a 3D printer to construct an elastomer-based actuator as well.

Inflatable robots and actuators are also made of fabric or plastic sheets instead of elastomers [20]–[23]. Fabric-based actuators are generally designed and fabricated with a pouch-like actuator. A pouch-like actuator is made of plastic film or fabric coated with TPU film (Thermoplastic polyurethane), which are laminated together using a heat-sealing process. The heat-sealing process is very simple and fast, but the method cannot make 3D structures. Therefore, the actuators are confined to a 2D planar structure. They are connected in a series of pouch chambers for contractile behavior [22], they are folded for extension operation principle [4], or the actuator changes the geometry itself by a pneumatic hinge mechanism for bending motion [24]. In addition, origami-like structures can be enclosed in the pouch actuator [25], [26]. The structures are performed as a skeleton of the actuator and prevent buckling when negative pressure is applied. Due to this, the actuators with the origami structures can provide a high contraction ratio and large forces under vacuum. An actuator with fabric or plastic film is usually utilized for applications that require high contraction or expansion motion. It is also compact and can have variable

geometry, so different motion principles achieve novel design approaches for robotic applications to provide torque and force [27], [28].

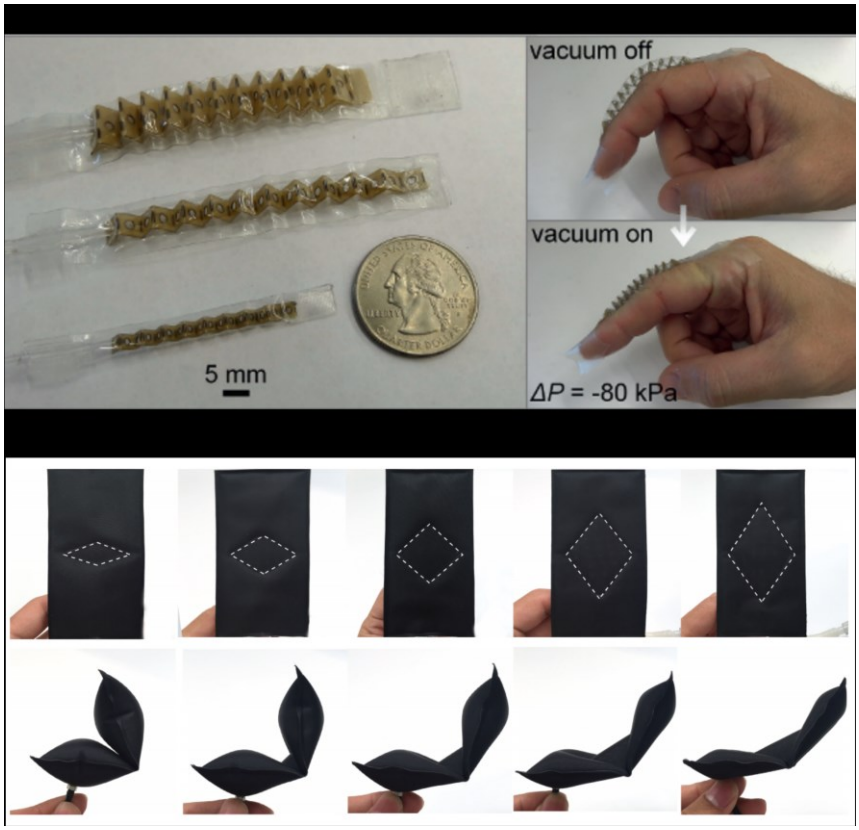

Figure 1.5. (A) A pouch actuator made of plastic film with an origami like structure [25], [26]; (B) A hinge mechanism of a fabric actuator using different hinge shapes for bending actuation.

Although a soft robot has many advantages as mentioned above, the robotic system has many challenges as well. First, the 3D fabrication process for an elastomer robot is quite simple and easily used for the robot, but it is a very time-consuming process and

requires unnecessary fabrication steps; new molds should be re-designed and fabricated whenever the robot geometry is changed. The method also requires special sensors such as textile sensors since the traditional sensors cannot be used in the method. In addition, the elastomer robot has relatively low force output due to the fact that the robot generally has bending actuation. Therefore, the robot is still limited for small scale applications which is not required large force output.

Next, the fabric or plastic film-based robot is compact, lightweight and has various geometry. However, its different geometry is restricted to a pouch chamber. That is because a fabrication process for the robot is not well developed yet. The robot is also not available to be modeled easily because the geometry of fabric or plastic film is nonstandard and atypical when it is inflated. Due to its challenging disadvantages, the amount of research on this type of robot is relatively lower than research on the elastomer robot.

In addition, even though many applications of soft manipulators are introduced, these manipulators have several challenges. Many soft manipulators are modeled and controlled based on the kinematics of a continuum robotic theory, which estimates the curvature of bending motion to detect the end effectors position. However, the theory is quite complex, so it is relatively difficult to achieve high positioning accuracy. Especially, the pneumatic system has more challenges to control the positioning of the end effector since airflow cannot be controlled accurately and the geometry of the robot body is unpredictable. This being so, we need to study better design and control strategy including a fast and straightforward manufacturing process, merging other materials with the soft robot, and operating the robot with simple kinematics.

In this paper, we focus on using fabric as the primary material for the manufacturing system and robots. In Chapter 2, we introduce a new fabrication method for fabric or plastic film-based actuators and robots. The manufacturing process can be used by a household iron, heat press, or oven. The fabrication process also provides opportunities to integrate a traditional sensor into the soft actuator directly and to include rigid materials. The method offers a possible solution to building small scale robots and large-scale robots as well. To demonstrate the process, we show three applications with a textile bellows actuator. In Chapter 3, among the applications we proposed in Chapter 2, we introduce a multi-DOF modular soft/rigid hybrid robotic manipulator, which is low cost and lightweight. The manipulator has different modules including a roll-pitch actuator, a revolute actuator, and a body actuator. The roll-pitch actuator follows a fixed arc when it is inflated and deflated, so a new variant of the piece-wise constant curvature (PCC) model is made for the geometry of the robot. Using this PCC model with a new variant, the soft manipulator is controlled using forward and inverse kinematics. We model a bellows actuator, which is a subcomponent of a roll-pitch actuator, with a variable-stiffness spring. With the model, we also model the roll-pitch actuator and predict the behavior of the actuator. Additionally, the actuator stiffnesses are measured in all directions to predict the end effector behavior of the manipulator.

1.1 Contributions

In this thesis, we provide the following contributions:

1. Development of a novel manufacturing process that permits the creation of soft and soft/rigid hybrid robotic systems, and permits the easy integration of sensors into these robots.

2. Development of a novel soft roll-pitch actuator and a model of its kinematics.

3. Using this actuator and the kinematic model, development and characterization of a position control system for a robot arm that uses Inertial Measurement Units and a new varient of PCC model to detect the arm's orientation.

4. Modeling and experimental validation of a bellows actuator and a roll-pitch actuator to predict the behavior of a soft/rigid hybrid manipulator.

Chapter 2.

A Layered Manufacturing Approach for Soft and Soft-Rigid Hybrid Robots

2.1 Abstract

We present a fabrication method for designing centimeter-scale inflatable structures with multi-chambers that can include both soft and rigid materials. The method uses a thermoplastic polyurethane (TPU) adhesive film to bond together layers of textiles, plastics, or other materials. The structures are heated and compressed a few layers at a time using a heat press machine, or bonded in an oven all at once. We present two methods for arranging textiles and thermal adhesive film in order to build air-impermeable structures. We also characterize the set of textiles and rigid materials that will work with this process, measuring how strongly the TPU film bonds with them and noting the heat deflection and melting temperatures of the rigid materials. We present methods for including rigid

materials and materials with low heat deflection temperatures into a structure. We also describe how to include corners, where several pieces of material come together at a point, and determine which corner constructions are airtight. We also characterize how different seam widths behave, determine the maximum pressure chambers fabricated with this process can support, and determine the cycle life of actuators built with this process. Finally, we present three examples of robots constructed with textiles and TPU film, including a hybrid soft/rigid robotic manipulator, a soft robot that can roll along the ground, and a robot that can climb inside tubes or other confined spaces.

2.2 Introduction

Soft robotics are becoming increasingly prevalent today, with various applications including soft grippers [13], soft robots [3], exoskeletons [29], and origami robots [30]. Soft robots typically have intrinsic compliance, low cost, and light weight, which can provide some benefits over conventional robotic platforms. Soft robots can have many degrees of freedom (DOF), resilience in the event of collisions, the ability to grasp unknown geometric objects, or allow for safe interaction with humans [31], [32].

Additionally, soft robotic platforms can be constructed from relatively simple fabrication techniques, including molding elastomers or bonding materials with adhesives, as compared to traditional robots which may require machining or connecting components with discrete fasteners. The ability to fabricate robots quickly and easily is beneficial for both rapid prototyping and mass production of robots, as well as potentially allowing home hobbyists to participate in the construction of these robots. Most soft robots are fabricated

by pouring an uncured polymer into custom 3D molds [12], [13], [33], [34], directly printing flexible materials with a 3D printer [35]–[39], or assembling layers of textile or plastic with a heat press or similar device [4], [21]–[23], [40]–[43]. Even though each of these methods has its own benefits and can be a simple and fast process, they all still present opportunities for improvement in the construction of soft robots.

The custom 3D mold fabrication methods are used to make robots out of elastomer based materials such as silicone or PDMS [11], [44]–[48]. These robots use chambers that can stretch with relatively high strains, expanding or contracting in one or more dimensions during inflation or deflation. To construct these hollow chambers that can be inflated, 3D molds must be fabricated for top and bottom sections of the robot separately, and then the sub-components attached together, so the fabrication process requires several repetitions of the cast-cure cycle. Modifying the robot's physical geometry requires redesigning and fabricating the 3D molds, which may be time-consuming.

A 3D printer-based approach has also been developed for robots that inflate and stretch [35]–[39]. The process is simple and faster than a mold-based approach. Despite these benefits, there remain some challenges related to the mechanical properties of the printed materials and the ability of the layers to hold together, potentially leading to low cycle lifetimes.

Both mold-based and 3D printer-based soft robots also present challenges when incorporating sensors, wires, plates for mounting objects, and circuit boards due to the fact that these materials do not stretch while the robot material can and does stretch. To accommodate the difference in strains, intervening layers of material of intermediate

stiffness have been used to avoid stress concentrations and delamination at the soft-rigid interface [35], [49]–[51]. Other groups have developed sensors or wires that can stretch, typically using a liquid metal flowing through narrow channels [49], [52]–[56]. Incorporating these into a soft robot requires additional, complex steps.

A third class of fabrication uses a heat press or similar device to make robots out of thin layers of plastic or coated textiles instead of an elastomer [4], [21]–[23], [40]–[43]. The robots are bonded together through a heat sealing process, by either melting the materials themselves or using a thermal adhesive film. The robots have the same general operational principle as the elastomer based robots. They have small pouches or larger chambers that have the ability to expand or contract. Using this process, pouch-like structured actuators [41], [43], and linear actuators that use zigzag origami structures in a pouch have been developed [57]. Other structures also have been formed but with additional steps to make separate airtight chambers, and another variant uses a sealed chamber inside a containment structure made out of cloth [58], [59]. Additionally, vine robots have been introduced that are made of long tubes of thin plastic [60]–[62] or additional membranes inside of actuators [63]. With just a few exceptions, the majority of the structures built using heat and plastic or adhesive films have only single pouches, with a single chamber of air and two walls.

In this paper we describe a fabricating methodology for soft pneumatic structures using thermoplastic polyurethane (TPU) adhesive film and either textiles or thin sheets of plastic; our work is an example of the third type of fabrication process described above. Our method involves stacking layers of thin, inextensible materials and layers of thermal adhesive film, and bonding them together with a heat press, household iron, or oven. The

resulting structures can have complex, three-dimensional shapes when inflated (Figure 2.1), and additionally can include embedded tubes, electronics, and structural elements. The process allows for rapid fabrication of new designs, and stress concentrations are avoided when interfacing with rigid elements because the robots bend instead of stretch.

While many robots have been made in a related manner, we significantly extend previous work by creating monolithic structures with many layers of material, incorporating rigid structures on both the outside and inside of the robots, and including folds and corners into the robots. Additionally, we present a thorough investigation into the different possible materials that can be used with the process, including measurements of their performance, and describe several systematic ways of creating complex, layered structures that are airtight.

We first provide an overview of our fabrication method (Section 2.3), then present several recipes for assembling layers of structural material and thermal adhesive film to achieve airtight structures. We additionally present how to include rigid structures and corners (Section 2.4). We next present a library of possible materials to use with the process, including measurements of how well they bond with TPU film, and present measurements of different seam widths and the service lifetimes of sample actuators (Section 2.5). We finally present three examples of inflatable robots built with this manufacturing process (Section 2.6) before concluding.

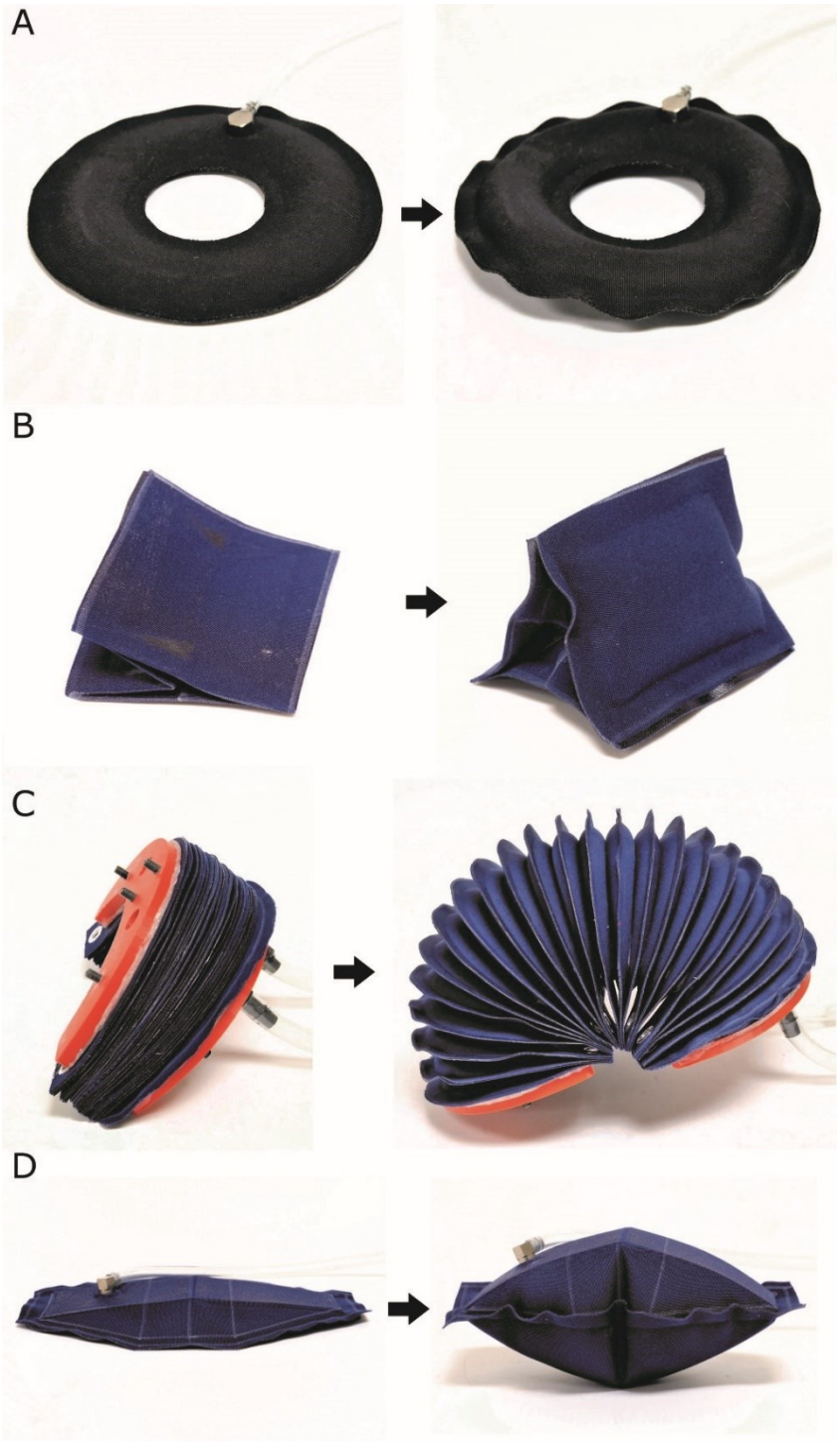

Figure 2.1. Soft actuators made by the manufacturing processes described in this paper, with the uninflated state shown on the left and the inflated state shown on the right. (A) toroid-shaped pouch; (B) chamber in the shape of a triangular prism; (C) bellows structure formed of crescent shapes that curls when inflated; and (D) pouch with rigid plates embedded on the top and bottom surfaces, so as to cause sharp corners at the top, bottom, and sides.

2.3 Overview and Materials

Our method uses layers of a thin structural material including a textile or plastic film interleaved with layers of thermoplastic polyurethane (TPU) film. The fabrication process consists of cutting materials to desired shapes, stacking them, and then bonding them by heating them while applying a compressive force to the stack. In Section 3 we present several specific ways the materials can be stacked to make the resulting structures airtight, describe how long they must be heated to be bonded under various conditions, and also discuss how the materials can be folded prior to being stacked to achieve complex shapes or corners.

Our process is based around an ester-based thermoplastic polyurethane (TPU) film (#HM65-PA, Perfectex LLC.), which is used to both bond the structural layers together and also to make textiles air-impermeable by laminating them with it. We use a 0.1mm thick TPU film which we have found bonds more effectively to textiles than thinner layers of TPU. The 0.1mm thickness is easy to handle, and can be stacked in a few layers if a thicker film is desired.

Besides the TPU film, the robot's structure is primarily composed of a plastic film or textile that gives the robot its shape and strength. In this paper we have used textiles as the structural material, although thin sheets of plastic will work equally well so long as they will bond with the TPU film. We have constructed most of our example chambers and robots out of a medium-weight poplin fabric (65% polyester, 35% cotton, 0.30 mm thick) which provides a good ratio of strength to thickness. In general, a thinner textile

provides more flexibility for the structure, especially at the seams which have two or more layers of textile bonded together, but fabrics that are too thin may not have a high enough tensile strength.

Additional elements can be also incorporated into the structures, such as rigid plates, pneumatic tubing, or electronic circuit boards. The rigid structures can be attached to the exterior of a robot, thereby making hybrid soft-rigid robots. Section 5.3 gives details on the types of rigid materials that work well with this manufacturing process.

2.4 Manufacturing Process Detail

2.4.1 Layered Manufacturing Methods

We present two different methods for arranging layers of textile and TPU film in order to fabricate an airtight robot. These differ in how the layers of textile are coated in thermal adhesive film to make them air-impermeable, and the sequence of how the structures are heated and pressed. These both use a heat press machine or household iron to bond the structures together a few layers at a time. We also describe a third method by which the robots can be bonded together at once in an oven.

The first method (Type I) uses a lamination formed of textile-TPU-textile to make the fabric airtight before subsequent bonding steps. Figure 2.2 (left) shows the steps in preparing the materials and intermediate forms. Large sheets of fabric are first made to be airtight by placing a layer of TPU film in between two layers of fabric, and placing the stack in the heat press machine at 154°C (310°F) for 60 seconds (Figure 2.2A). Note that

this is just above the quoted melting temperature of the TPU film we are using (130-150°C); some other TPU films have lower melting temperatures, and if those were to be used instead, a temperature just above the TPU melting point should be used. Higher temperatures can also be used to reduce the process time, which is limited by the heat transfer through the top layers of textile. After the fabric is laminated, shapes are cut out with a vinyl cutter machine or scissors (Figure 2.2B). A second material preparation step is to bond additional layers of TPU film to the top or bottom of the fabric-TPU-fabric lamination. These are bonded with the heat press machine at 154°C (310°F) for 20 seconds (Figure 2.2C). The resulting intermediate forms (Figure 2.2D) now have the topology TPU-fabric-TPU-fabric-TPU. The non-stick paper that comes with the TPU film prevents the structure from bonding to the heat press when the TPU film is added on the outside. The final shape is then constructed from the bottom up, by placing one of these intermediate forms on the heat press machine, bonding it at 154°C (310°F) for 20 seconds, and then repeating for additional layers in the structure (Figure 2.3, left). The vertical hole in the center of the structures in Figure 2.3 is not shown in Figure 2.2 for clarity; it can be added during the initial steps of the process or can be cut after bonding everything except the end piece.

The iterative process in adding layers is necessary because the heat press machine only applies heat at the top surface, and the heat does not permeate very far into the structure in the allotted time. It is possible to bond a few layers at a time if they are held longer in the heat press machine: three layers works well with a press time of 60 seconds.

The bottom surface of the heat press machine contains a 1cm silicone pad, which conforms to the shape of the structure being bonded, compressing the layers together even if different

parts of the structure are slightly different thicknesses. The silicone pad only accommodates relatively small (<0.5cm) differences in height; if needed, removable spacers of plastic or foam can be placed underneath the lower layers to equalize the height of the structure at the top surface and ensure an equal heat distribution across the top surface. For the structures shown, no additional spacers are needed, but these could be necessary for structures with different numbers of layers in different areas.

With the Type I fabrication method, it is relatively fast to create shapes and bond them because the initial fabric lamination can be done in large sheets, and it requires relatively small amounts of TPU film to hold the different layers together. However, the final structures are not perfectly airtight. As can be seen in Figure 2.3, the thermal adhesive film prevents air from flowing perpendicularly through the fabric, but air can still escape through the fabric itself at the edges of the structure, in between the adhesive layers. This leads to a continuous, slow leak, where a structure similar to the one at the bottom of Figure 2.3 (6cm diameter, 15cm tall, 6 chambers, 5mm wide seams) will deflate in approximately 5 minutes with a load of 10N on top. This equates to a leakage of 12.73mL/hour per centimeter of seam perimeter.

The next fabrication method (Type II) uses a different way of preparing the materials that makes the resulting structures completely airtight (Figure 2.2, right). First, pieces of fabric are coated with TPU film on one side. The fabric is next cut into an "outer" layer with the TPU facing up (2 in Figure 2.2), and an "inner" layer which is flipped upside down so it has the TPU film facing downward (3 in Figure 2.2). The outer layer's outside edge has a diameter of length L3, and it has a hole in it with diameter L1. The inner layer has the same overall shape as the outer layer, but with its outside dimension L2 slightly

smaller than that of the outer layer (L1 < L2 < L3). The combination of the inner and outer layer will form the top or bottom half of a final airtight chamber.

Additional layers of TPU film are ideally also added to the top and bottom of the intermediate structure before continuing with subsequent assembly steps in order to make it of nearly uniform thickness. Specifically, on the top rings of TPU film with inner diameter L2 and outer diameter L3 are placed around the "inner" layer (4 in Figure 2.2), and on the bottom discs of diameter L1 are placed inside the hole in the "outer" layer (1 in Figure 2.2). Since the TPU film is 0.1mm thick and the fabric is 0.3mm thick, 2-3 layers of TPU film should be placed to make the entire structure have a uniform thickness (see cross-section view at the bottom of Figure 2.2). Making these intermediate layers approximately uniform thickness is beneficial because to create the final structure, the intermediate layers will be placed on top of each other, flipping every other one upside down (Figure 2.3, right). If portions of these intermediate layers are much thinner than other parts (with only one layer of fabric and one layer of TPU film), there will not be as much pressure on the thinner portions once they are stacked, leading to poor bonding there. Once the layers have been aligned (1-4 in Figure 2.2), the pieces are clamped together in the heat press machine at 154℃ (310℉) for 60 seconds.

The process thus far results in an intermediate structure which has a continuous layer of TPU film on the interior of the structure. If these intermediate structures are then assembled as in Figure 2.3, flipping every other one upside down, the final structure has a continuous layer of TPU film throughout it, making it completely airtight. Textiles cover the exterior and interior of the structure so that adjacent layers of TPU do not bond to each

other. The Type II process is somewhat slower than the Type I process due to the additional steps in cutting material and arranging it, but the resulting structure is completely airtight.

We also present one additional method for bonding these robots together: instead of using a heat press to bond layers iteratively, the entire structure can be bonded in a single step by baking it in a convection oven. In this method, the structural material and TPU film can be cut and layered in either the Type I or Type II pattern. Then, all of the materials for the entire structure are placed in a large stack, clamped together, and baked in a convection oven at 177°C (350°F) for 15 minutes or more. The baking time can be varied depending on how many layers there are in the structure; 15 minutes was found to work well for structures around 6cm in diameter with around 30 layers. Lower temperatures may also work well for baking, since the melting point of TPU film is 130-150°C, but these were not tested. This last method is the easiest way to build soft robots compared to the previous processes, since all of the bonding can be done in a single step.

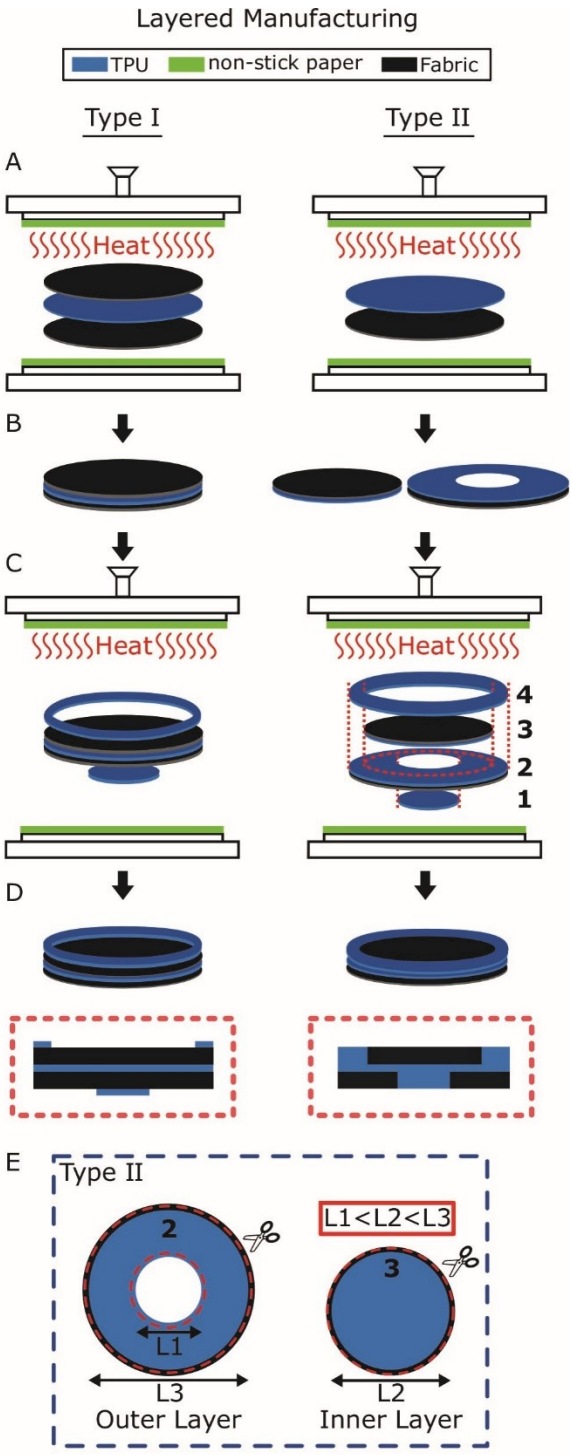

Figure 2.2. Material preparation for the layered manufacturing process. In A and C, a side view is shown of the heat press with materials inside. The heat press is then clamped down to bond the materials under heat and pressure, resulting in the structures in B and D. The materials inside the red boxes in D show a cross-section view of the assembled structures; the textile used is thicker than the TPU film, as drawn. E shows detail about the relative sizes of the different pieces used in the Type II process.

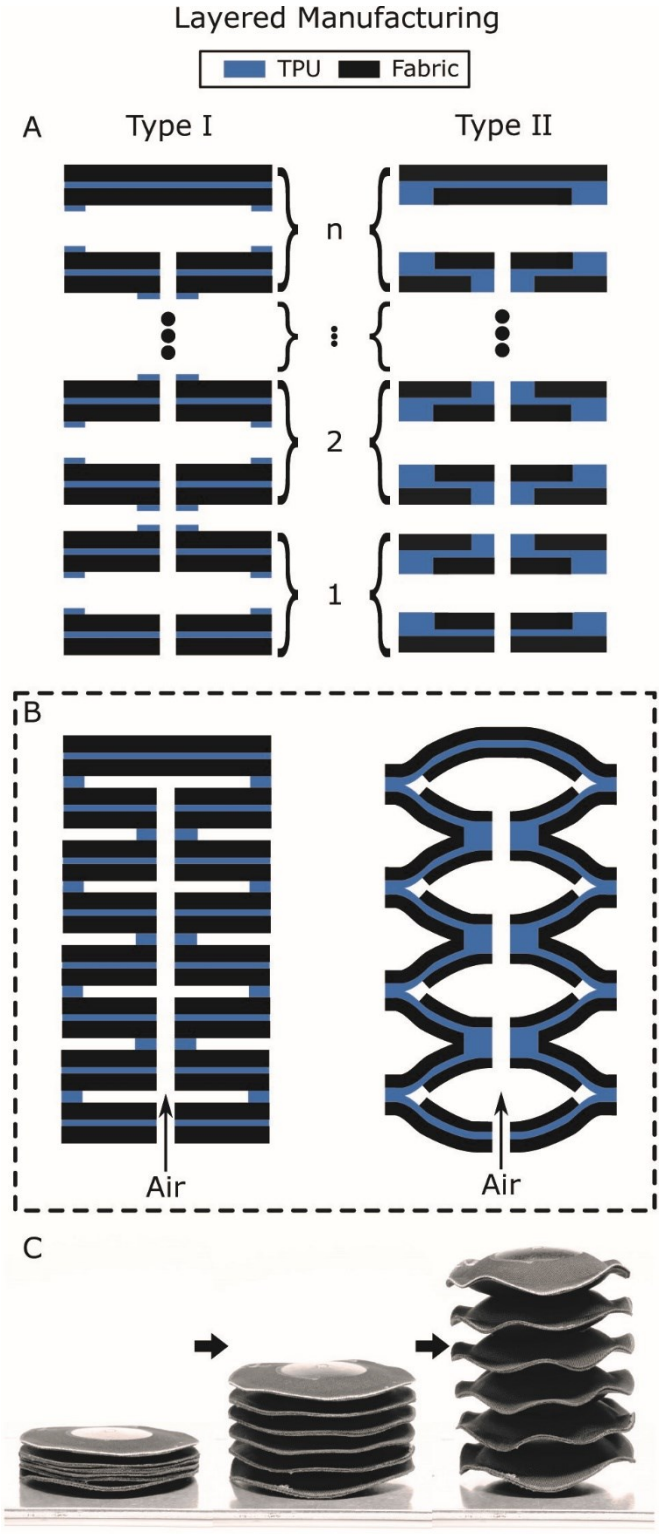

Figure 2.3. (A) Arrangement of the intermediate pieces to create a continuous structure with many smaller, connected chambers. Note that in this figure the structures are shown with a hole in the middle to allow air to pass through; this is not shown in Figures 2.2 or 2.4 for clarity there. (B) Diagram of the assembled actuators made by Type I and II; (C) A sample pneumatic actuator built by any of the types of the layered manufacturing.

2.4.2 Inclusion of rigid surfaces

We can include rigid surfaces at any stage of the manufacturing process. These can be used for a variety of purposes. If bonded to the outside of an inflatable structure, they can be used to connect different modules with fasteners (Figures 2.1C, 2. 10). Rigid body parts can also be used to integrate off-the-shelf sensors into soft robots. For example, a circuit board with IMUs and pressure sensors can be included as a layer in an inflatable structure, and the wires connecting to it can routed out through seams. If rigid surfaces are included on the inside or outside of an inflatable structure, the structure can be made to have flat, stiff regions with discrete joints in specified locations (Figure 2.2D). From our materials testing, the best materials are ABS, Polycarbonate, and PVC plastics.

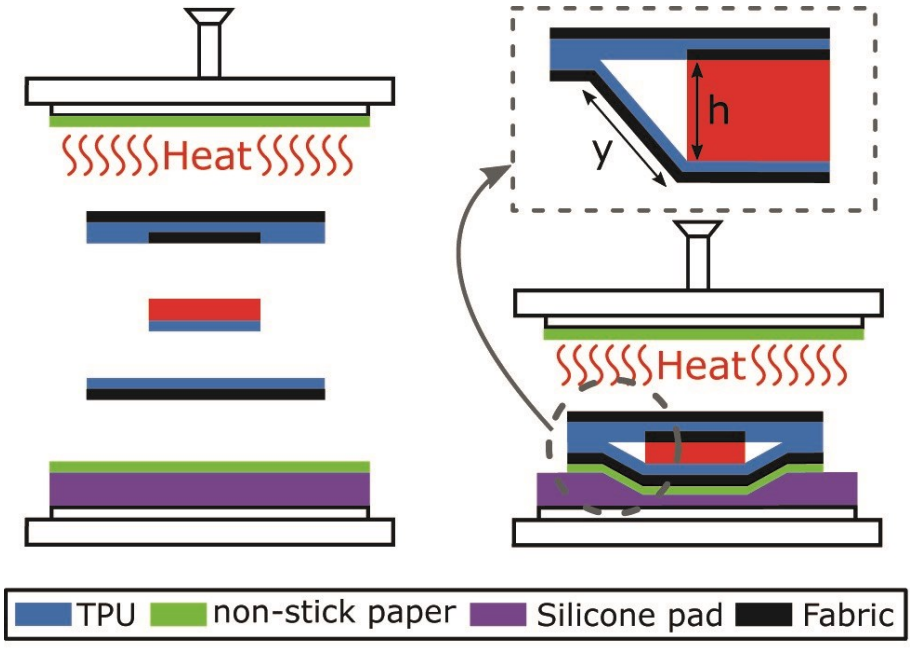

Figure 2.4. Manufacturing process to integrate a rigid part into a soft actuator.

Special consideration is warranted when including rigid surfaces on the interior of an inflatable chamber, since these can be much thicker than the typical layers of textile, plastic film, or TPU film (Figure 2.4). Due to the material thickness (h in Figure 2.4), there is a small space surrounding the object in which the surrounding textiles cannot bond. If the structure is bonded in the heat press, the silicone pad on the bottom will cause the material to conform to the included object while the top surface remains flat, as shown in the figure. The unattached length of textile is of length y.

Five samples were prepared with the geometry shown in Figure 2.4 but with different thicknesses of included object. For object thicknesses h of 1mm, 2mm, 3mm, 4mm, and 5mm, the unbonded lengths y were 0mm, 3mm, 4mm, 5mm, and 6mm, respectively. In other words, a 1mm thick object appeared to bond along its edge with the to continuously to the TPU film, and a 5mm thick object had an unbonded length of 6mm. This allows for objects 1mm thick or less to cross from the inside to the outside of an inflated chamber without leakage occurring; this is useful for, for example, placing sensors on the inside of a chamber and routing the wiring to the outside of the chamber.

Additionally, care should be taken when bonding rigid surfaces to the outside of an inflatable structure. In some circumstances, it may be desirable to bond structures that are very thick or that have a low melting point (see Section 4.4 for additional discussion about melting temperatures). If a rigid structure is very thick, it is not possible for the heat press to transmit heat through it. In this circumstance, the structure could be baked in an oven. If a rigid structure has a low melting or heat deflection temperature, it may deform when heated in an oven or with the heat press. Providing contoured supporting material can help prevent deformation in these circumstances. However, for both thick materials

and materials with a low melting point, a technique that can be used with the Type I and Type II processes is useful, shown in Figure 2.5.

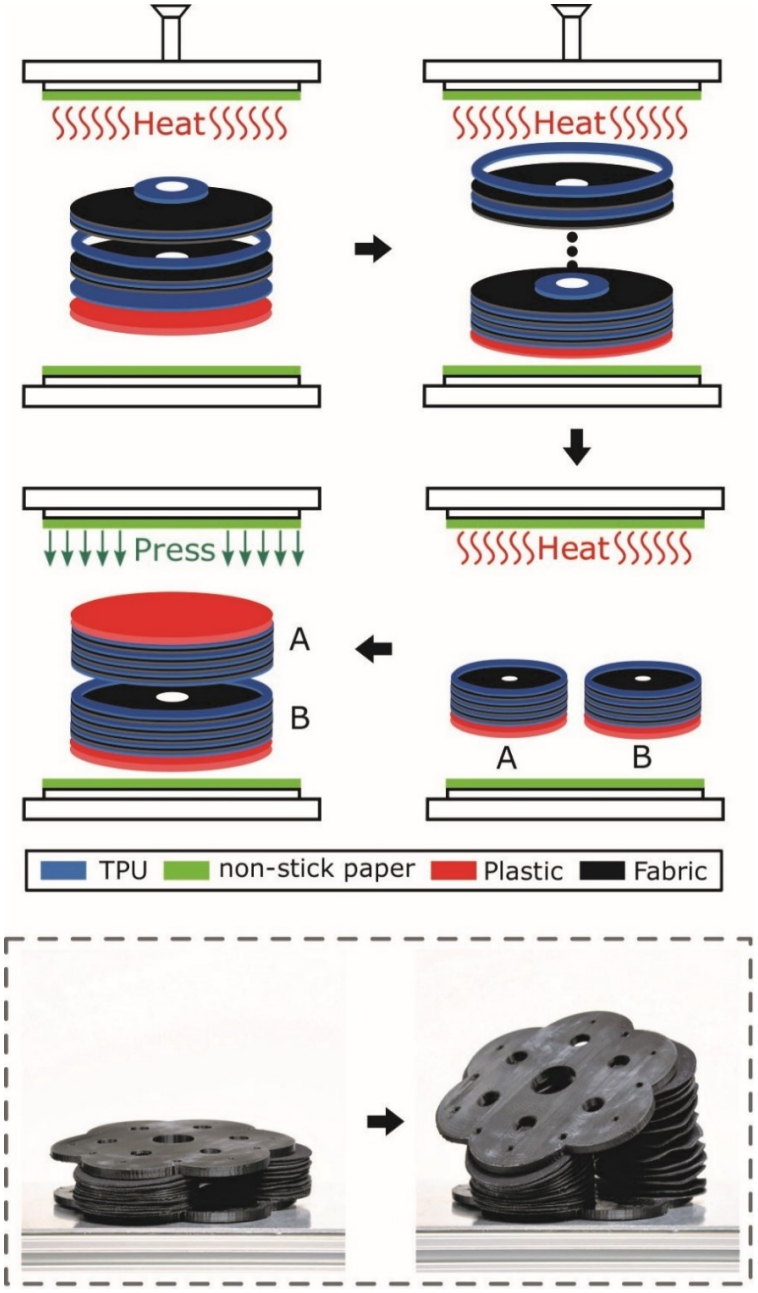

Figure 2.5. Additional detail on one method to bond soft and rigid surfaces. Here, a 3D printed plate is bonded to three bellows structures next to each other. The structure shown at the bottom of the figure is one of the actuated segments in the robotic arm in Figure 2.10.

Figure 2.5 shows the process by which an inflatable structure can be bonded to a rigid structure on each end, for example a segment of the robotic arm in Figure 2.10 which has a 3D-printed ABS plate on each side of three bellows structures (the segment is shown at the bottom of Figure 2.5). The first step is to place the rigid structure on the bottom of the heat press, and TPU film and other thin layers on top, as shown in the first two panels of Figure 2.5. It is recommended to bond two layers of TPU film and textile on the top at a time, for a maximum of 20~30 seconds, in order to avoid melting rigid structures such as ABS plastic with relatively low heat deflection temperatures. Additionally, if a structure has small variations in height, e.g. from being 3D printed, it is necessary to place 0.4-0.5mm of TPU between the structure and adjacent layers to achieve proper bonding.

This process can be used to make two segments (A and B in the third and fourth panels) that have same height. Then, the two segments have their top layers of TPU film melted simultaneously in the heat press under low pressure (panel 3). Once the TPU film is melted, the two segments can be placed together and pressed with no additional heat until the TPU bonds. This allows for airtight structures to be made with thick rigid plates on both ends.

2.4.3 Corners

With both the Type I and Type II processes, it is possible to make folds in the material before bonding it together, and to make corners where three or more faces come together at a point. The addition of folds and corners greatly expands the possible robot topologies able to be made with these processes. To construct seams and corners from sheets of material, there are three different possible simple arrangements of material, shown in Figure 2.6. These include "OUT" seams, where the material pieces are parallel and the seam is on the exterior of the structure, as shown in all previous figures; "IN" seams, where both pieces of material are folded 180 degrees back on themselves, and the TPU film is placed on the folded parts, so that the seam is on the interior of the structure; and "180°" seams, where one piece of fabric is folded at a 180 degree angle and the other is flat. The folds are created after pre-laminating the fabric with TPU film, before the final assembly step.

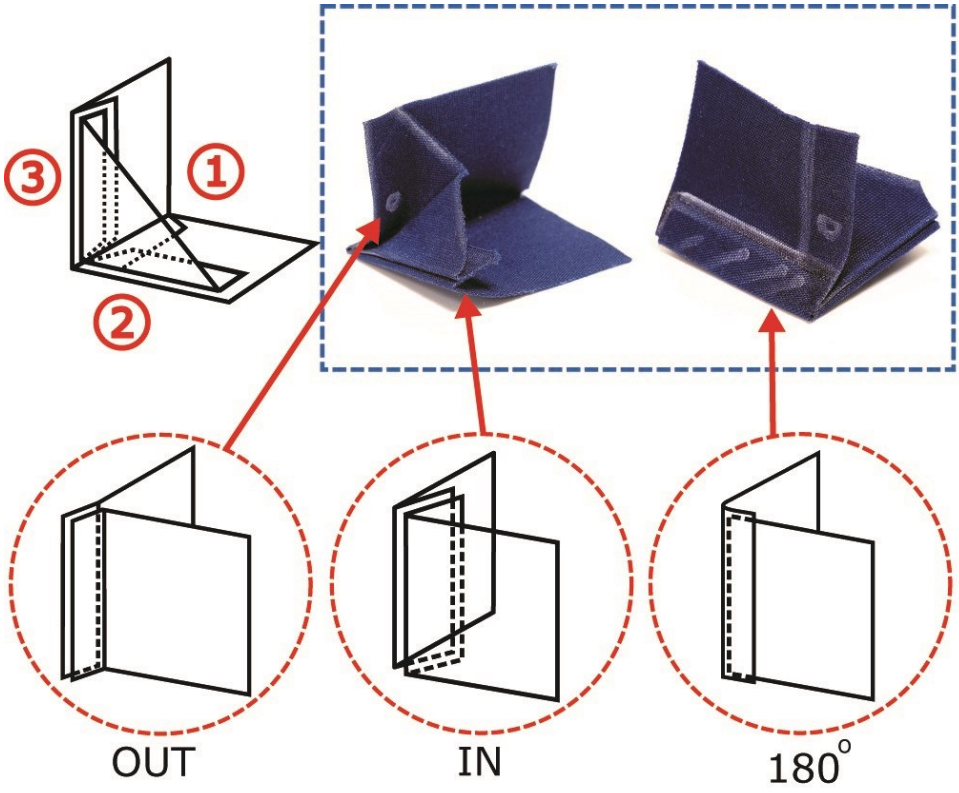

Figure 2.6. Three types of possible corners for an airtight 180, IN, OUT actuator.

We can create corners using different seam types. We constructed all of the possible corner types for corners with three seams using the Type II manufacturing process and tested them to determine it is airtight or not. The results are shown in Table 2.1. Figure 2.7 shows three examples of corners that are airtight, and one example of a corner that is not airtight. Two different geometrical structures with folds and corners are shown in Figure 2.8.

We found that for a corner to be airtight, it must contain at least one OUT seam. If the structure does not contain OUT seam, then there is an air leak from a tiny hole where the pieces of fabric join together. These holes are due to the bulk of the fabric and TPU

film on the interior of the structure, and the amount of area with TPU film available for bonding. With the IN and 180° seams, there are several layers of laminated fabric that are on the interior of the corner. This creates a large bump that prevents some of the layers from getting close together, resulting in a small hole. Additionally, layers of fabric on the exterior of the corner may slide or shift during the bonding process to accommodate the large bump. This can be observed with the 180° edge in Figure 2.7D. When the fabric shifts, a hole may develop as well. It may be possible to cover up small holes at corners with additional small pieces of TPU film placed strategically inside the corner, but this was not tested.

TABLE 2.1. POSSIBILITIES FOR AIRTIGHT CORNERS

Corner Style			*Airtight Chambers*
1	*2*	*3*	
OUT	OUT	OUT	Yes
IN	OUT	OUT	Yes
IN	IN	OUT	Yes
IN	IN	IN	No
180	OUT	OUT	Yes
180	180	OUT	Yes
180	180	180	No
180	IN	IN	No
180	180	IN	No
180	IN	OUT	Yes

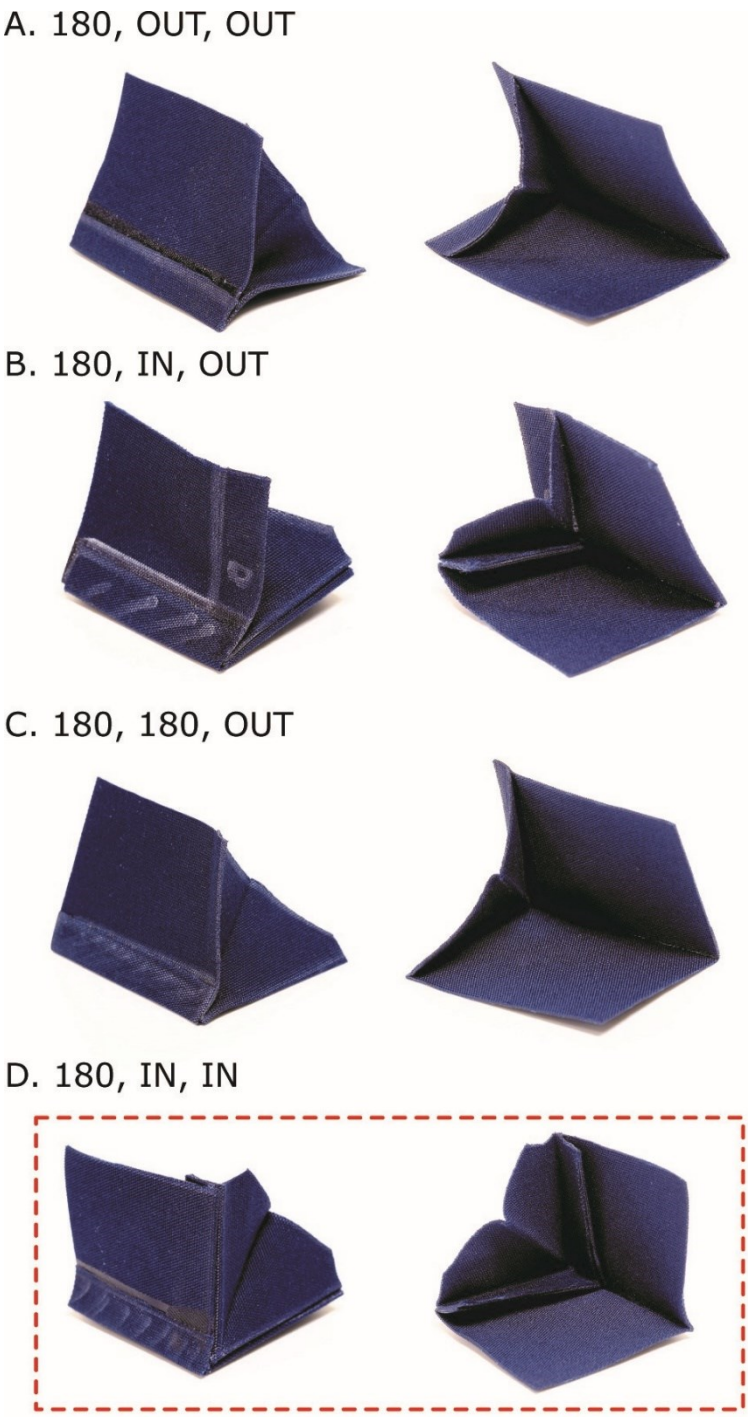

Figure 2.7. (A-C), Examples of airtight corners. (D), Example of a corner that is not airtight.

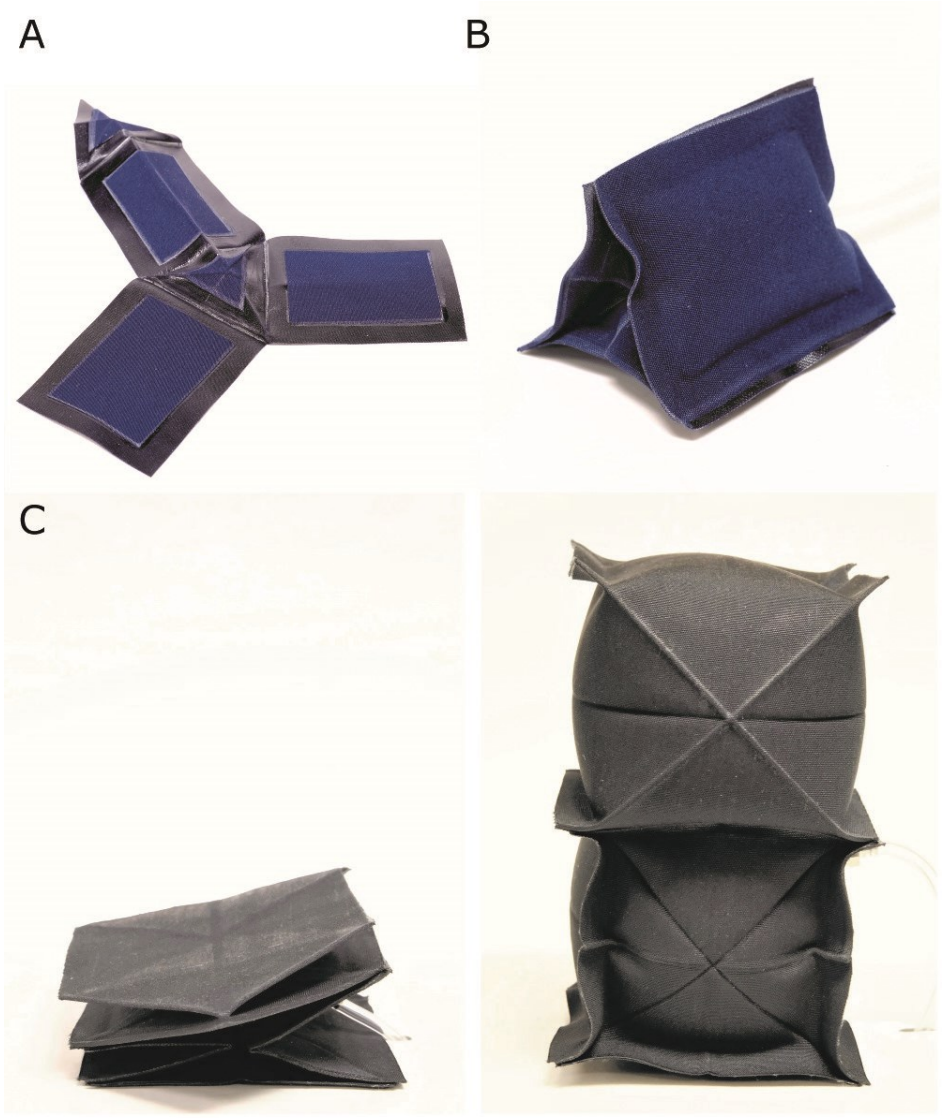

Figure 2.8. Sample chambers incorporating folds and corners. Subfigure A shows the flat pattern for the triangular prism in B. Areas of blue fabric are visible on the interior of the structure, which prevent those regions from bonding; the black regions around the perimeter have exposed TPU film, and they will bond together to form the final structure. C shows the deflated and inflated states for a structure with two connected rectangular chambers.

2.5 Modeling and Experiments

We next present mathematical models and experimental data for both a single pouch and a bellows structure comprised of multiple stacked pouches.

2.5.1 A Single Pouch Chamber

We first consider a single circular pouch chamber, with a schematic and variables shown in Figure 2.9A. The figure shows a side view of an inflated pouch: a flat circular chamber with radius r inflates to a shape with a radius a and where the height of the cross-section above the equator is $f(x)$. The shape of the inflated pouch is similar to that of an inflated mylar balloon, which was studied by Paulsen.[64] Following Paulsen's analysis, the volume of the pouch is

$$V = 4\pi \int_0^a x f(x) dx \tag{2.1}$$

subject to the constraint of

$$\int_0^a \sqrt{1 + f'(x)^2} dx = r \tag{2.2}$$

The pouch assumes a shape $f(x)$ so as to maximize the inflated volume. Paulsen found that the radius of the inflated chamber (a) is 0.7627 times the uninflated radius (r), and the thickness of the inflated chamber is $2f(0) = 0.9139r$. We tested sample pouches of several radii and found the samples' geometry matched this model within 1%.

2.5.2 A Chamber with Multiple Pouches

We next consider the geometry of a stack of circular pouches connected in their interior (Figure 2.9B). Within a stack, each pouch is bonded to its neighbor with a radius c, leading to flat regions on the top and bottom of the pouch. The height in the center of the pouch is then h_c, and the total height of a stack is h_{total}. The cross-sectional shape of a pouch in the center of the stack will differ somewhat from that of the Paulsen model due to the flat ends; we wrote a custom Matlab (The Mathworks, Inc., Natick, MA) script to simulate the shape of a sample chamber (with uninflated radius 3cm) given the boundary condition of the ends being flat. The results are in Figure 2.9C, and show the upper right quarter of a pouch. It can be seen that for bonding radii c even up to 2/3 of the uninflated radius r, the shape is very close to a truncated form of a single inflated pouch. The volume of the pouch also remains nearly constant as the bonding radius increases, decreasing by only 3% with $c = 1.5$cm and 12% by $c = 2$cm.

This simulation in turn allows us to predict the total height of a stack of pouches. Sample chambers (3cm radius, 5mm seams) with three pouches and varying bonding radii c of 1, 1.25, 1.5, 1.75, and 2cm were fabricated and compared to the simulation when inflated to 69kPa. The results are in Figure 2.9D and show that the simulations match the experimental data within 5%.

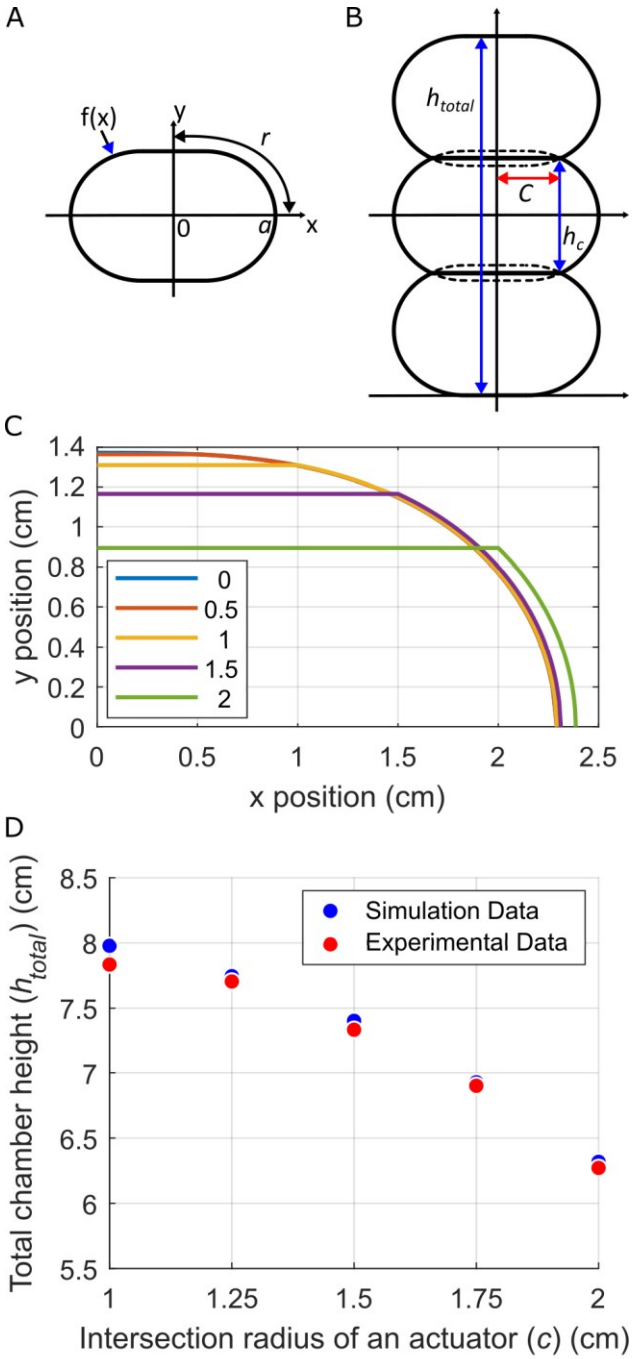

Figure 2.9. (A), Cross-sectional view of a single pouch, with variables used in modeling. (B), Cross-sectional view of a chamber formed by three connected pouches, along with variables. (C), Results of simulations showing the shape of the top left of a cross-section of a single pouch. The different colors correspond to different flat regions c. (D), Simulation data and experimental results of the height of a stack of six pouches with differing bonding radii.

2.5.3 Force vs. Displacement Modeling and Experiments

We conducted several tests on chambers consisting of a stack of six pouches (6cm diameter, 5mm seams, 4.4cm bonding diameter). In the first test, we measured the restoring force when the chamber was pulled outward mechanically from its ends, with the results in Figure 2.10A. The first three tests of the chamber after it was manufactured had a peak force of around 70N, which dropped to around 33N after the chamber was cyclically inflated and deflated 100 times. The restoring force $F_{restore}$ was observed to be a quadratic function of the chamber's extension x, with an equation

$$F_{restore} = \begin{cases} 0.86\,(x - 1.9)^2 & x > 1.9 \\ 0 & x \leq 1.9 \end{cases} \tag{2.3}$$

for the tests after 100 cycles, where x is in centimeters and $\mathrm{F_{restore}}$ is in Newtons.

The next set of tests measured the total force created lengthwise by a chamber when it was inflated. This total force is the sum of the outward force from the air pressure minus the restoring force,

$$F_{total} = F_{outward} - F_{restore} \tag{2.4}$$

A chamber was placed in an Instron machine at various pressures, and the force measured as the machine permitted its length to increase; the results are shown in Figure 2.10B. It can be seen there that for small expansion distances below around 6cm, the force decreases roughly linearly with the actuator's length. In this region, each pouch in the chamber is compressed to have flat ends with a radius $r_{end} > c$, so the cross-sectional area

$\pi {r_{end}}^2$ is large, and the outward force $F_{total} = P\pi {r_{end}}^2 - F_{restore}$ is similarly large, where P is the internal pressure. As the chamber expands, the cross-sectional area decreases approximately linearly. At large extension distances, the force drops off rapidly both because the end pouches have a smaller contact area with the world, and because the restoring force $F_{restore}$ increases. Also of note, the maximum length of the chambers increases at higher pressures, as they more closely approximate the mylar balloon model. At lower pressures, the bending and wrinkling that occurs at the seams causes them to be slightly shorter.

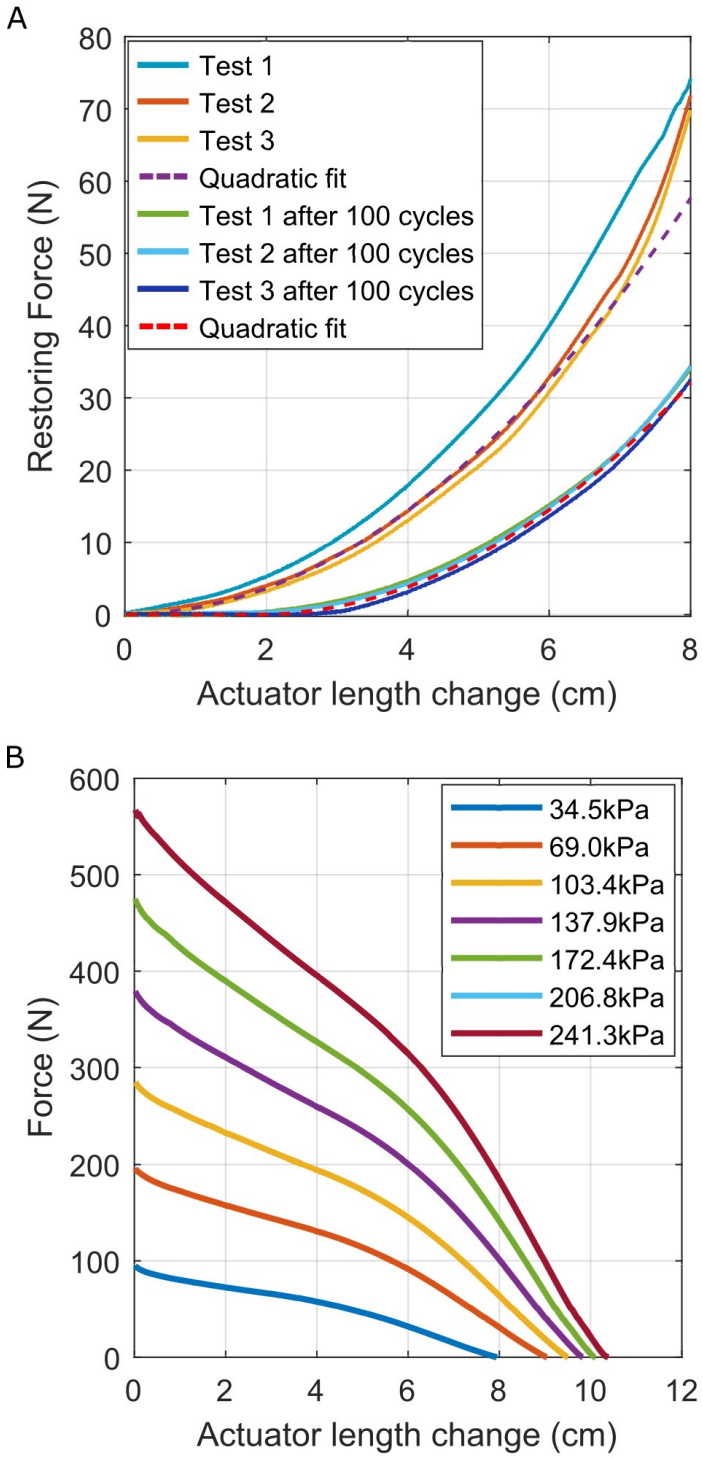

Figure 2.10. (A), Graph of the restoring force when a chamber with six pouches is stretched at atmospheric pressure. (B), Graph of the expansion force versus actuator length as a chamber with six pouches is inflated to different pressures.

2.6 Materials and Measurements

2.6.1 Materials testing overview

We conducted several tests to determine a library of materials that will work with this fabrication process. Specifically, we tested how well the TPU film bonded to several different types of textiles, the yield strength and elongation of these textiles, and how well several rigid materials could be attached to textiles with TPU film. We tested four types of fabric: Poplin (65% polyester, 35% cotton, 0.30mm thick, plain weave); Cotton (0.35mm thick, 2x1 twill weave); Polyester (0.35mm thick, 2x2 balanced twill weave); and Rayon (0.30mm thick, 2x1 twill weave). We also tested a number of rigid materials: Acetal, also known as Polyoxymethylene; Acrylonitrile butadiene styrene (ABS); Nylon, also known as Polyamide; Polycarbonate (PC); Polylactic acid (PLA); Polypropylene (PP); Polystyrene (PS); Polyurethane (PU); Polyvinyl chloride (PVC); a standard printed fiberglass-epoxy printed circuit board (PCB); and Aluminum that was both smooth and sanded to be rough. These were selected as they are common engineering materials or materials used in 3D printers.

2.6.2 Tests with textiles

Several types of fabric were tested to measure their tensile strength, in order to determine the strength of structures that can be created using this manufacturing method. For the test, two types of samples were prepared: pure fabric, and the patterned fabric-TPU-fabric

sandwiches such as those used in the Type I manufacturing process. Samples constructed were 1cm wide, and were cut either along the fiber direction (0°) or at a 45° angle (on the bias). These were placed into an Instron 4204 machine and pulled lengthwise at 20 mm/minute until failure occurred (i.e., the materials tore); force and displacement were recorded during each trial. The force in Newtons to cause tearing in a 1 cm wide piece of material is shown in Table 2.2. The results showed that poplin fabric has the highest tensile strength compared to the other fabric types. Samples made with the sandwich construction had approximately twice the tear strength as the textile in isolation, and all samples cut at a 45° angle showed a much lower strength as compared to the 0° samples.

A second set of tests examined how well the fabric bonded to the TPU film, with the results in Table 2.3. Samples were prepared in which two pieces of fabric were bonded together at one edge, and the un-bonded edges were clamped in each side of an Instron machine and pulled apart. In this manner, the bonds were pulled apart in a T-peel test. The samples were tested with the same process as the previous test. The results showed that the poplin, polyester, and rayon fabrics all bonded equally well, and were limited by the strength of the TPU film itself, which tore apart.

TABLE 2.2. TENSILE STRENGTH OF FABRICS

Fabric	*Tensile Strength (N/cm)*	
Weave Angle	0°	45°
Poplin	337	74
Polyester	176	22
Cotton	108	30
Rayon	77	16
Poplin-TPU-Poplin	647	329
Polyester-TPU-Polyester	621	231
Rayon-TPU-Rayon	263	196
Cotton-TPU-Cotton	159	80

TABLE 2.3. BOND STRENGTH OF JOINTS (FABRIC TO FABRIC)

Fabric to Fabric	*Maximum Bond Strength (N/cm)*
Polyester – Polyester	64 ± 2
Poplin – Poplin	64 ± 2
Rayon – Rayon	64 ± 2
Cotton – Cotton	42 ± 2

2.6.3 Tests with rigid materials

We also tested to decide what rigid materials bonded effectively using the TPU film, which is important to understand for building hybrid soft-rigid robots. Samples were constructed in which poplin fabric was bonded to a rigid material at one edge, but with the other edges unbonded. The unbonded edges were placed in an Instron machine with the same test conditions as before, except that the fabric was pulled off from the rigid surface at a 90° angle with respect to the rigid surface (a 90° peel test). The results are shown in Table 2.4. ABS and Polycarbonate plastics bond well with the film, with a strength in excess of the bond between poplin and TPU. In the tests the poplin fabric delaminated from the material before the TPU came off the plastic. Additionally, a standard printed circuit board showed moderate adhesion, enough so that circuit boards with sensors could be mounted inside inflatable structures. Acetal plastic, Aluminum (both smooth and sanded), Nylon, Polypropylene (PP), and Polystyrene (PS) do not bond very well at all; the materials came apart easily by hand, and due to this they were not tested in the Instron machine. There do exist a variety of products that can be used to pre-treat metals and plastics to alter their surface chemistry and improve their bond strength with TPU films [65], but we did not test these.

TABLE 2.4. BOND STRENGTH OF JOINTS
(POPLIN FABRIC TO RIGID MATERIAL)

Poplin Fabric to Rigid material	*Maximum Bond Strength (N/cm)*
Poplin – Poplin	64 ± 2
ABS	> 66
Polycarbonate	> 66
PVC	50 ± 2
PLA	35 ± 2
PU	32 ± 2
PCB (Circuit Board)	10 ± 2
Acetal	~ 0
Aluminum	~ 0
Nylon	~ 0
PP	~ 0
PS	~ 0

2.6.4 Material Softening and Melting Temperatures

We collected data on the heat deflection temperatures and melting temperatures of a number of possible materials that could be used with the manufacturing process, and the results are shown in Table 2.5.[66]–[72] Shown are the rigid materials that bond well with TPU film from Table 4 as well as some other materials of interest. As shown in the table, all of the materials have melting points above the melting point of TPU (130-150℃). However, most of them have heat deflection temperatures less than 150℃, which means that they may deform when heated and pressed during the bonding process. As such, it may be important to construct the assembly so that there are no asymmetric forces on the plastic pieces being bonded. Alternatively, high-temperature formulations of PLA and Polycarbonate can have heat deflection temperatures above 150℃, allowing them to be used without additional considerations. Also shown in the table, printed circuit boards and solder have deflection temperatures or melting temperatures higher than 150℃, allowing them all to be used in this process directly.

TABLE 2.5. MELTING AND DEFLECTION TEMPERATURES OF MATERIALS

Material	*Heat Deflection Temp.* (℃)	*Melting Temp.* (℃)
TPU	110 ~ 130	130 ~ 150
PLA	50 ~ 160	130 ~ 243
PVC	69 ~ 85	154 ~ 210
ABS	70 ~ 107	180 ~ 274
PU	143	
Polycarbonate	127 ~ 147	250 ~ 343
Fiberglass-Epoxy PCB	130 ~ 180	
Lead-Free solder		≥ 220
Silver solder		≥ 220

2.6.5 Seams

Sample chambers with various seam widths were tested to determine how well different seam sizes work in the manufacturing process. The chambers were fabricated with different seam widths (2 mm, 3 mm, 4 mm, 5 mm, and 8mm) by the Type I method, and all had an outer diameter of 6.5cm. They were then inflated to 69kPa (10 psi), and the results are shown in Figure 2.11. The chambers showed different behavior at their edges depending on the seam width; in Figure 2.11, a yellow line was drawn highlighting the edge of the inflated region. Narrow seams showed more wrinkling than wider seams, with the 8mm seam showing only four wrinkles around the circumference of the chamber. The test results showed that an inflated chamber should have wider than a 2mm seam to be air-impermeable under 69kPa. However, the chambers with both 2mm and 3mm seams showed sharp bends in the seam, which we determined can decrease the service lifetime of the structure (number of inflate/deflate cycles before a leak). Therefore, it is recommended to design structures with a seam width greater than 3mm; 5mm was used in making most of the structures in this paper. Additionally, if only gradual wrinkles are desired, a seam should be made to be at least 8mm wide.

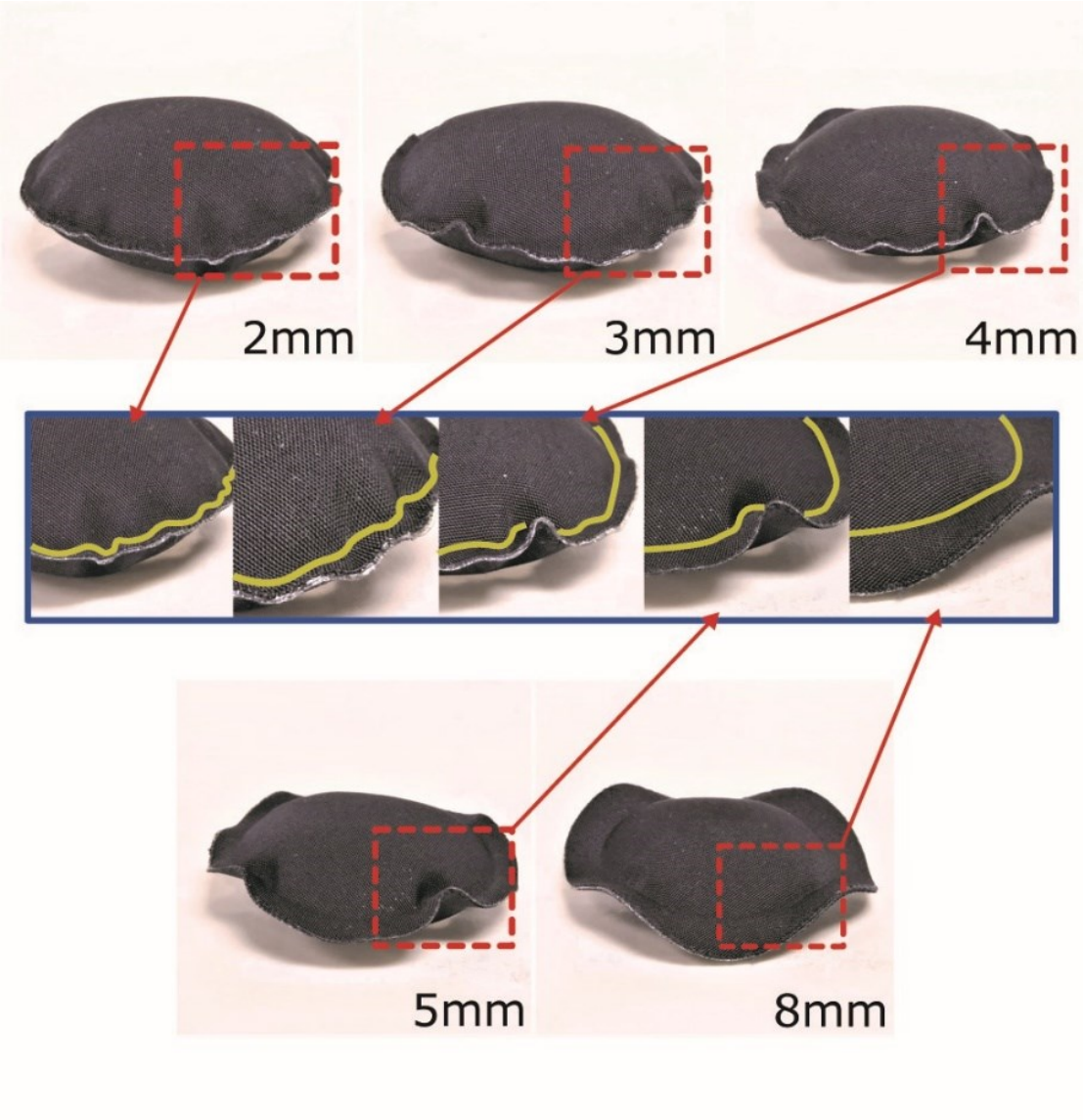

Figure 2.11. Wrinkle and buckling at the seams of sample chambers with different seam widths (2mm, 3mm, 4mm, 5mm, and 8mm).

2.6.6 Maximum Pressure and Service Lifetime

Tests were conducted to determine the maximum pressure an inflatable chamber could sustain. Sample pouches were made with the Type II process (made with poplin fabric, 5mm seam width, and varying radii), and inflated until they leaked; the results are shown in Figure 2.12. In the figure, the red dots show experimental trials which ruptured, while the red asterisks show experimental trials which did not rupture, and the maximum pressure was limited by the equipment available to test them. The chambers were able to support maximum pressures of as little as 72kPa, for a 10cm radius chamber, and as much as 315kPa (45psi) for chambers with radii of 4cm or less. Failures occurred when the seam delaminated, with the TPU film unable to hold the two sides of the chamber together.

Also shown in the figure is a blue line, which is the predicted inflation pressure based on the edge seam failure strength and the geometry of the chamber. Following the nomenclature in Figure 2.9, a chamber with uninflated radius r and inflated radius a will have a perimeter of length $S = 2\pi r$ and a cross-sectional area at the equator of $A = \pi a^2$ when inflated. If the edge can support a linear force of γ Newtons per meter of seam length before delaminating (as was measured in Table 3), then the total force supported by the entire edge at rupture should theoretically be

$$F_{rupture} = \gamma S = 2\pi\gamma r \tag{2.5}$$

which corresponds to a maximum pressure of

$$P_{rupture} = \frac{F_{rupture}}{A} = \frac{2\pi\gamma r}{\pi a^2} = \frac{2\gamma r}{(0.7627r)^2} = \frac{3.44\gamma}{r} \quad (2.6)$$

This is plotted in Figure 2.12 with $\gamma = 6200$ N/m. This analysis predicts failure pressures of roughly 50-100% more than the experimental data shows; this is likely due to high stress concentrations occurring at the wrinkles that occur around the seam (see Figure 2.11). Using wider seams may result in a higher failure pressures, since chambers with wider seams exhibit less wrinkling (Figure 2.11).

Tests were also conducted to determine the cycle life of actuators made with this process. Actuators with three chambers were fabricated with the Type I method (6cm diameter, 5mm seam width), and connected to an air supply with a solenoid valve. During the test, a sample actuator was fully inflated to a specified pressure, and then the solenoid valve was opened to vent the air. Then, the actuator was deflated to 20% of its maximum length through the action of a second similar actuator pushing on its end and forcing the air out. Each inflate-deflate cycle took 0.7 seconds on average. Tests were conducted at the pressures of 69kPa, 138kPa, and 207kPa as measured by an air regulator. Each test continued until the inner pressure of the actuator did not reach the specified pressure, which indicated that the actuator ruptured at a point on the seam, or until the test reached 100,000 cycles. The results were that the actuator inflated to 69kPa (10psi) worked for more than 100,000 cycles, the actuator inflated to 138kPa (20psi) worked for 95,000 cycles, and the actuator inflated to 207kPa (30psi) lasted for 20,000 cycles. Since holes appeared at locations where the seam creased sharply, we hypothesize that using wider seams may increase the service lifetime.

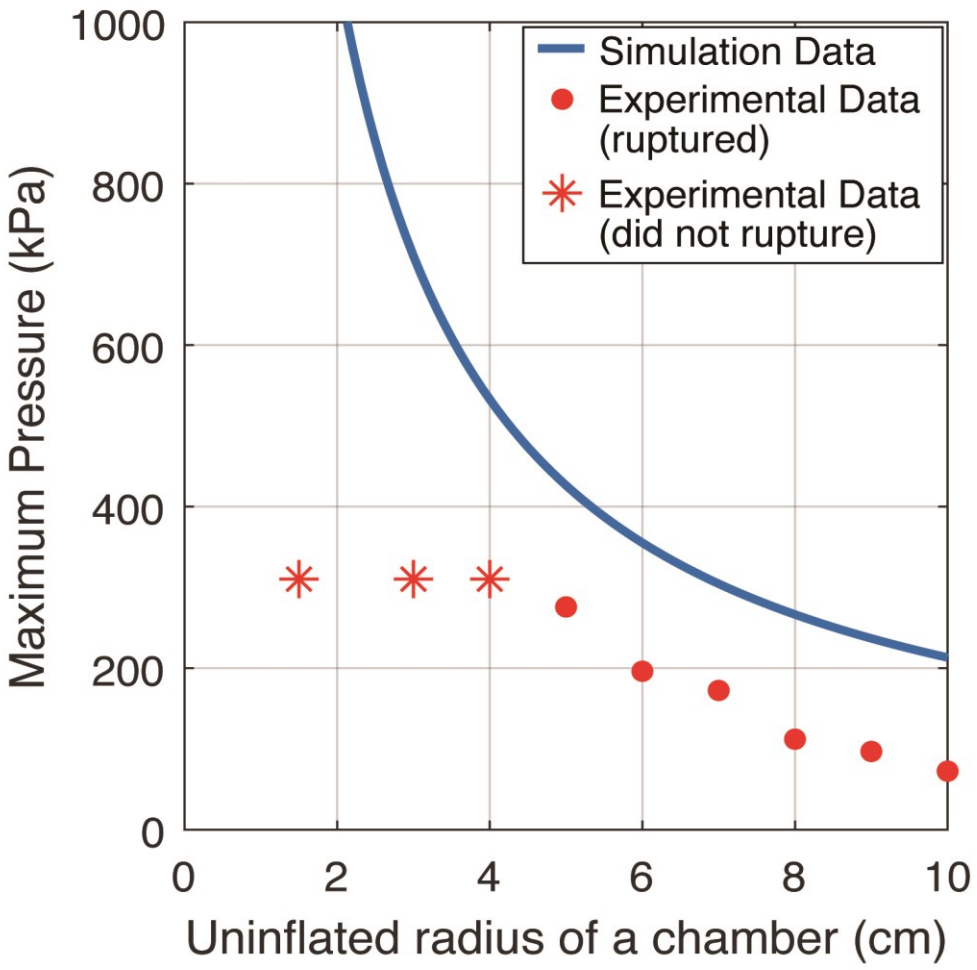

Figure 2.12. Simulation data and experimental results of the maximum pressure a single chamber can sustain before rupturing. The asterisks indicate samples where the maximum pressure was limited by the available air supply, and the pouches did not rupture.

2.7 Application

2.7.1 A Sensorized Actuator

To demonstrate the ability to incorporate wiring and circuit boards, we constructed a sample actuator (6cm diameter, 5mm seams) which included an embedded distance sensor (VL6180X Time-of-flight sensor, mounted on a breakout board). As shown in Figure 2.13A, the breakout board was bonded to the interior of one end of a bellows chamber, and an additional layer of fabric and TPU film was placed around its perimeter to further secure it. The wires were routed out through one of the seams. The wire insulation was made of PVC, as is extremely common; due to its low melting temperature (Table 2.5), the insulation melted to some extent inside the seam, which led to a flatter profile and an airtight seal in conjunction with the TPU film. During testing, the actuator was commanded to cyclically inflate until the sensor read 7cm, then deflate until the sensor read 1cm (Figure 2.13B).

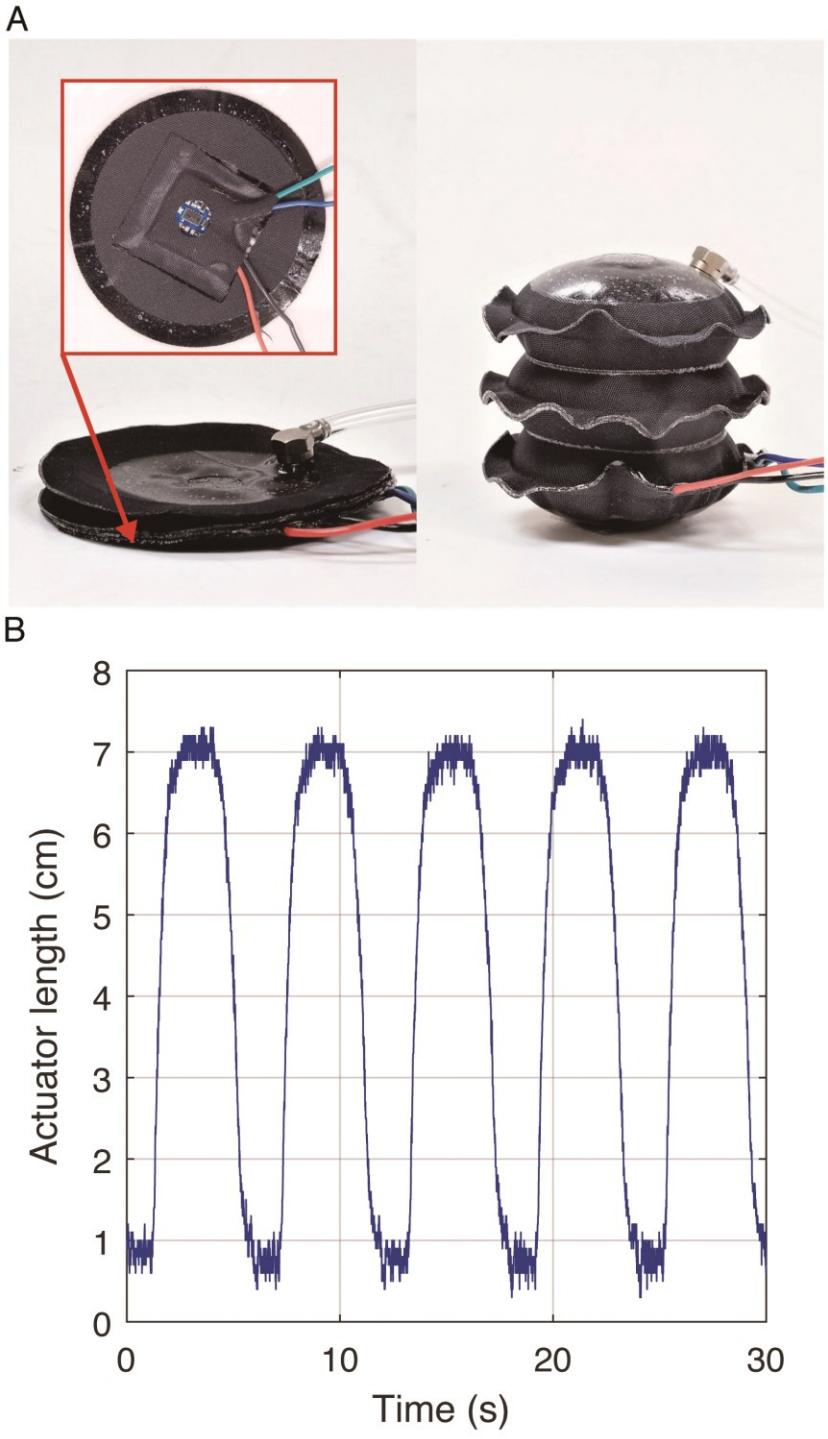

Figure 2.13. (A), Bellows actuator with an embedded distance sensor. The red box shows a view of the bottom layer inside the actuator before it was fully assembled. (B), Graph of the actuator length versus time as it was cycled between 1cm and 7cm lengths.

2.7.2 Pneumatic Hybrid Soft/Rigid Robot Arm

We demonstrate the fabrication method in designing various applications with three inflatable robots. The first example is a pneumatic hybrid soft/rigid robot arm, shown in Figure 2.14. The arm has two straight sections with joints in between and at the ends. The joints are each composed of three bellows structures, with rigid 3D printed ABS plates on each end; the joints were previously shown at the bottom of Figure 2.5. The actuators were fabricated with the Type II process, and the 3D printed plates were attached using the process described in Figure 2.5. The straight sections were constructed using two sheets of textile, bonded in a number of narrow strips so as to make chambers along the length of the robot arm. These long chambers are all inter-connected, so the sections only require a single air hose to inflate the entire structures. After being bonded to make these chambers, the structure is wrapped into a cylinder shape and bonded to ABS end plates using additional TPU film. The different segments of the robot are attached together by bolting their ABS end plates together, enabling the robot to be easily reconfigured or disassembled for repair.

The robot arm thus contains 11 chambers: one in each of the straight segments, and three in each of the joints. Each chamber is inflated or deflated via a tube that passes through the center of the robot. In Figure 5, holes in the center of the ABS end plates can be seen; the tubes pass through these holes to extend along the length of the robot. The tubes were connected to the actuators via tube fittings that were threaded into the ABS end

plates. The robot can collapse when it is deflated, and the joint can bend to 90° in any direction respectively.

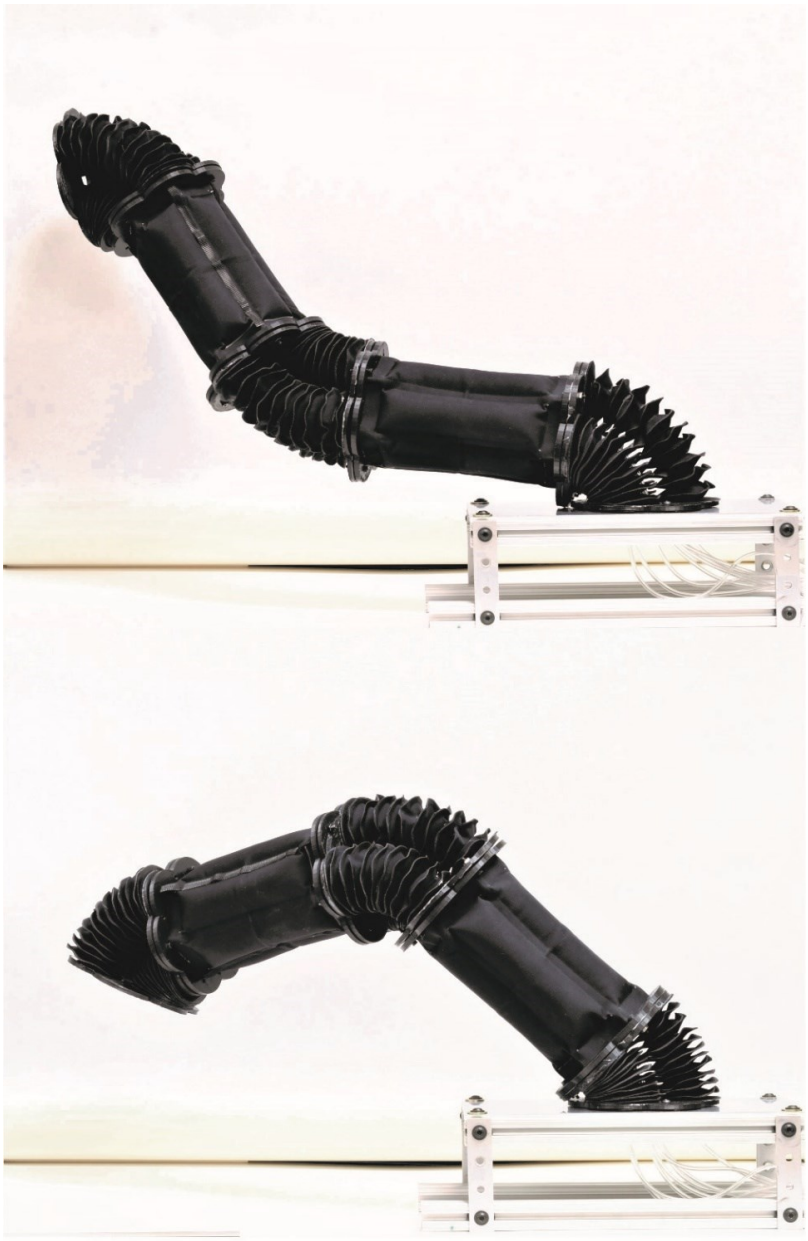

Figure 2.14. The low-cost pneumatic soft/rigid hybrid robot.

2.7.3 A Rolling Robot

As a second example of a robot fabricated with this process, we made two types of pneumatic robots that can roll along the ground (Figure 2.15). The first robot with bellows type actuators is constructed with the Type I process, and the second robot with origami-like actuators is fabricated with the Type II process. Air is supplied by attaching screw-on tube fittings (Pneumadyne Part #EB25) and connecting pneumatic tubing. The robots are formed of three structures arranged in a triangle. In the first robot, the bellows are constructed asymmetrically, with each chamber bonded to its neighbors off-center (with the hole connecting the chambers in the center of the bonded region). This construction causes the bellows to curl when inflated, as can be seen in Figure 2.15. The second robot uses an origami structure with chambers similar to those in Figure 2.8. Both of these structures can be made to roll along the ground by sequentially inflating the chambers.

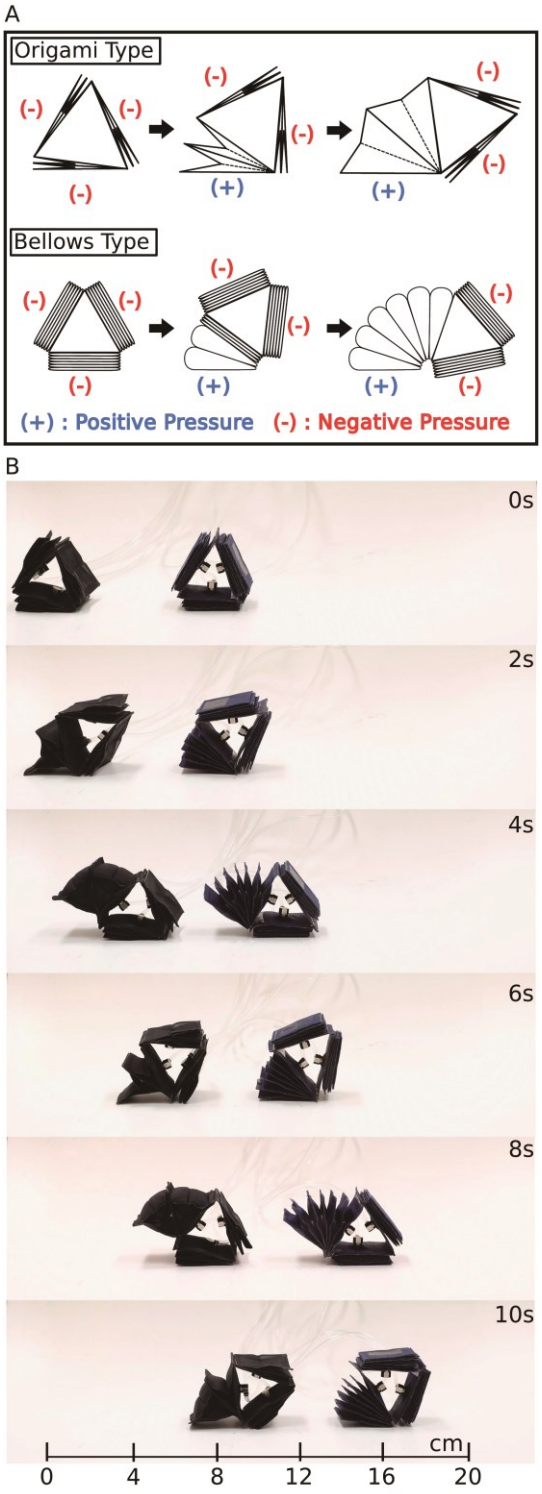

Figure 2.15. (A), Diagrams of the two methods of constructing the revolving robot. (B), Photos showing the two rolling robots in operation.

2.7.4 A Pipe-climbing Robot

A final example robot fabricated using this process is designed to climb inside pipes (Figure 2.16). The robot is composed of three segments: the first and third segments (1 and 3 in Figure 2.16, respectively), each have three bellows chambers arranged in a triangle, similarly to the rolling robot, except that the bellows are designed to expand radially instead of curling. The second segment (**2** in Figure 2.16) is in between the two, and has three bellows chambers arranged in parallel between the first and third segments. 3D printed ABS plates are located between the segments. The first and third segments expand outward to grip the inside of a pipe, while the second segment acts as a body structure to allow the robot to move forward and bend. By inflating and deflating the three segments in an appropriate sequence, the robot can be made to climb inside confined spaces such as pipes. The robot can be manufactured using any of the proposed methods.

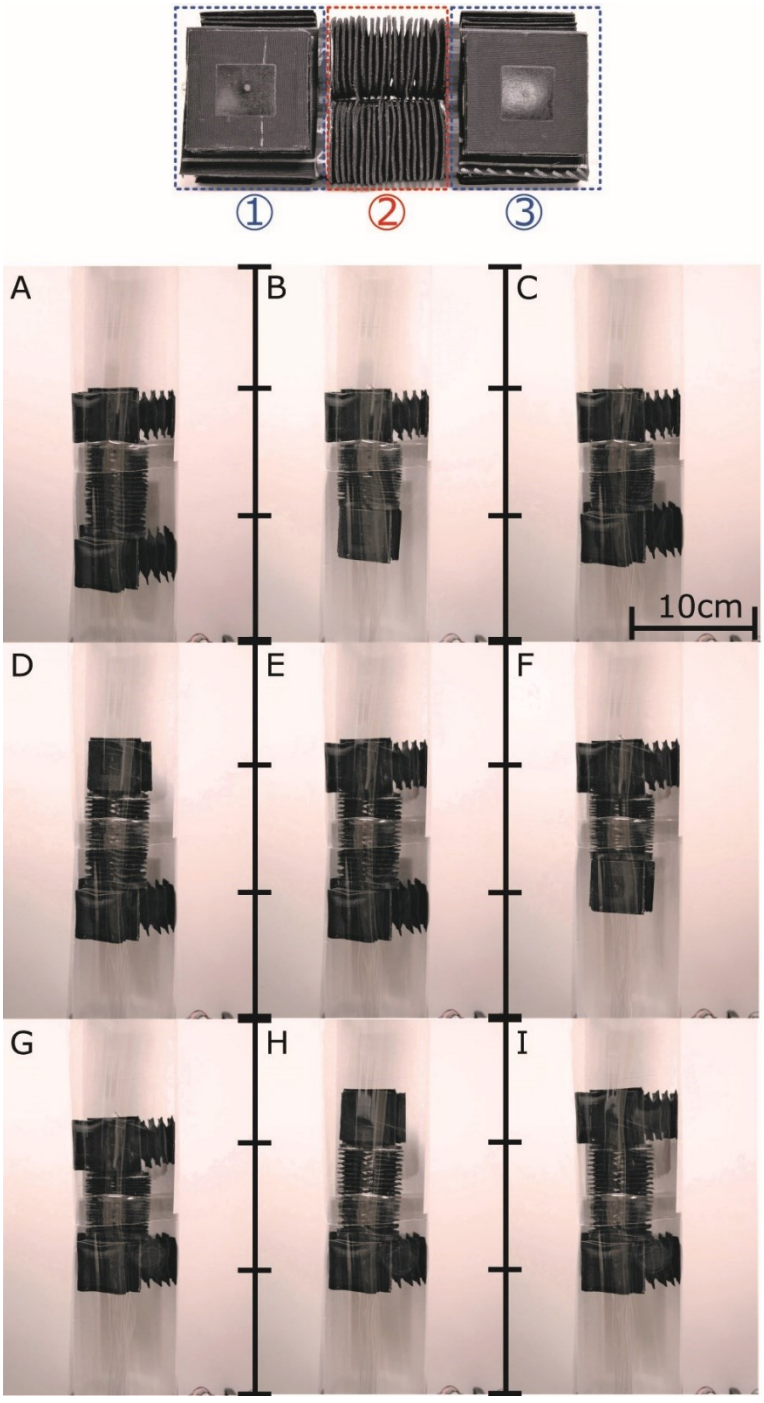

Figure 2.16. Construction and motion of the pipe-climbing robot. Sections 1 and 3 can extend arms to grip the tube radially; section 2 can extend and shorten to allow the robot to move along the pipe.

2.8 Conclusions

In summary, we present a thorough investigation into how soft robots can be fabricated in layers using TPU film to bond the structure together. The manufacturing process is simple, and fast, with robot pieces able to be cut out on a vinyl cutter and assembled in less than 30 minutes. The process is low-cost, with most textiles costing <$10 USD/yard and the thermal adhesive film costing around $10 USD/yard. The ability to include corners, folds, and rigid elements enables the creation of various robot morphologies, and the possibility to embed printed circuit boards and wires allows for the easy integration of a wide range of sensors. Additional work must be done to understand how corners and folds can be best utilized to generated different inflated shapes, and to determine any limitations on possible robot shapes as well as better understand the stress concentrations that occur at wrinkles in the seams. There are also many opportunities for further research in integrating sensors, and for developing new methods of locomotion and manipulation using this process.

Chapter 3.

Design and Characterization of a Modular Hybrid Continuum Robotic Manipulator

3.1 Abstract

We present a new design of a multi-DOF modular soft/rigid hybrid robotic manipulator that includes integrated electronics, composed of several modules which each provide 1-2 degrees of freedom of motion. To control the robot, we present a new variant of the piece-wise constant curvature (PCC) model made possible due to the geometry of the robot. Embedded inertial measurement units (IMUs) are used in conjunction with the robot model to determine its kinematics. With the model, the soft robot can be controlled using traditional forward and inverse kinematics. Compared to traditional rigid manipulators, it

has the advantages of being low cost and lightweight. We present models for each of the robotic joint modules created. With these models, we can perform calculations about the stiffness of each module, information that is useful when creating robotic arms with them. We further collect experimental data on the actual module stiffnesses in all directions through applying forces and torques, and use it to predict the behavior of the entire robot. The modeling introduced in this paper had errors of less than 5%, and the robot arm achieved positioning accuracy of less than 1cm.

3.2 Introduction

Traditional robotic manipulators designed and constructed from rigid materials are the most useful devices to have maximum stiffness and achieve very accurate positioning of an end effector. Due to this benefit, the manipulators are widely used in various industries for many purposes, including welding, assembly, or painting. Many advanced theories, including accurate modeling techniques, design processes, and control methods, have been developed for traditional robotic manipulators. Using these, robotic systems have been able to accomplish many tasks that previously had to be performed by humans [2], [73]–[76].

Recently, making robots human-safe has become a key issue for future robotic systems; some solutions thus far include introducing compliance through software and control systems for conventional robots [77]–[81]. Despite these efforts, conventional robotic systems still have challenges in spaces where humans and robots work in close proximity.

Meanwhile, soft robots typically have intrinsic compliance, low cost, and light weight, which make them safer around humans and potentially easily transportable and deployable [82], [83]. Due to these benefits, research in soft robotics has accelerated rapidly [84], [85]. On the other hand, softness causes design and control issues that are entirely different from those in conventional robotic systems. Because of this problem, we need to develop new design and modeling principles that can lead to controlling soft robotic systems more readily.

There has been much previous work in soft robotics focused on design and fabrication principles [86]–[91]. Among many types of soft actuators, artificial pneumatic actuators are most common because of their properties: fast operation time, high power density, large payload-to-weight ratios, and easy fabrication process [92].

The pneumatic actuators can be grouped based on their material properties and operation principle. The first type of actuators is made of elastomer based materials, and operate by positive or negative pressure [6], [60], [93]–[95]. The actuators achieve their actuation by an asymmetrical axial cross-section of their structures under positive or negative pressure. The structure causes bending or linear motion when placed under positive pressure [96] or vacuum [97]–[99]. A second type of actuator, which is composed of a fabric or a plastic sheet, has the same operating principle as elastomer based actuators [100]–[104]. They have pouches or origami structures that lead to making a structure expand or contract. Still other types of pneumatic actuators with a hybrid structure have been studied [105], [106]. A hybrid structure enforces specific kinematics to inflatable actuators, which leads to bending or expanding in a desired motion. The structure can also help increase the stiffness of pneumatic actuators.

Recently, using these soft pneumatic actuators, various soft robotic manipulators have been introduced [17], [46], [60], [107], [108]. The first example of soft manipulators is fabric or plastic sheets based robotic arm [108]–[112]. A second example is a soft fluidic elastomer robotic arm [17], [113]. The manipulators have different geometries which dictate how their positions can be controlled. One manipulator has an asymmetrical design with a core bladder and smaller bladders on one side, leading to curling in one dimension [109]. Other robotic arms contain three independent actuators in parallel and are made to bend and curl by changing the actuator lengths. In addition, some manipulators contain a cable-drive system to assist in moving in three dimensions. Most soft manipulators follow kinematics based on a piece-wise constant curvature (PCC) model [114]. The soft manipulators can adaptively manipulate unknown objects regardless of size and shape, and the robots are operated by bending motion. The bending motion is predicted based on complex kinematics and a geometrical approach. Due to this, it is very challenging to control these manipulators' trajectories very accurately.

In this paper, we propose a novel soft/rigid hybrid pneumatic manipulator that is easily controllable and has high positioning accuracy through the use of traditional robot kinematics algorithms. We begin by presenting two different types of robot joint actuator, specifically a revolute actuator and a roll-pitch actuator. We model their kinematics, including understanding how to determine their positions based on signals from embedded inertial measurement units (IMUs), with a modified version of the PCC model. We then present our control system for operating the entire robot. To understand the joint actuators in more detail, we then model a single bellows actuator and based on this model derive what pressures are needed in each chamber of the joint actuators, and what their stiffnesses

should be. We then conduct experiments determining the stiffness of the roll-pitch actuator in all six degrees of freedom, which is useful in predicting how an entire robot arm will respond to external loads. Finally, we present results from experiments with the entire robot arm, demonstrating its positioning accuracy and how it responds to external loads in practice.

Figure 3.1. A proposed soft/rigid hybrid pneumatic robot in this paper.

3.3 Manipulator design and fabrication

The proposed robotic manipulator is composed of modular subcomponents (A, B, and C in Figure 3.1). We design each segment with fabric bellows actuators and rigid components. In our previous work [115], we introduced a layered manufacturing method that can be used to create various soft actuator designs from fabric and thermal adhesive film. Among two types of fabrication methods presented there (Type I, and II), all bellows actuators in this paper were designed and made with the Type II process to be perfectly airtight. The bellows actuators are made of poplin fabric and thermoplastic polyurethane (TPU) film (#HM65-PA, Perfectex LLC.), and the rigid components are fabricated using a 3D printer. The TPU film is used to both bond the structural layers together and also to make textiles pouch-like structures using a heat press machine. The poplin fabric is a medium-weight textile (65% polyester, 35% cotton) which provides a good ratio of strength to thickness.

3.3.1 Revolute Actuator

Section A, in Figures 3.1 and 3.2, is a revolute actuator. It contains 3D printed ABS plates on the top and bottom, which together form a revolute joint at the center, and a bellows actuator around it. The bellows actuator has 20 inter-connected pouches, and is connected to an air hose via a tube fitting. Each pouch has a square shape, with a height of 5cm, a width of 4.8cm, and a seam width of 5mm. The pouches are bonded with an off-centered inter-connection area; this leads to the bellows curling around the revolute joint when it is pressurized. The revolute actuator can rotate 0 to 220 degrees, which is limited by the

length of the bellows. The actuator includes an embedded Inertial Measurement Unit (IMU) (Model BNO055) in order to sense its rotation. The top rigid component contains the sensor on its top, slightly toward one edge.

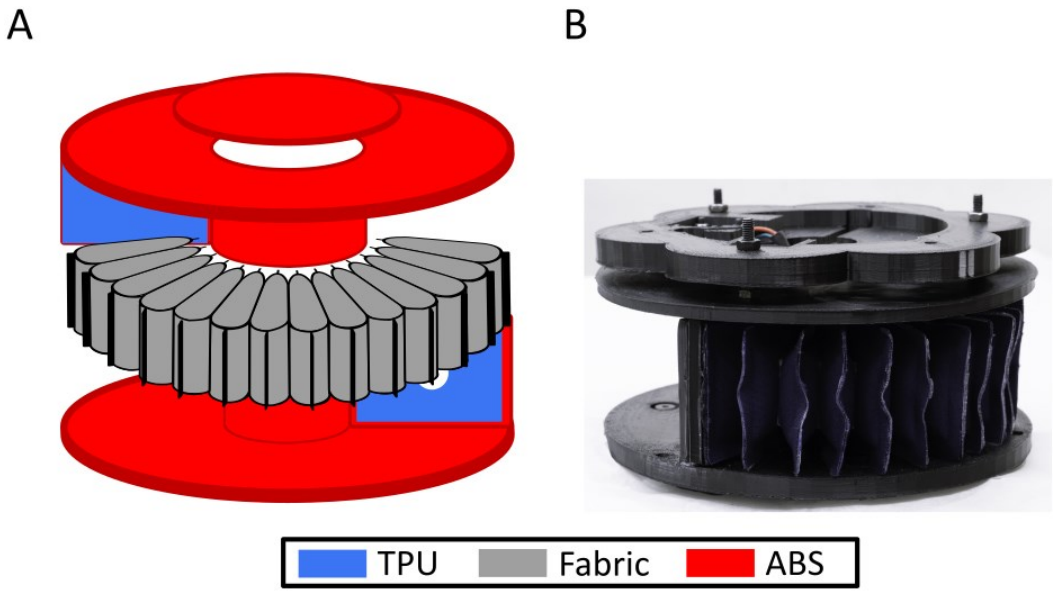

Figure 3.2. A revolute actuator. (A) Components of the actuator: blue colored regions are TPU film, the black and gray part is a fabric bellows actuator, and the red parts are rigid 3D printed components; (B) a complete actuator.

3.3.2 Roll-pitch Actuator

Section B, in Figures 3.1 and 3.3, is a roll-pitch actuator composed of three bellows structures arranged in parallel. Each bellows actuator has an outer diameter of 5.5cm and a total height of 20cm with 11 chambers. Each chamber is bonded at the center of the interconnection area. Three bellows actuators are connected to each other with fabric at the

edge of each chamber in the bellows in order to prevent them from buckling during operation. Each bellows actuator is connected to an air tubing via a tube fitting respectively.

Each bellows actuator operates independently, extending under positive pressure or contracting with vacuum. When one of the bellows is inflated, the roll-pitch actuator bends away from it and towards the other bellows which are under vacuum. Similarly, two bellows can be inflated and one placed under vacuum. Note that at least one of the bellows actuators is always fully contracted with vacuum, so that the top plate of the roll-pitch actuator essentially "rolls" around the bottom on a continuous arc. By inflating different bellows actuators, the roll-pitch actuator can bend to an angle of -90 to 90 degrees in pitch and roll angles. This actuator similarly has an IMU embedded in the top ABS structure, and weighs around 300g.

3.3.3 Body Structure

Section C is also composed of an inflatable structure between 3D printed ABS plates. Unlike section B, its middle part is constructed from two sheets of textiles, including 6 chambers, which are interconnected via a single tube fitting. The middle section is connected with both end structures. In the robot, it functions as a robot body segment when pressurized and left inflated.

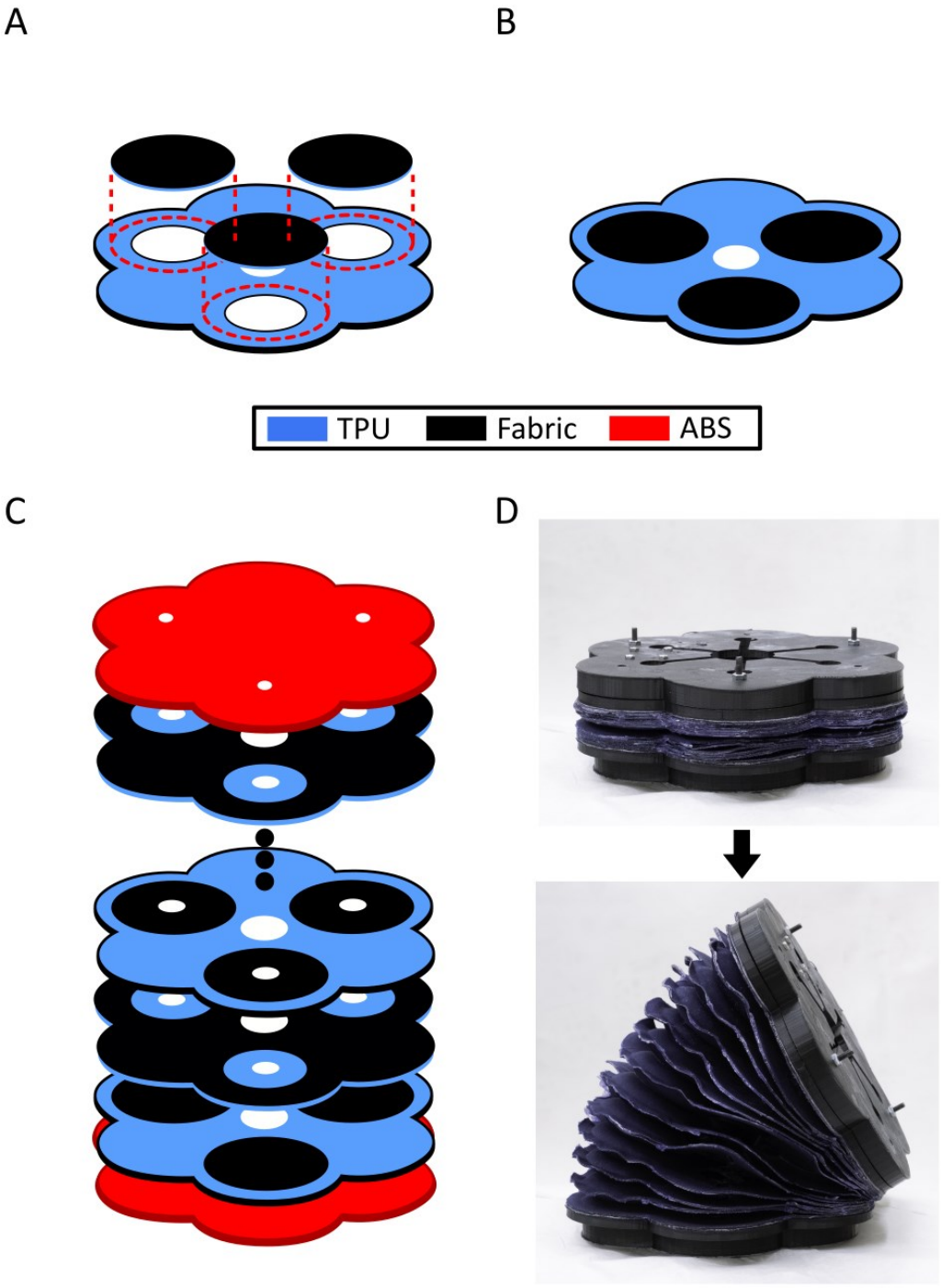

Figure 3.3. Design and fabrication process of a roll-pitch actuator. (A) fabrication method to make a single layer of a chamber: A TPU laminated fabric sheet has three holes, and inner circle layers bond to the proper positions with red line; (B) a complete single layer of a bellow chamber; (C) a layered manufacturing process to make a whole joint actuator; (D) photos of a complete roll-pitch actuator.

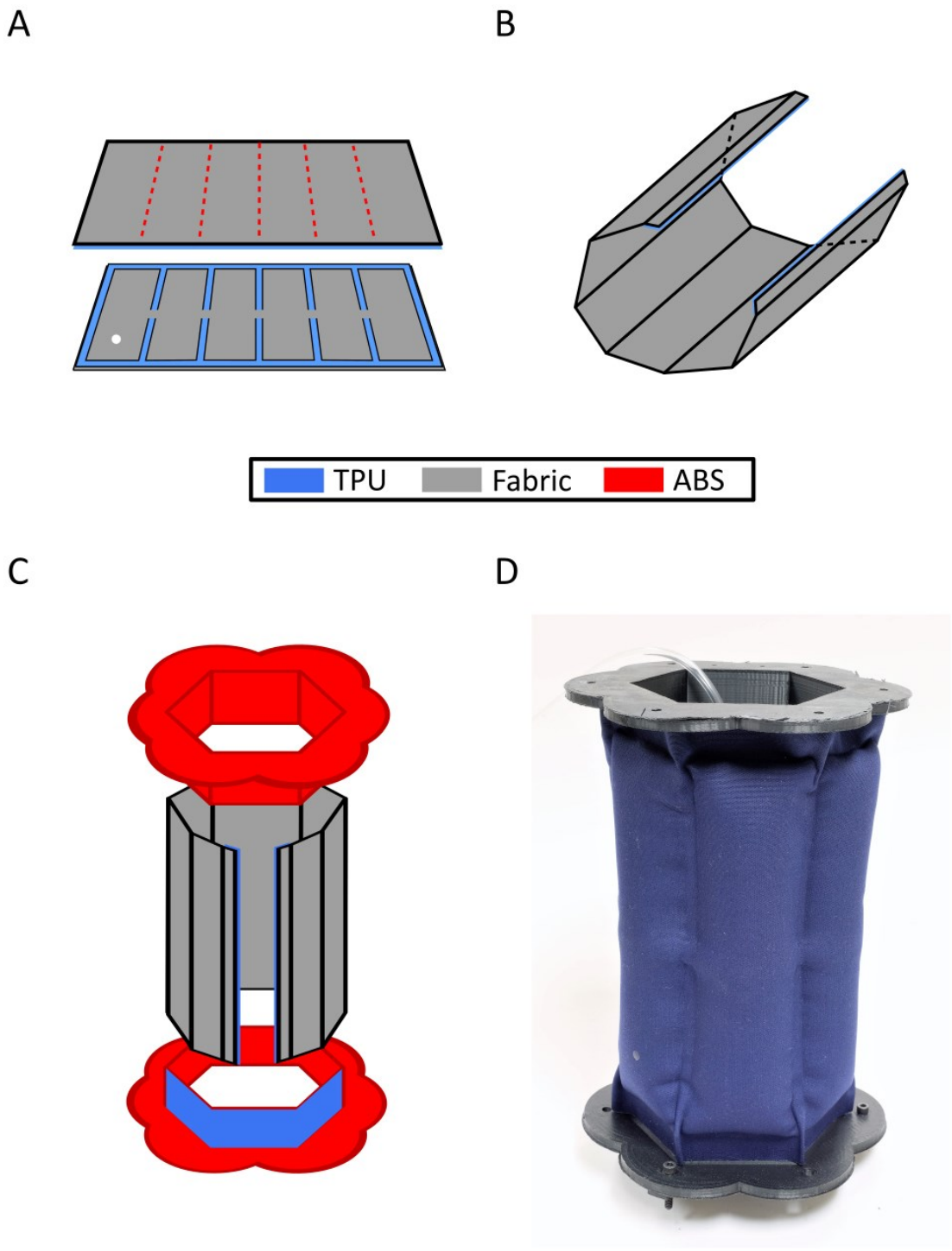

Figure 3.4. A body segment. (A) Fabrication process to make a center part of the body component; (B) a complete center fabric assembly; (C) sub-components of the body segment: the red parts are 3D printed ABS, and the black and gray part is an inflatable

3.4 Kinematics

We first modeled the roll-pitch actuator and the revolute actuator in 3D space. Each actuator operates by positive or negative air pressure, and its position is set depending on the difference of bellows actuator lengths. In Figure 3.5, we use the readings α, β, and γ as Euler angles from each IMU, which is defined to be in the actuator space. Using these angles, we compute the yaw and frame angle for the actuator, and then using these we compute the length of each actuator. The yaw and frame angles and actuator lengths are all part of the configuration space. Using the robot's overall kinematics, we can compute the task space and position of the end effector from the variables in the configuration space. The variables used in the configuration space and task space are described later in this section.

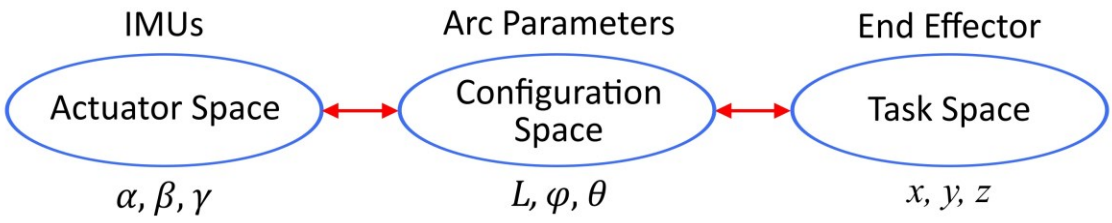

Figure 3.5. Operating spaces of a proposed manipulator and its definitions. Joint space is determined by IMUs information, and the space is converted to the configuration space and task space. Each space is in Cartesian coordinates.

3.4.1 One-DOF Revolute actuator

The 1-DOF revolute actuator is easily modeled. In Figure 3.6, L is the length between the origin to an average radius of the bellows actuator. The bellows actuator can be modeled using the equation $L_b = L\gamma$, where L is the radius from the center of the joint to the midpoint of the bellows, γ is the angle rotated by the actuator and L_b is the total length of the bellows at the radius L.

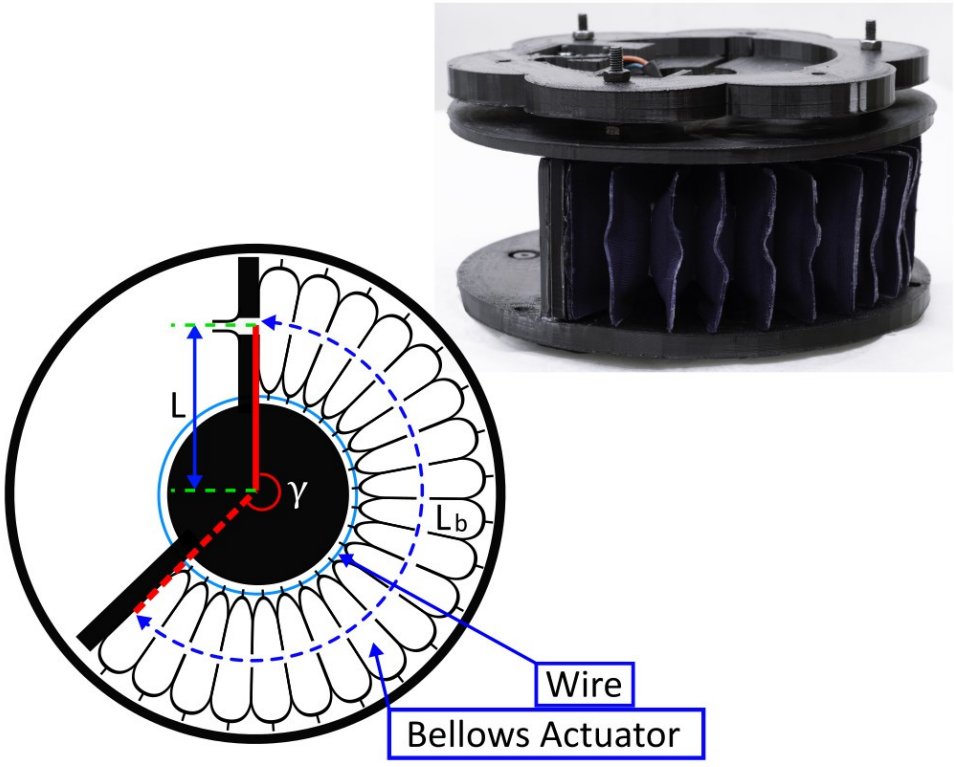

Figure 3.6. A schematic figure of a one-DOF revolute joint actuator

3.4.2 Two-DOF Roll-pitch actuator

3.4.2.1 Forward Kinematics

We model a two-DOF yaw-pitch actuator of a soft/rigid hybrid manipulator with a variant of the piecewise constant-curvature (PCC) model, which is widely used for continuum manipulators. The PCC model represents how a continuum actuator deforms with a constant curvature. If a continuum actuator's path has a specific curvature, the assumption enables the calculation of the end effector's position. In general, continuum manipulators change the specific curvature at each point in time by altering the chamber pressures or by retracting cables connected on the outsides of the chambers.

The roll-pitch actuator in this paper uses a similar principle and model but with one key difference. Specifically, at least one chamber is always kept under vacuum. This causes one or two of the bellows to be fully compressed, which leads the actuator to always have the same curvature. This can be seen in Figure 3.8A where the actuator follows a fixed arc if it curls in one direction. Therefore, we set the constant radius of the curvature (R) from the center point of the arc, which is the actuator's real path, to the origin, then we model the roll-pitch actuator with yaw angle (φ) and frame angle (θ) in Figure 3.8B and 3.8C.

The roll-pitch actuator contains an inertial measurement unit (IMU) embedded in the top ABS plate. The orientation of the top plate is used with the kinematic models to determine the actuator's angles and position. The IMU senses the roll and pitch angles instead of yaw and frame angles, but the modeling is easier in terms of the yaw and frame angles.

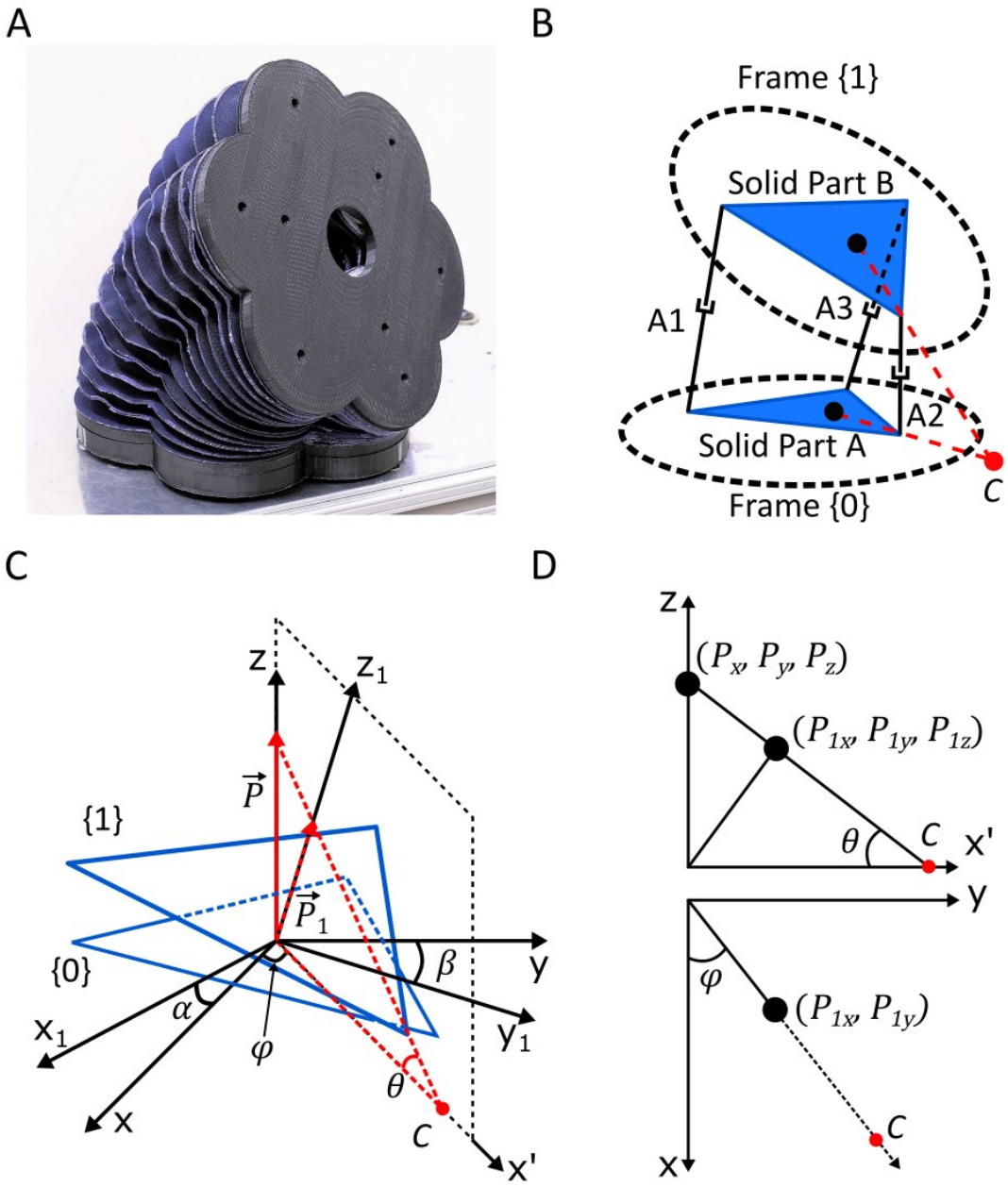

Figure 3.7. A description of a joint actuator with an IMU. (A) a real actuator; (B) a schematic figure of the actuator: Blue colored triangles are the ABS plates, and A_n ($n = 1,2, and\ 3$) are the bellows actuators; (C) two coordinates {0, 1} for conversion from the IMU to joint space; (D) detailed description how to find yaw angle (φ) and frame angle (θ).

In Figure 3.7A and 3.7B, the actuator is operated and controlled by the length of each bellows (A1, A2, and A3) during inflation and deflation. Due to the difficulty of precisely modeling a fabric bellows actuator shape, we consider the following assumption: each bellows operates with linear motion when it is inflated or deflated. Thus, the three bellows are considered as prismatic joints. We set a frame {0} where solid part A is located, and a frame {1} at solid part B. We next set point C as the center point of the arc, and this point moves on the x-y plane depending on the actuator's motion. As follows Figure 3.7C, two coordinates are described for the roll-pitch actuator. The first coordinate in the frame {0} is attached at the at the center of the solid part A, and the second coordinate in the frame {1} is located at the center of the solid part B. We also set $\vec{P} = [P_x, P_y, P_z]^T = [0, 0, 1]^T$ on frame {0}, and $\overrightarrow{P_1} = [P_{1x}, P_{1y}, P_{1z}]^T$ on frame {1} as two reference vectors.

When three actuators are inflated or deflated, the $\overrightarrow{P_1}$ changes its position as follows:

$$\overrightarrow{P_1} = \begin{bmatrix} \sin(\beta) \\ -\cos(\beta) \times \sin(\alpha) \\ \cos(\beta) \times \cos(\alpha) \\ 1 \end{bmatrix} \tag{3.1}$$

where β is a roll angle and α is a pitch angle from the IMU. From this $\overrightarrow{P_1}$ position, $\overrightarrow{P_1}$ can be projected on the x-y plane or the x'-z plane in Figure 3.7D, and then we have,

$$\varphi = \tan^{-1}(P_{1y}/P_{1x}) \tag{3.2}$$

$$\theta = \cos^{-1}(P_{1z}) \tag{3.3}$$

where φ is a yaw angle and θ is a frame angle. Note that the yaw angle (φ) does not mean that the roll-pitch actuator is rotated around the z-axis. We just need the yaw angle and the frame angle of the roll-pitch actuator as converted parameters from the roll and pitch angles. Using the two angles, the point $C = [C_x, C_y, C_z]^T$ can be determined as follows:

$$C_x = R \times \cos(\varphi) \tag{3.4}$$

$$C_y = R \times \sin(\theta) \tag{3.5}$$

Finally, the position of the point C is determined. However, using the IMU sensor, we do not know how much the frame {1} translates from the frame {0}. The translation point should be on the arc. Therefore, we need to know translated coordinate position as in Figure 3.8C. As mentioned above, the actuator moves on a continuous arc, which is a reference path with green, then the translation position can be calculated,

$$B_x = R(1 - \cos(\theta)) \times \cos(\varphi) \tag{3.6}$$

$$B_y = R(1 - \cos(\theta)) \times \sin(\varphi) \tag{3.7}$$

$$B_z = R \times \sin(\theta) \tag{3.8}$$

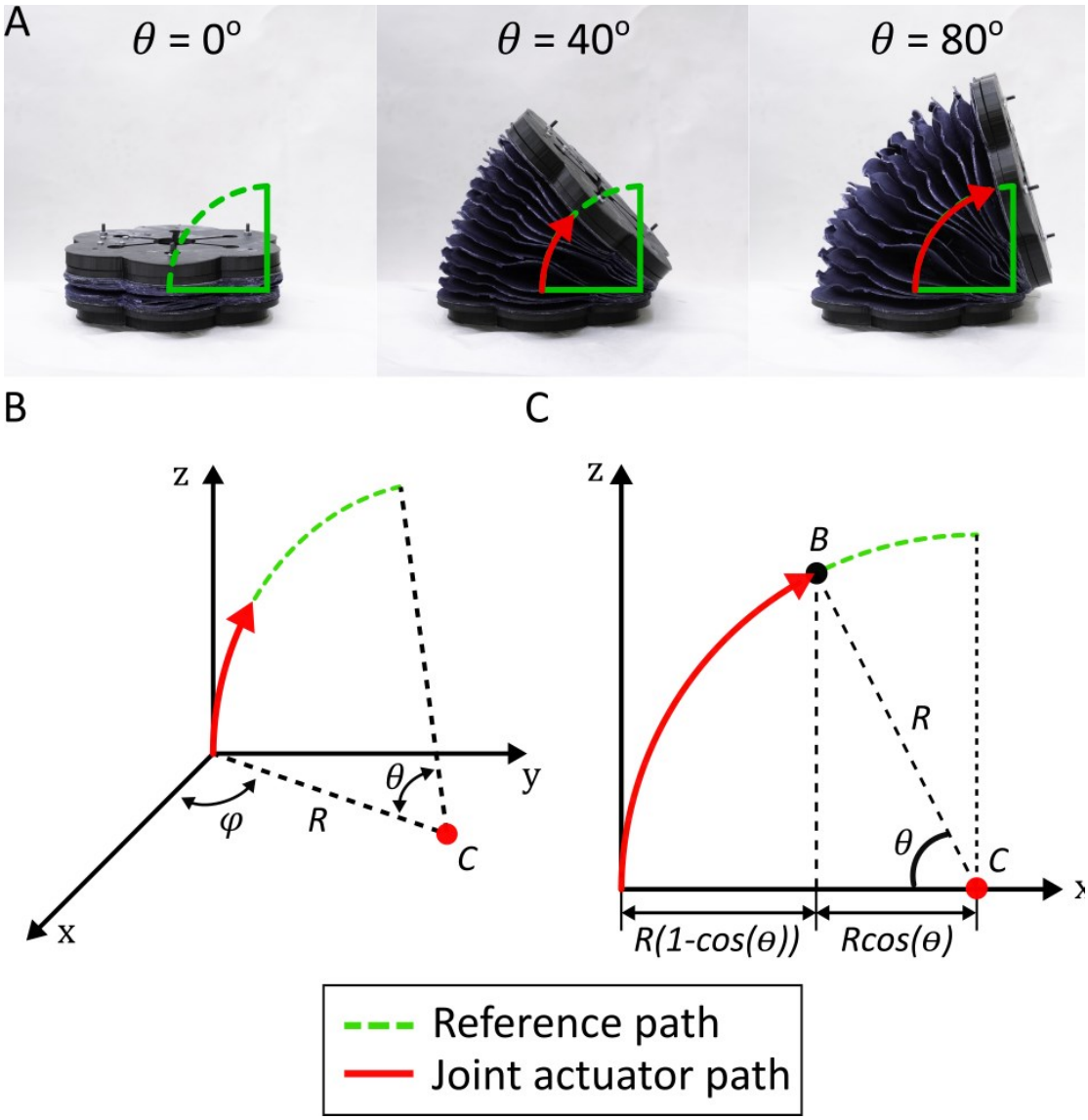

Figure 3.8. A schematic figure of how to find the joint actuator's position using an IMU sensor. (A) A motion of a real joint actuator; (B) Actual modified kinematics; (C) Calculation method to find the translation point.

where $B = [B_x, B_y, B_z]^T = [x, y, z]^T$ is the position of B in the frame {1} as the end effector position of the solid part B. Finally, the actuator's matrix equation is:

$$\vec{T}_{JA} = \begin{bmatrix} \cos\beta & 0 & \sin\beta & B_x \\ \sin\alpha\sin\beta & \cos\alpha & -\sin\alpha\cos\beta & B_y \\ -\sin\beta\cos\alpha & \sin\alpha & \cos\alpha\cos\beta & B_z \\ 0 & 0 & 0 & 0 \end{bmatrix} \tag{3.9}$$

As follows the transformation matrix ($\vec{T}_{JA}$), a position of each actuator in frame {1} is calculated by multiplying $\vec{T}_{JA}$ to each position of $A1$, $A2$, and $A3$ in the frame {0}. Finally, each actuator length $L = [L_A, L_B, L_C]^T$ can be estimated by two positions in the frames {0} and {1}.

3.4.2.2 Inverse Kinematics

For an autonomous system, inverse kinematics are required to find three actuators' lengths for proper motion from a desired end effector position. From Equation 3.6 to 3.8, an estimated frame angle (θ) and a yaw angle (φ) from the desired position (B) are:

$$\theta = \sin^{-1}(B_z/R) \tag{3.10}$$

$$\varphi = \sin^{-1}\{B_y/(R(1-\cos\theta))\} \tag{3.11}$$

Based on two angles, the point C can be determined from Equation 3.4 and 3.5. The reference vector of $\overrightarrow{P_1} = [P_{1x}, P_{1y}, P_{1z}]^T$ is also calculated using Equation 3.2 and 3.3. Next, from Equation 3.1, desired roll and pitch angles are:

$$\alpha = -\tan^{-1}(P_{1y}/P_{1z}) \tag{3.12}$$

$$\beta = \sin^{-1}(P_{1x}) \tag{3.13}$$

Given all angles, each actuator length can be determined. In our system, we design and model the actuator to move from -90 to 90 degrees of a roll angle and pitch angle.

3.5 Control system

3.5.1 Hardware

A hardware control system has been developed using proportional valves, pneumatic pumps, sensors (pressure sensors and IMUs), and a microcontroller (Arduino MEGA 2560 R3).

The pneumatic manipulator has a number of joint actuators based on the desired robot topology. Each bellows within an actuator requires two proportional valves, which are connected via a T-fitting to a single tube extending to the bellows. One of the valves

controls the positive pressure, and the second controls the vacuum. Only one of the valves is operated at a time, due to the shared tube. Each one-DOF revolute joint needs two valves, each two-DOF roll-pitch actuator requires six valves, and each body segment needs two valves.

A schematic figure of the manipulator's control system is shown in Figure 3.9. We used an air regulator to control the central air pressure from a wall-mounted air source in order to inflate the actuators. A vacuum pump (Parker T2-01 High Flow Diaphragm Pump (P/N: T1-2HD-12-1NEA)) is also used for deflating the actuators. The closed-loop PID control system controls each proportional valve.

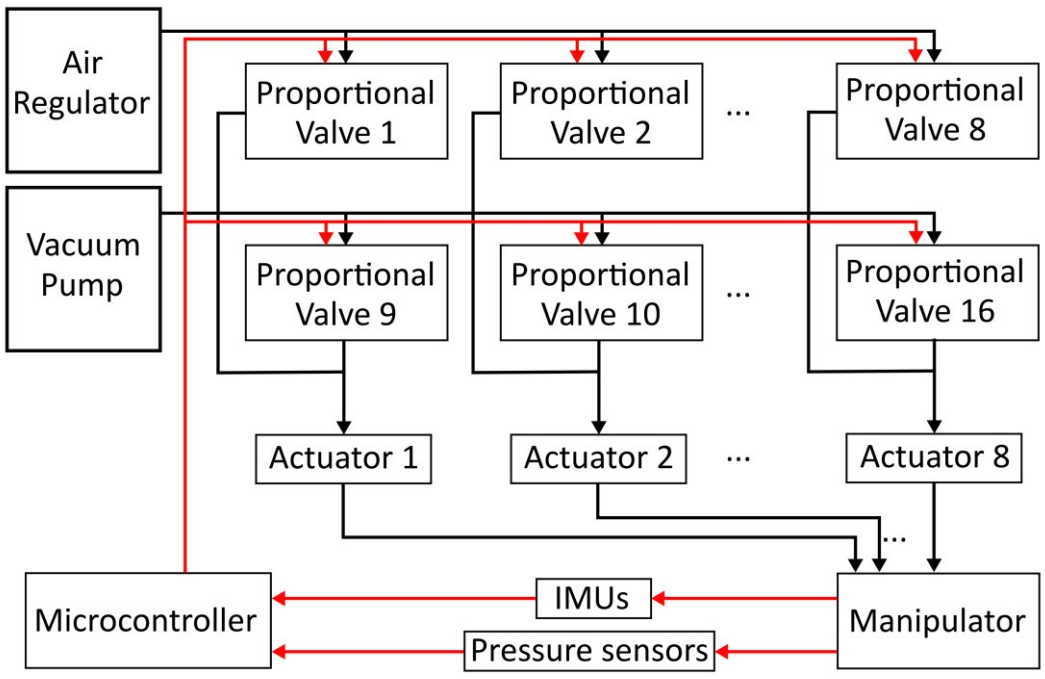

Figure 3.9. A schematic figure of manipulation control system. A red line is to describe electrical circuit, and a black line is to describe air path.

3.5.2 Controller and Algorithm

The PID control system is described in Figure 3.10. Two angles (α, β) of the roll-pitch actuator are measured by an IMU sensor in the actuator, and the pressure sensors monitor the actuator's pressure in real time. In addition, a yaw angle (φ) and a frame angle (θ) of the actuator are calculated by the kinematics, then each actuator is controlled. The two proportional valves for each bellows actuator are controlled separately. To prevent them from both being open at the same time, small deadbands are set in the system.

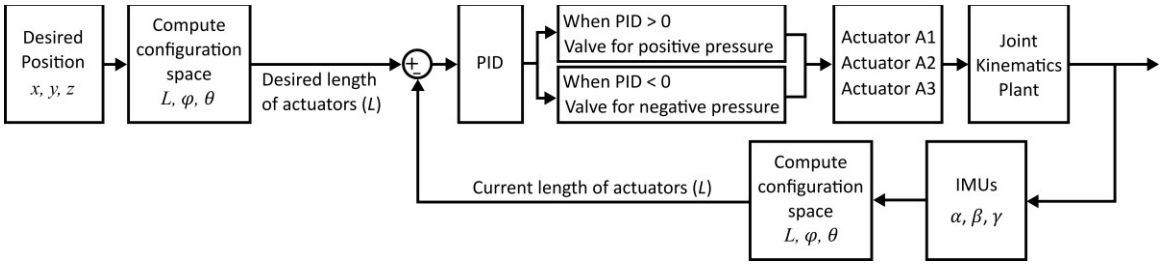

Figure 3.10. Manipulation control system

The roll-pitch actuator follows the algorithm described in Figure 3.11. Note that each bellows actuator (A1, A2, and A3) occupies a part of the range of the yaw angle (φ) on the x-y plane. The first bellows actuator (A1) is located between 0° and 120°. The second bellows actuator (A2) is placed in the range of 120° to 240°, and the last actuator (A3) is located between 240° and 360°.

The position of the point C and desired lengths of the three bellows (A1, A2, and A3) are determined following the kinematics. The control system decides two bellows

actuators to be placed under positive pressure and one to be under vacuum using the C position. When the desired tip position is set, the C position will fall within the yaw angle range of one of the bellows actuators. The system then places that actuator under vacuum. In other words, the bellows that the roll-pitch actuator is curling towards is placed under vacuum. Then, the other two actuators are controlled to move the entire roll-pitch actuator to the desired tip position.

Algorithm. Controller

Procedure Title | Inflation/Deflation Priority

Note | PID value $\longrightarrow$ $PID_{P\ AB\ or\ C}$ for a positive pressure
| PID value $\longrightarrow$ $PID_{N\ AB\ or\ C}$ for a negative pressure

Input | B_x, B_y, B_z

for $n=1...N$

$\theta_{desired}$, $\varphi_{desired}$ $\longleftarrow$ B_x, B_y, B_z

$\alpha_{desired}$, $\beta_{desired}$ $\longleftarrow$ $\theta_{desired}$, $\varphi_{desired}$, $\vec{P}_{desired}$, $\vec{P}_{1\ desired}$

$L_{A\ desired}$, $L_{B\ desired}$, $L_{C\ desired}$, $C_{desired}$ $\longleftarrow$ R, $\alpha_{desired}$, $\beta_{desired}$

α, β $\longleftarrow$ $IMUs$

L_A, L_B, L_C $\longleftarrow$ R, α, β

$L_{\Delta A}$, $L_{\Delta B}$, $L_{\Delta C}$ $\longleftarrow$ $L_{A\ desired} - L_A$, $L_{B\ desired} - L_B$, $L_{C\ desired} - L_C$

if $0^o < C_{desired} < 120^o$

$PID_{PA} = 0$, $PID_{NA} = High$
$PID_{PB} = PID_{PB}$, $PID_{NB} = PID_{NB}$
$PID_{PC} = PID_{PC}$, $PID_{NC} = PID_{NC}$

else if $120^o <= C_{desired} < 240^o$

$PID_{PB} = 0$, $PID_{NB} = High$
$PID_{PA} = PID_{PA}$, $PID_{NA} = PID_{NA}$
$PID_{PC} = PID_{PC}$, $PID_{NC} = PID_{NC}$

else

$PID_{PC} = 0$, $PID_{NC} = High$
$PID_{PA} = PID_{PA}$, $PID_{NA} = PID_{NA}$
$PID_{PB} = PID_{PB}$, $PID_{NB} = PID_{NB}$

end

return

Figure 3.11. Control Algorithm

3.6 Actuator Modeling and experiments

We next model a bellows actuator and the two joint actuators so we can predict the behavior of a robot arm made with them.

3.6.1 A bellows actuator

We model a single bellows actuator using a variable-stiffness spring, and present a mathematical model and experiments for it, since it is a subcomponent of each joint actuator. A single pouch within a bellows is modeled using a spring with a stiffness parameter of k_{pouch} and a total length of a pouch (x_{pouch}) in Figure 3.12A. The force output is determined by the pressure (P) inside the chamber and the contact area (A) at the end. A total force is affected by a restoring force as follows,

$$F_{total} = F_{output} - F_R = PA - k_{pouch}x_{pouch} \tag{3.14}$$

where F_R is a total restoring force.

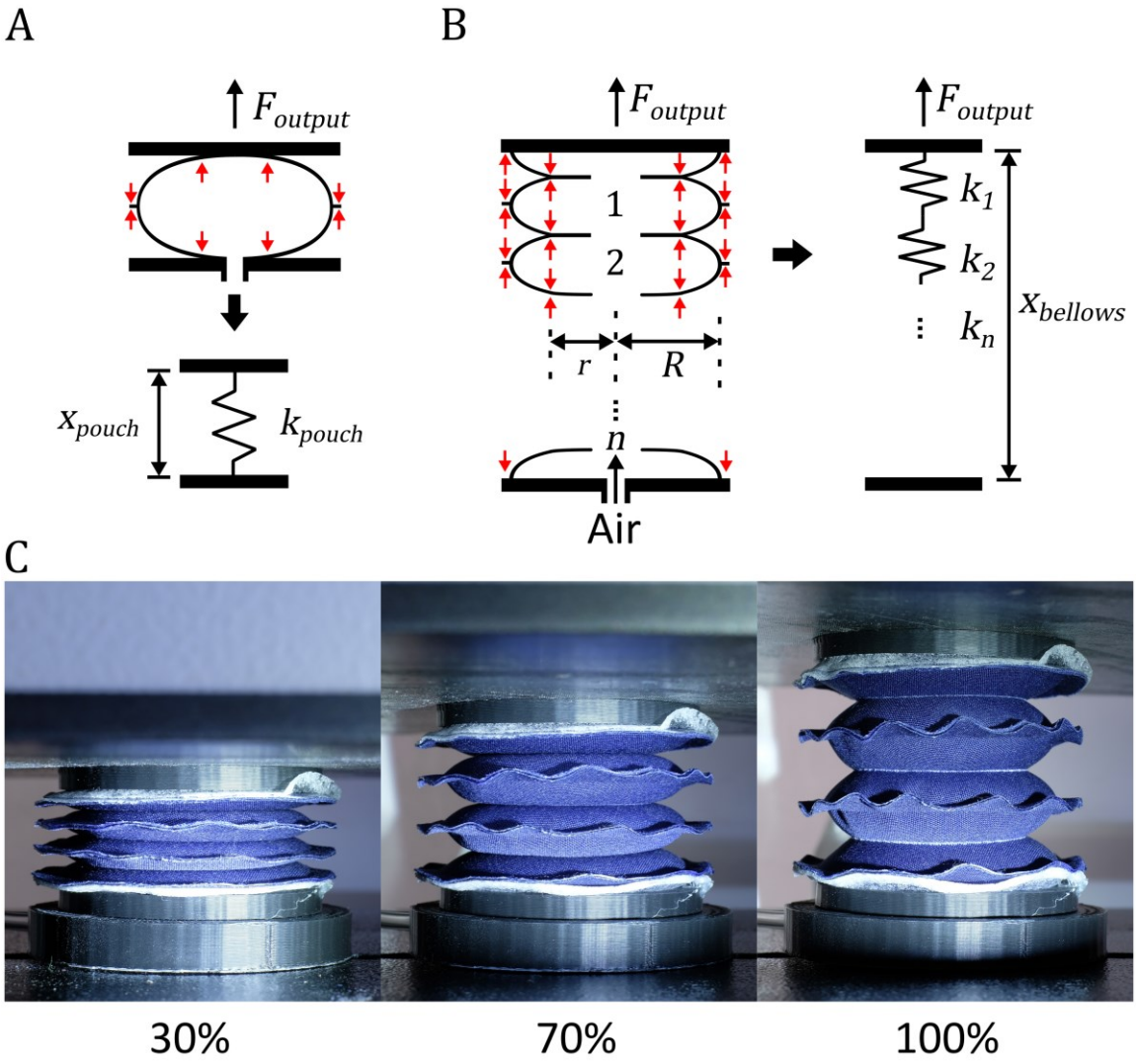

Figure 3.12. A mathematical model. (A) a model of a single chamber; (B) a model of a bellows actuator; (C) a real actuator with different range of its motion.

The stiffness parameter (k) is not constant. That is because the structures are constructed using fabric and contain outer seams and inner seams. Each seam has different angles depending on the pressure and the total length of a pouch (x_{pouch}) in Figure 3.12A. In figure 3.12C, a bellows actuator shows different geometries within different parts of its range of motion. With expansions of less than 70% of its full range of motion, the adjacent

pouches make contact with each other around their inner seams. Due to this, the stiffness is dominated by the pouch's geometry, the outer seams, and the fabric stretching. At the 70% inflation point, each pouch loses contact with the adjacent pouches, and then the stiffness of inner seam and associated geometry changes add to the total stiffness. The stiffness and fabric stretching are proportional to pressure and vary with the actuator displacement, making it very challenging to further decompose the specific contributions to the pouch's stiffness. Therefore, we assume the stiffness parameter k_{pouch} represents a stiffness of a pouch.

Using the model of a single pouch, we can also model a bellows actuator with multiple pouches. The bellows actuator contains *i* pouches, so the bellows actuator's range of motion can be considered as,

$$x_{bellows} = i * x_{pouch} \tag{3.15}$$

where *i* is the number of chambers. The stiffness can also be expressed as,

$$k_{bellows} = \frac{k_{pouch}}{i} \tag{3.16}$$

also, the total force is calculated as

$$F_{total} = PA - k_{bellows}x_{bellows} \tag{3.17}$$

We tested and simulated a bellows actuator with 5 pouches (5.5cm outer diameter, 3.5cm intersection diameter), and where the actuator had ABS plates attached to both ends. The test was conducted under 34.5, 69.0, 103.4, 137.9, 172.4, and 206.8kPa, and the results plotted in Figure 3.13.

From the experimental data in Figure 3.13B, we confirmed that the actuator has a constant stiffness value until it is inflated around 70% of the range of actuator's motion, and this stiffness varies based on the pressure. We calculated numerical derivatives of the data in Figure 3.13A in two regions, for points up to 70% of the final actuator lengths and for points at larger displacements. Using the numerical derivative, the relationship between the actuator's stiffness ($k_{bellows}$) and pressure (P) until 70% of range of the motion can be expressed as

$$k_{bellows} = a_1 P + a_2 \tag{3.18}$$

where a_1 and a_2 are constant coefficients from a curve fit, with values of 0.177 and 3.07 respectively. In the range from 70% to the full range of the motion, the relationship between pressure and the stiffness can be described as

$$k_{bellows} = (b_1 P + b_2) x_{bellows} + (c_1 P + c_2) \tag{3.19}$$

where b_1, b_2, c_1, and c_2 are constant coefficients from fitting the data, with values of 0.128, 0.792, -0.807, and 15.1 respectively. Additionally, the maximum actuator displacement varies based on the different pressures, and the relationship between these can be fit by the function

$$x_{bellows\_max} = d_1 P^4 + d_2 P^3 + d_3 P^2 + d_4 P + d_5 \tag{3.20}$$

where d_1, d_2, d_3, d_4 and d_5 have values -2.2e-09, 1.4e-06, 0.38e-03, 0.058, and 5.59 respectively. Using this model, we plotted the dashed lines in Figure 3.13B, which can be seen to closely match the experimental data.

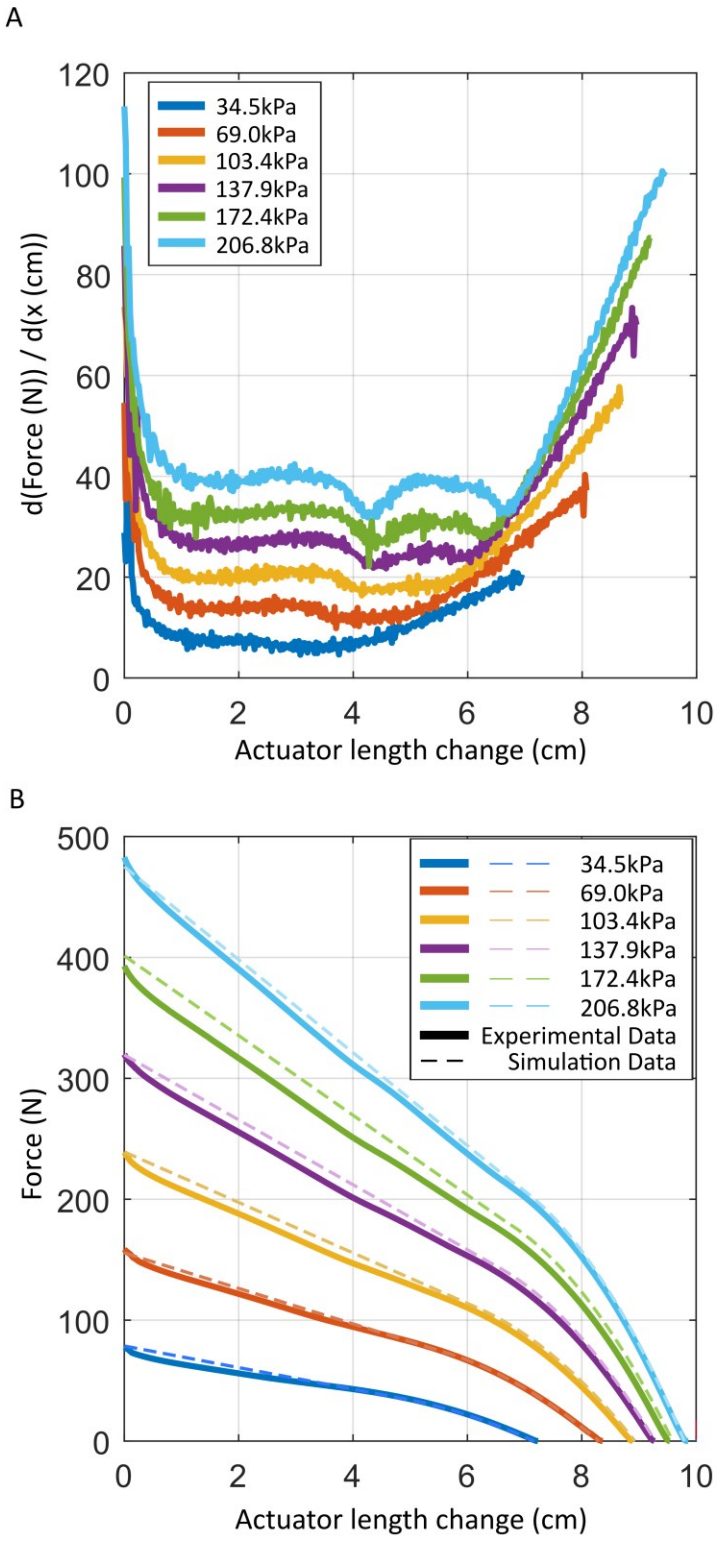

Figure 3.13. (A) A numerical derivative of the data in Figure 13B; (B) an experimental data and a simulation data of a bellows actuator with five chambers.

3.6.2 Roll-pitch actuator modeling

We next model and test an entire single roll-pitch actuator to predict deformation of the robot end effector. Using the model of a bellows actuator above, we describe the roll-pitch actuator with three springs (Figure 3.14A). In order to model an accurate length of each actuator (L_A, L_B, and L_C), Figure 3.14B shows a top view of the base. Recalling its kinematics, the point C can be found from the yaw angle (φ). According to the coordinates of the base, an angle of q can be calculated for each bellows actuator as $q_i = \{(90 + 120(i-1)) - \varphi\}$ $(i = 1,2, and\ 3)$. Using these angles, the radius of curvature for each bellows actuator is calculated as

$$R_i = R - d\cos q_i \ \ (i = 1,2, and\ 3) \tag{3.21}$$

and L_A, L_B, and L_C are also calculated from $L_n = R_i\theta$.

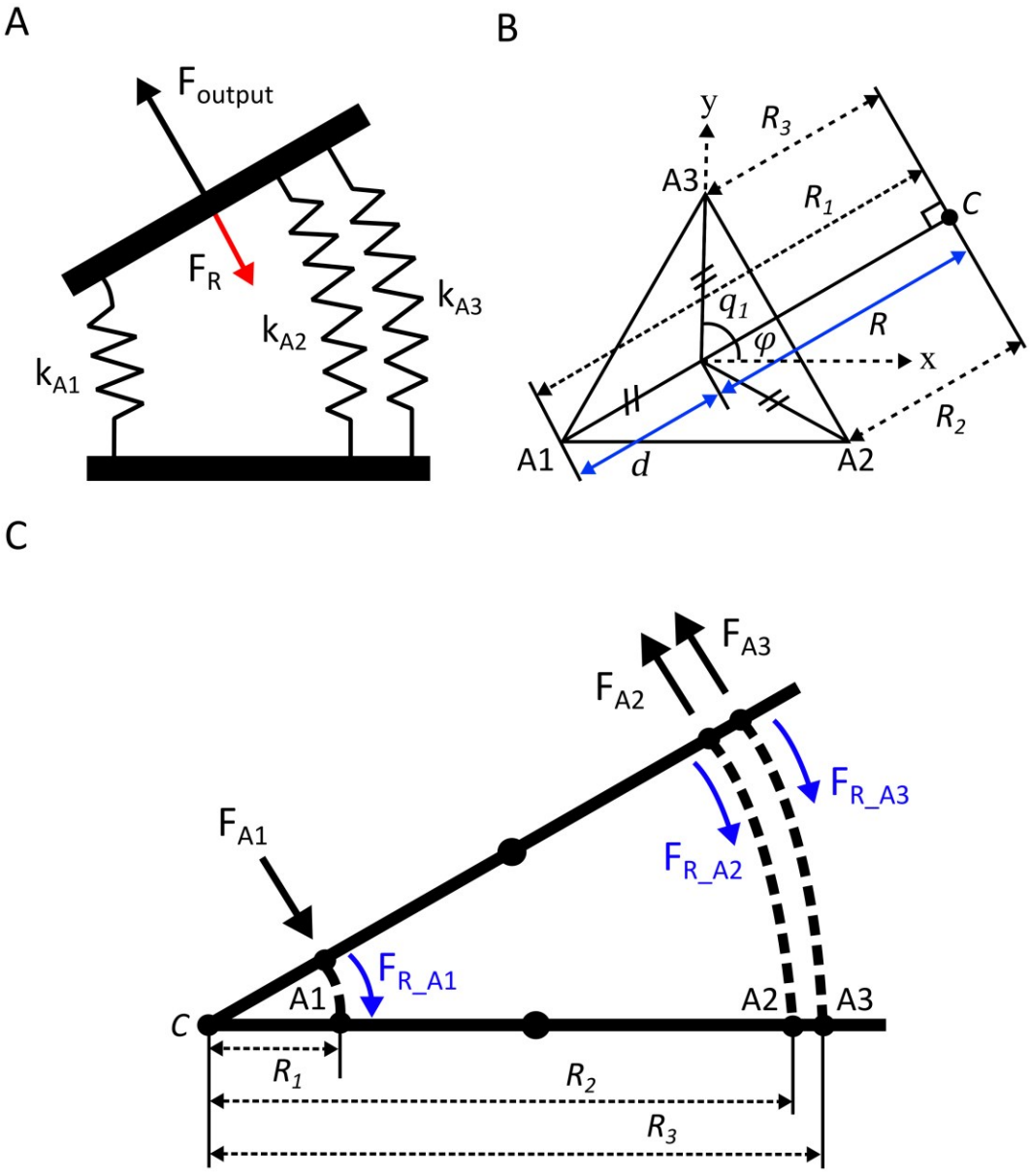

Figure 3.14. A mathematical model. (A) a model of a joint actuator; (B) top view of the actuator to find lengths of each bellows actuator (L_A, L_B, and L_C); (C) a model of a single joint actuator with forces by pressure and restoring forces by fabric.

According to the desired frame angle (θ), a desired actuator length is calculated, and we can predict how much pressure the actuator needs to reach the desired angle. In addition, compared to pressure and actuator length, the stiffness can be predicted.

In Figure 3.14C, a model of a single joint actuator is described with outward forces from pressure and restoring forces from fabric. In this case of the actuator, its point C, which is the radius of curvature of the center position, is always placed on the edge of the joint actuator as a pivot point. We modeled the actuator with the case that a single actuator (A1) is under vacuum. According to the pivot point, the actuator's force equilibrium is modeled as

$$\frac{R_1}{(R_2+R_3)/2}F_{A1} - F_{R\_A1} = F_{A2} + F_{A3} - F_{R\_A2} - F_{R\_A3} \tag{3.22}$$

From the kinematics, L_n is calculated according to a desired angle (θ). Recalling equations 3.18 and 3.19, from the single bellows actuator, each actuator's pressure can be estimated.

We tested a complete roll-pitch actuator to verify this model. Each bellows actuator within it had 11 pouches (5.5cm outer diameter, 3.5cm inner diameter). The sample actuator was tested under two conditions, when one bellows was under vacuum and with two bellows under vacuum, to determine how the predicted positive pressure in the inflated chambers compared to the actual pressure at different frame angles. Each experiment was tested with an electric pressure sensor and an IMU sensor. The IMU sensor was used to log the actuator's orientation. The results are in Figure 3.15.

To simulate the actuator, we ignored the restoring force (F_{R_A1}) of the vacuumed actuator. Putting the equations 3.18 and 3.19 into the equation 3.22, we solved the equation of the relationship between pressure (P) and stiffness of seam ($k_{bellows}$). Vacuum pressure was set to -62kPa. We collected the pressure values when the frame angles were varied. In each case, the data matched with the simulation results within a 5% error. From equation 3.22, we now predict how much pressure the actuator has. We can then also estimate the deformation distance when an axial force is applied based on the predicted pressure and stiffness.

.

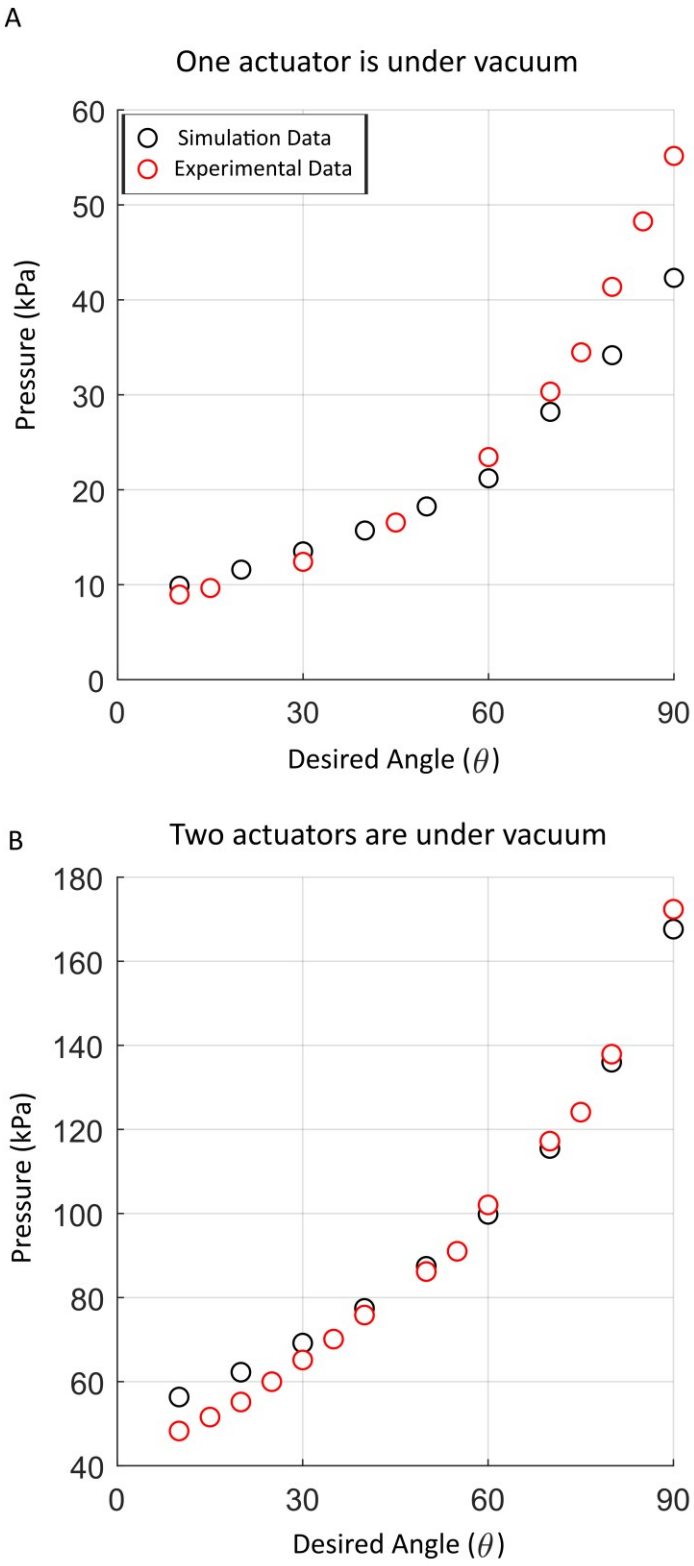

Figure 3.15. (A) Experimental data compared to the simulation data when one actuator is under vacuum; (B) Experimental data versus the simulation data when two actuators are under vacuum.

3.6.3 Roll-pitch actuator stiffness testing

The roll-pitch actuator was tested to measure deformation under axial force. The actuator was tested under the same conditions as the previous experiment in Figure 3.15. A force sensor (ATI Mini 45) was mounted on the top plate of the actuator to measure forces and torques toward different directions. We also used a motion capture system (Qualysis Miquas M1) to measure the end effector position. Three markers were attached on the top of each bellows actuator, and then the end effector position was calculated.

Vacuum pressure was set to -62kPa. For the experiment with one actuator under vacuum, positive pressure was applied to two actuators at 6.8kPa for the 30 degrees case, 23.4kPa for 60 degrees, and 55.2kPa for 90 degrees of the frame angle. For the experiment with two actuators were under vacuum, positive pressure was applied to one actuator at 58.3kPa for 30 degrees, 96.5kPa for 60 degrees, and 165.5kPa for 90 degrees.

According to the model of the actuator, we simulated the deformation displacement under different forces toward the axial direction in Figure 3.16A and 3.16D. These results show that the model has a maximum error of 5% for the first 1.5mm and a maximum error of 12% after 1.5mm.

We additionally tested lateral forces and torques, to completely characterize the stiffness of the actuator. It is very challenging to model how the bellows actuators will deform under lateral loads and torques, so we only provide experimental data. These data can help to predict the end effector motion, if several joint actuators are combined into a robot. The first column in each of Figures 3.16 and 3.17 shows results for when one bellows

is under vacuum, and the second column of each figure shows the results when two actuators are under vacuum.

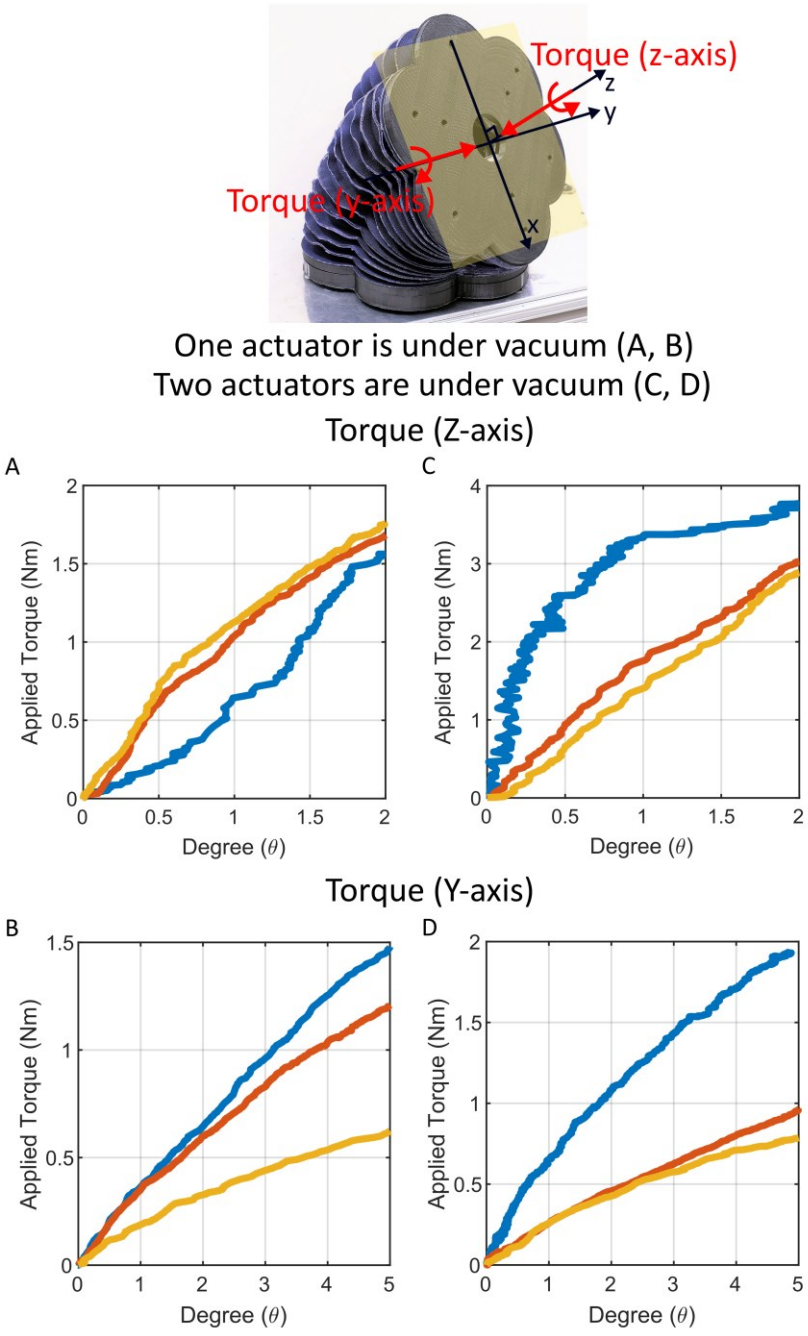

Figure 3.16. Deformation Tests (A) Torque under one actuator is vacuumed to z-axis; (B) Torque under one actuator is vacuumed to y-axis; (C) Torque under two actuators are vacuumed to y-axis; (D) Torque under two actuators are vacuumed to y-axis.

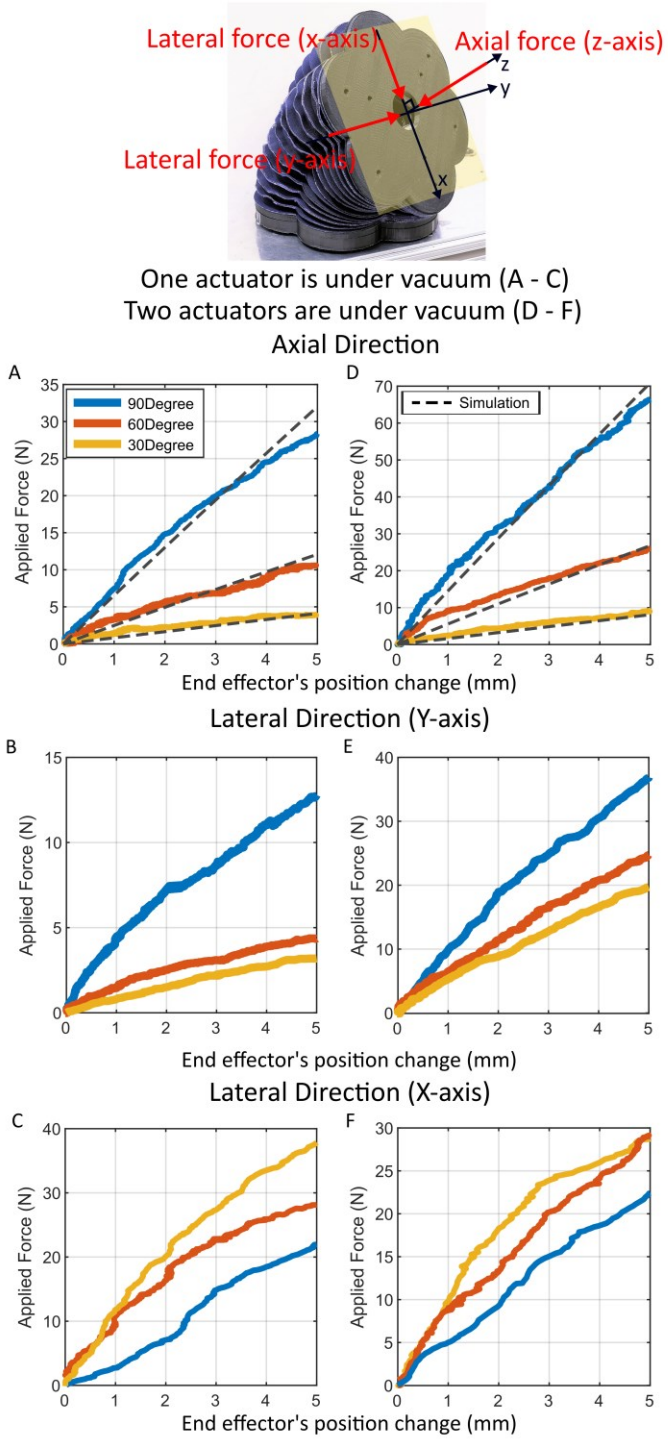

Figure 3.17. Deformation Tests (A) Axial force under one actuator is vacuumed; (B) Lateral force under one actuator is vacuumed to y-axis; (C) Lateral force under one actuator is vacuumed to x-axis; (D) Axial force under two actuators are vacuumed; (E) Lateral force under two actuators are vacuumed to y-axis; (F) Lateral force under two actuators are vacuumed to x-axis.

3.6.4 Complete manipulator stiffness testing

We then computed and tested how the complete manipulator deformed when loaded with different weights on the end effector, with the results in Figure 3.18. The manipulator contains two roll-pitch actuators, two body sections, and a revolute actuator. We set the first roll-pitch actuator to have 60 degrees of the frame angle, and the second roll-pitch actuator to have 30 degrees of the frame angle. Each actuator has the same condition with two bellows actuators under vacuum (-62kPa). Positive pressure was applied to the third bellows in the first roll-pitch actuator at 96.5kPa, and the third bellows actuator in the second roll-pitch actuator was at 58.3kPa to achieve their respective frame angles. The manipulator is controlled with an open loop system, so the pressures stayed constant. Different vertical forces from 0.5N to 3N were applied to the end effector.

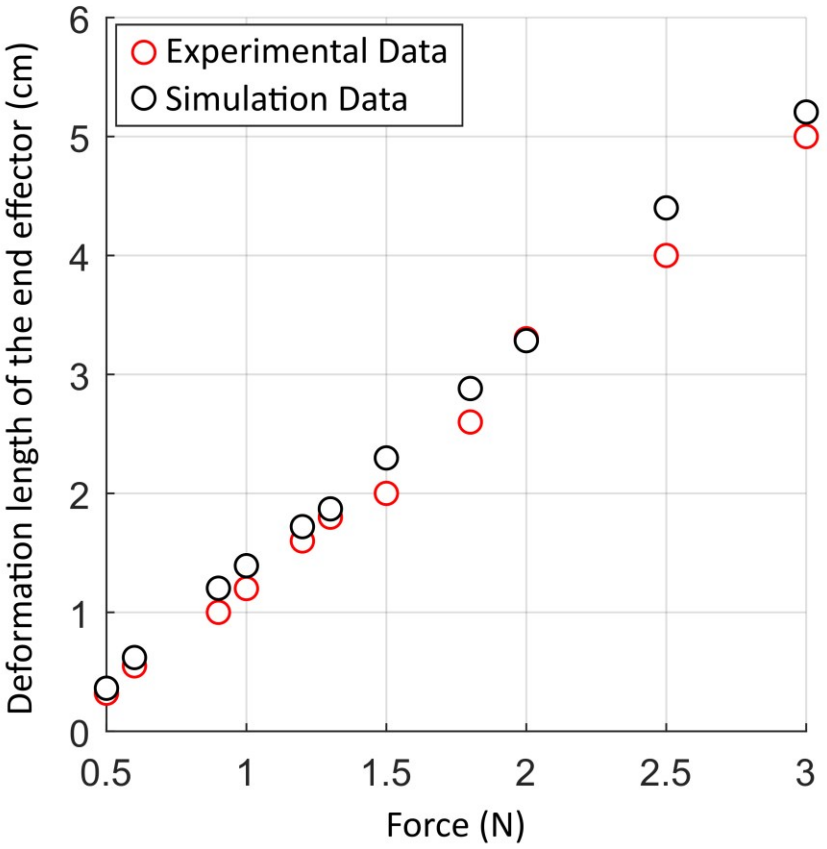

Figure 3.18. Deformation Tests to compare between experimental data and simulation data to predict how the manipulator responds to external loads at its end effector.

3.7 experimental Results

We next tested a revolute actuator and a roll-pitch actuator separately to prove how well the actuators can move to a desired position. In addition, a few different combinations with other actuators were built and tested. Three tests for a single actuator and a manipulator with a roll-pitch actuator and a revolute actuator were conducted by controlling using inverse kinematics. The final test of a complete four-DOF manipulator was tested under forward kinematics. For all tests, to analyze its motion, the end effector position is measured by using a reflective marker at the center point of the top plate.

Tests were first conducted with a roll-pitch actuator. One of the three bellows actuators of the roll-pitch actuator was inflated, while two were under vacuum. Two proportional values were controlled for positive and negative pressure respectively. A PID controller was developed with small deadbands, and results from it for the roll-pitch actuator are shown in Figure 3.19A.

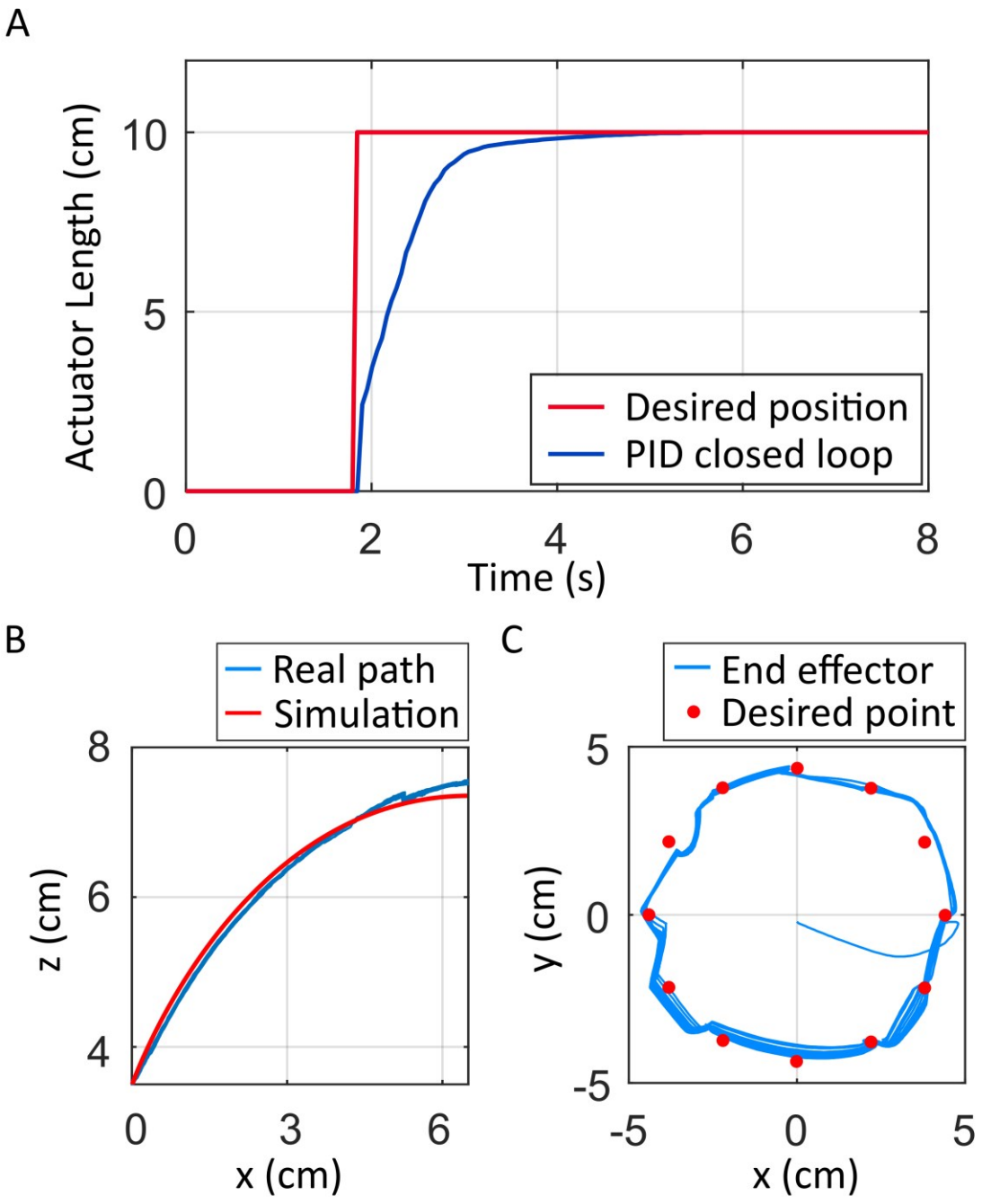

Figure 3. 19. An experimental data about the two-DOF joint actuator. (A) PID control system for a single bellows actuator; (B) A comparison data plot how well the kinematic model represents the real path; (C) An actuator's path in the trajectory under the fixed yaw angle.

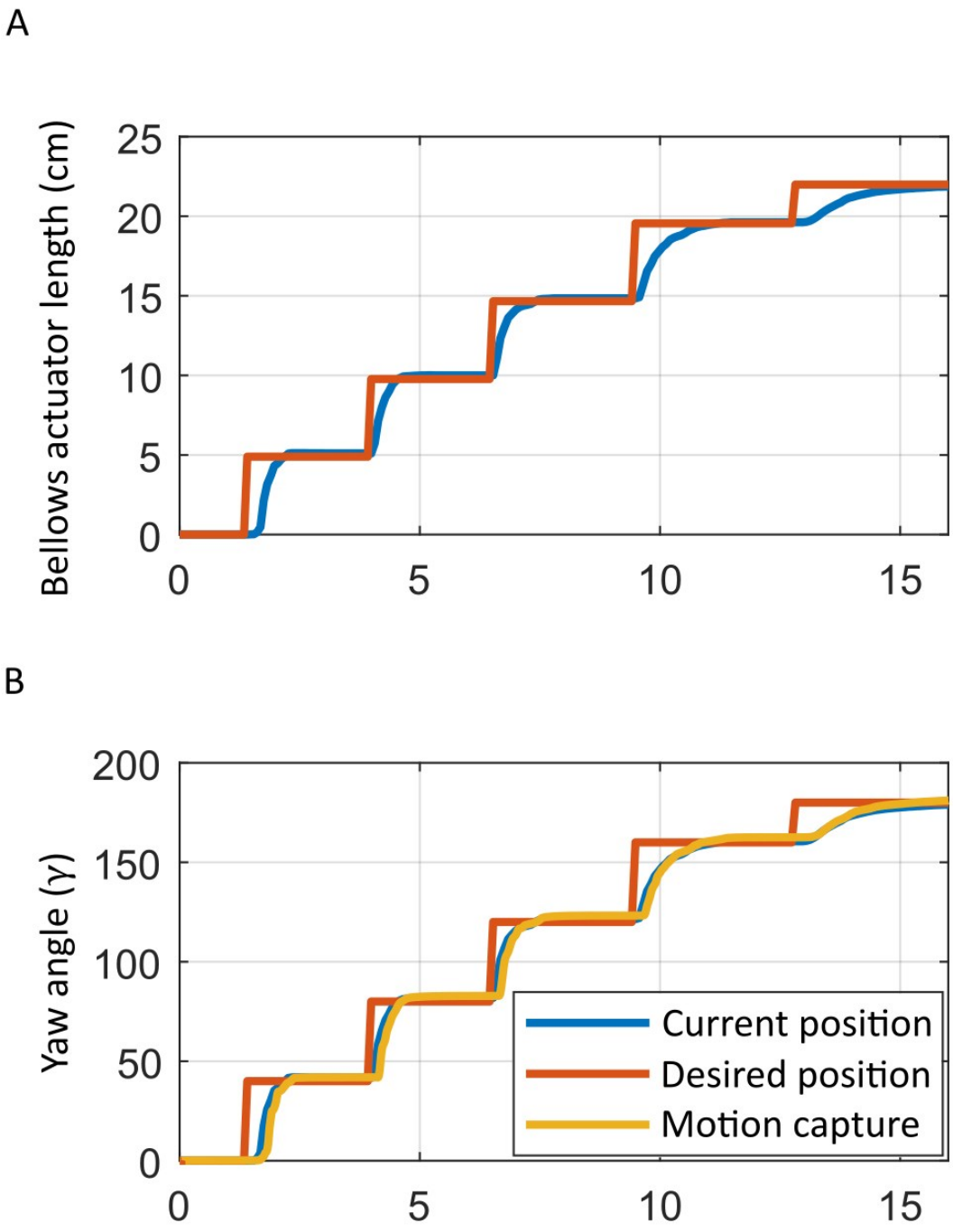

Figure 3. 20. Results from an experiment showing how the true bellows actuator length and actuator's yaw angle measurement are related. (A) results for different actuator length compared to calculated lengths and desired lengths; (B) results for different actuator's yaw angle with measured angles using an IMU sensor; (C) actuator's range of motion.

Next, we tested its motion path to compare to the simulation of the kinematics. The roll-pitch actuator inflated and deflated repeatedly. As shown in Figure 3.19B, the bending motion of the actuator follows a continuous arc based on the kinematics. To measure the end position, a marker was bonded at the center of the roll-pitch actuator. The total height of from its center point to the marker was 3.5 cm. Due to this, a plot is started from 3.5 cm to highest position under 0 to 90 degrees, and also the simulated arc and the real path are not a circle, but an ellipse.

Additionally, desired positions, which represent typical yaw angles on the x-y plane, were selected, and the roll-pitch actuator tracked the trajectory as shown in Figure 3.19C. The experiment was tested under a fixed desired yaw angle of 45°.

In the second experiment in Figure 3.19, the one-DOF revolute actuator was fabricated with a length (L) of 5cm. We then used a motion capture system (Qualysis Miqus M1) to measure the true end effector position. The experiment was performed to test how accurate the actuator controls its position in Figure 3.12. Desired lengths of the bellows actuator are 4.89, 9.77, 14.66, 19.55, and 21.99 (cm). Using an IMU sensor, calculated lengths of the actuator are 5.10, 10.00, 14.84, 19.62, and 21.86 (cm) respectively. Several desired lengths were chosen from 40 to 180 degrees, and a comparison between the modeled system position and the real position is described in Figure 3.20A and B. Compared to the desired and measured lengths, the actuator has a maximum error of 4.3% and a minimum error of 0.36%. Based on the length error, the actuator has between 0.8 and 3.2 degrees of angular error. Additionally, the rise time is slow after the angle exceeds 90 degrees. That is because the elastic property of the fabric causes a large contractile force at large extension distances.

The next experiment in Figure 3.21 was conducted to test the positioning accuracy of the manipulator when multiple modules are connected together. The manipulator for this experiment included two modules: a one-DOF revolute actuator and a two-DOF roll-pitch actuator. We selected the desired yaw(γ) and frame angles (θ) as (γ, θ) = (0°, 45.57°), (120°, 45.57°), (150°, 45.57°), and (90°, 45.57°). According to data we got from the motion capture, the actual yaw angles were 2, 122, 148.4, and 88 degrees, and the actual frame angles were 46.55, 47.16, 43.95, and 44.18 degrees respectively. The results showed that the maximum error of the yaw angle was 2°, the minimum error was 1.6°, the maximum error of the frame angle was 1.62°, and the minimum error of the frame angle was 0.98°.

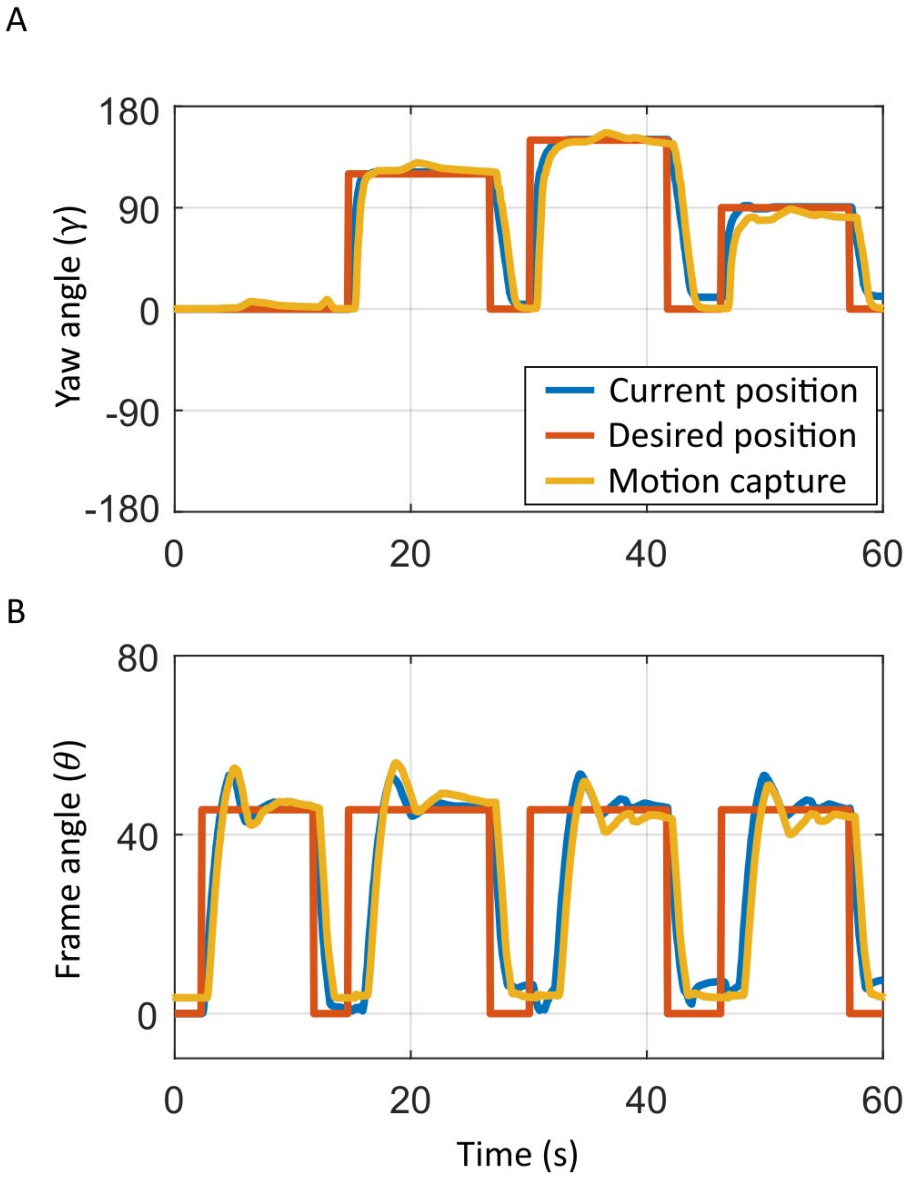

Figure 3. 21. An experimental result to show how well the revolute actuator with joint actuator track positions of desired angles.

In the last experiment (Figure 3.22), a complete manipulator was tested, which contained two roll-pitch actuators, two body sections, and a revolute actuator. We operated the manipulator by forward kinematics. Each module has an IMU sensor on the top surface, and the angles were determined by comparing the IMU readings with those from the previous segment's IMU. Each joint moved to the desired position sequentially. The manipulator moved between four random desired setpoints. Among the four target points, the actuator had errors between 2mm and 1cm.

In addition, we tested the payload capacity of the manipulator. The first roll-pitch actuator was set to 90 degrees of frame angle and the second roll-pitch actuator was set to 0 degrees of frame angle, so that the arm extended horizontally. The first roll-pitch actuator was set under the condition with two actuators were under vacuum and one actuator was controlled using PID control system. External weights were applied to the end effector, a moment arm of 58cm. External payloads caused the end effector’s deformation, and then the control system brought the arm back to its original position. With 165kPa of positive pressure and -62kPa of negative pressure, the manipulator had a maximum payload of 1.3kg. With larger payloads, the body section and the joint actuators buckled.

The kinematic model possibly causes errors. This is because the roll-pitch actuator has ±5% of position error in Figure 3.19B. The IMU sensor also has a small error of ±2° of roll, pitch, and yaw as specified on the datasheet; this leads to the sensor causing an unpredictable error in the system. In addition, four IMU sensors are not aligned perfectly in parallel, so the robot has small angle offsets at every joint.

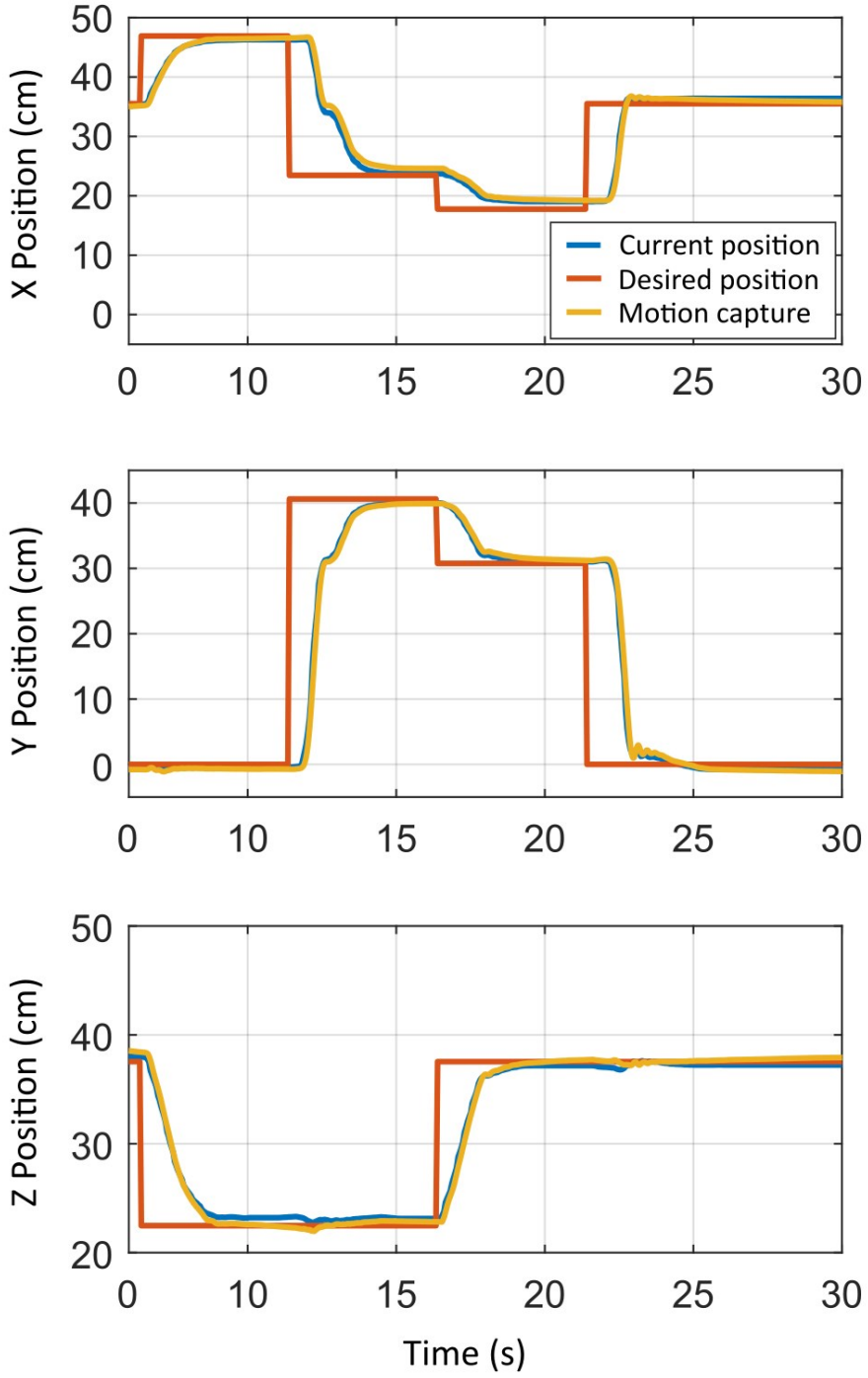

Figure 3. 22. An experiment data from a hybrid manipulator to show its accuracy.

3.8 conclusion

We presented the soft/rigid hybrid robotic system with multiple modules in the paper. The robotic manipulator contains integrated electronics to control its position easily. The modified kinematics and the simple control system with sensors were introduced to provide an opportunity to improve the positioning accuracy and predict soft robot motion. Its kinematics and the control system were demonstrated by a number of experiments. The detailed manufacturing process was also described, so researchers can build robots with differing designs based on these actuator modules. Compared to other soft robotic manipulators (the OctArm VI has a payload of 0.91kg under 551kPa of positive pressure, and the arm has a mass of 6.94kg [116]; the HPN manipulator has a payload of 0.29 kg under 90kPa of positive pressure, while the arm has a mass of 1.5kg [117]), the proposed manipulator has good performance with a 1.3kg payload under 165kPa of positive pressure and 62kPa of negative pressure, and it has a mass of 1.6kg.

Additional work must be done to improve the positioning accuracy and the control system. The control system can be further tuned to minimize errors. Furthermore, additional sensors or more accurate IMUs should be considered to improve the accuracy beyond what is possible with the IMU sensors used in the system.

Chapter 4.

Conclusion

In this paper, we presented a novel fabrication method for creating soft robots and soft/rigid hybrid robots. Two different methods for layered manufactuirng process were introduced, and a method for creating corners or attaching rigid components was present. The fabrication process is simple and fast, and it requires only fabric and TPU film, which are low cost and lightweight. The process can be used for making robots with various sizes and shapes, and the possibility to integrate sensors into the robot body allows for the easy integration of traditional sensors into soft robots.

Among many robotic applications, we presented a soft/rigid hybrid pneumatic manipulator with different modules. We proposed the roll-pitch actuator and designed it to follow a fixed arc in its operating motion. Using the acutator and a new varient of the PCC model, the manipulator achieved high positioning accuracy of the end effector.

Additionally, with the model of the bellows actuator and the roll-pitch actuator, the behavior of the manipualtor and the position of the end effector was predicted.

Future work includes making different inflated shapes such as origami-like structures using corners, folds and the layered fabrication method, understanding the stress concentrations at wrinkles in the seams that causes rupturing, and improving positioning accuracy and control system of the manipulator.

Bibliography

[1] S. Makris, P. Tsarouchi, D. Surdilovic, and J. Krüger, "Intuitive dual arm robot programming for assembly operations," *CIRP Ann. - Manuf. Technol.*, vol. 63, no. 1, pp. 13–16, 2014.

[2] R. Bogue, "Robots in the nuclear industry: a review of technologies and applications," *Ind. Robot An Int. J.*, vol. 38, no. 2, pp. 113–118, 2011.

[3] M. T. Tolley *et al.*, "A Resilient, Untethered Soft Robot," *Soft Robot.*, vol. 1, no. 3, pp. 213–223, 2014.

[4] H. K. Yap *et al.*, "A Fully Fabric-Based Bidirectional Soft Robotic Glove for Assistance and Rehabilitation of Hand Impaired Patients," *IEEE Robot. Autom. Lett.*, vol. 2, no. 3, pp. 1383–1390, 2017.

[5] A. Rafsanjani, Y. Zhang, B. Liu, S. M. Rubinstein, and K. Bertoldi, "Kirigami skins make a simple soft actuator crawl," *Sci. Robot.*, vol. 3, no. 15, p. eaar7555, 2018.

[6] R. F. Shepherd *et al.*, "Multigait soft robot," *Proc. Natl. Acad. Sci.*, vol. 108, no. 51, pp. 20400–20403, 2011.

[7] F. Ilievski, A. D. Mazzeo, R. F. Shepherd, X. Chen, and G. M. Whitesides, "Soft robotics for chemists," *Angew. Chemie*, vol. 123, no. 8, pp. 1930–1935, 2011.

[8] H.-T. Lin, G. G. Leisk, and B. Trimmer, "GoQBot: a caterpillar-inspired soft-bodied rolling robot," *Bioinspir. Biomim.*, vol. 6, no. 2, p. 26007, 2011.

[9] E. Palleau, D. Morales, M. D. Dickey, and O. D. Velev, "Reversible patterning and actuation of hydrogels by electrically assisted ionoprinting," *Nat. Commun.*, vol. 4, p. 2257, 2013.

[10] M. Calisti *et al.*, "An octopus-bioinspired solution to movement and manipulation for soft robots," *Bioinspir. Biomim.*, vol. 6, no. 3, p. 36002, 2011.

[11] P. Polygerinos *et al.*, "Modeling of Soft Fiber-Reinforced Bending Actuators," *IEEE Trans. Robot.*, vol. 31, no. 3, pp. 778–789, Jun. 2015.

[12] A. D. Marchese, R. K. Katzschmann, and D. Rus, "A recipe for soft fluidic elastomer robots," *Soft Robot.*, vol. 2, no. 1, pp. 7–25, 2015.

[13] K. C. Galloway *et al.*, "Soft Robotic Grippers for Biological Sampling on Deep Reefs," *Soft Robot.*, vol. 3, no. 1, pp. 23–33, 2016.

[14] R. V Martinez, C. R. Fish, X. Chen, and G. M. Whitesides, “Elastomeric origami: programmable paper-elastomer composites as pneumatic actuators,” *Adv. Funct. Mater.*, vol. 22, no. 7, pp. 1376–1384, 2012.

[15] M. A. Robertson and J. Paik, “New soft robots really suck: Vacuum-powered systems empower diverse capabilities,” *Sci. Robot.*, vol. 2, no. 9, p. eaan6357, 2017.

[16] B. Gorissen, T. Chishiro, S. Shimomura, D. Reynaerts, M. De Volder, and S. Konishi, “Flexible pneumatic twisting actuators and their application to tilting micromirrors,” *Sensors Actuators A Phys.*, vol. 216, pp. 426–431, 2014.

[17] A. D. Marchese and D. Rus, “Design, kinematics, and control of a soft spatial fluidic elastomer manipulator,” *Int. J. Rob. Res.*, vol. 35, no. 7, pp. 840–869, 2016.

[18] T. Ranzani, G. Gerboni, M. Cianchetti, and A. Menciassi, “A bioinspired soft manipulator for minimally invasive surgery,” 2015.

[19] R. L. Truby *et al.*, “Soft somatosensitive actuators via embedded 3D printing,” *Adv. Mater.*, vol. 30, no. 15, p. 1706383, 2018.

[20] A. J. Veale, S. Q. Xie, and I. A. Anderson, “Characterizing the Peano fluidic muscle and the effects of its material properties on its static and dynamic behavior,” *Smart Mater. Struct.*, vol. 25, no. 6, p. 065014, 2016.

[21] R. Niiyama, X. Sun, L. Yao, H. Ishii, D. Rus, and S. Kim, “Sticky actuator: Free-form planar actuators for animated objects,” in *Proceedings of the Ninth International Conference on Tangible, Embedded, and Embodied Interaction*, 2015, pp. 77–84.

[22] R. Niiyama, X. Sun, C. Sung, B. An, D. Rus, and S. Kim, “Pouch Motors: Printable Soft Actuators Integrated with Computational Design,” *Soft Robot.*, vol. 2, no. 2, pp. 59–70, 2015.

[23] P. M. Khin, H. K. Yap, M. H. Ang, and C.-H. Yeow, “Fabric-based actuator modules for building soft pneumatic structures with high payload-to-weight ratio,” *2017 IEEE/RSJ Int. Conf. Intell. Robot. Syst.*, no. c, pp. 2744–2750, 2017.

[24] J. Ou *et al.*, “aeroMorph - Heat-sealing Inflatable Shape-change Materials for Interaction Design,” *Proc. 29th Annu. Symp. User Interface Softw. Technol. - UIST ’16*, pp. 121–132, 2016.

[25] J.-G. Lee and H. Rodrigue, “Origami-Based Vacuum Pneumatic Artificial Muscles with Large Contraction Ratios,” *Soft Robot.*, 2018.

[26] S. Li, D. M. Vogt, D. Rus, and R. J. Wood, “Fluid-driven origami-inspired artificial muscles,” *Proc. Natl. Acad. Sci.*, vol. 114, no. 50, pp. 13132–13137, 2017.

[27] C. R. Nesler, T. A. Swift, and E. J. Rouse, “Initial design and experimental evaluation of a pneumatic interference actuator,” *Soft Robot.*, vol. 5, no. 2, pp. 138–148, 2018.

[28] J. Chung, R. Heimgartner, C. T. O’Neill, N. S. Phipps, and C. J. Walsh, “ExoBoot, a Soft Inflatable Robotic Boot to Assist Ankle During Walking: Design, Characterization and Preliminary Tests,” in *2018 7th IEEE International Conference on Biomedical Robotics and Biomechatronics (Biorob)*, 2018, pp. 509–516.

[29] P. Polygerinos, Z. Wang, K. C. Galloway, R. J. Wood, and C. J. Walsh, “Soft robotic glove for combined assistance and at-home rehabilitation,” *Rob. Auton. Syst.*, vol. 73, pp. 135–143, 2015.

[30] Z. Zhakypov, M. Falahi, M. Shah, and J. Paik, “The design and control of the multi-modal locomotion origami robot, Tribot,” *IEEE Int. Conf. Intell. Robot. Syst.*, vol. 2015–Decem, pp. 4349–4355, 2015.

[31] P. Polygerinos *et al.*, “Soft Robotics: Review of Fluid-Driven Intrinsically Soft Devices; Manufacturing, Sensing, Control, and Applications in Human-Robot Interaction,” *Adv. Eng. Mater.*, vol. 19, no. 12, 2017.

[32] C. Laschi, B. Mazzolai, and M. Cianchetti, “Soft robotics: Technologies and systems pushing the boundaries of robot abilities,” *Sci. Robot.*, vol. 1, no. 1, p. eaah3690, 2016.

[33] R. V. Martinez *et al.*, “Robotic tentacles with three-dimensional mobility based on flexible elastomers,” *Adv. Mater.*, vol. 25, no. 2, pp. 205–212, 2013.

[34] R. Deimel and O. Brock, “A compliant hand based on a novel pneumatic actuator,” *Proc. - IEEE Int. Conf. Robot. Autom.*, pp. 2047–2053, 2013.

[35] N. W. Bartlett *et al.*, “A 3D-printed, functionally graded soft robot powered by combustion,” *Science (80-.).*, vol. 349, no. 6244, pp. 161–165, 2015.

[36] B. N. Peele, T. J. Wallin, H. Zhao, and R. F. Shepherd, “3D printing antagonistic systems of artificial muscle using projection stereolithography,” *Bioinspir. Biomim.*, vol. 10, no. 5, p. 055003, 2015.

[37] M. Schaffner, J. A. Faber, L. Pianegonda, P. A. Rühs, F. Coulter, and A. R. Studart, “3D printing of robotic soft actuators with programmable bioinspired architectures,” *Nat. Commun.*, vol. 9, no. 1, 2018.

[38] D. Drotman, S. Jadhav, M. Karimi, P. Dezonia, and M. T. Tolley, “3D printed soft actuators for a legged robot capable of navigating unstructured terrain,” *Proc. - IEEE Int. Conf. Robot. Autom.*, pp. 5532–5538, 2017.

[39] C. MacCurdy, R. Katzschmann, Y. Kim, D. Rus, and R. MacCurdy, “Printable Hydraulics: A Method for Fabricating Robots by 3D Co-Printing Solids and Liquids,” *IEEE Int. Conf. Robot. Autom.*, pp. 3878–3885, 2016.

[40] H. Sareen *et al.*, "Printflatables: Printing Human-Scale, Functional and Dynamic Inflatable Objects," in *Proceedings of the 2017 CHI Conference on Human Factors in Computing Systems*, 2017, pp. 3669–3680.

[41] X. Liang, H. Cheong, Y. Sun, J. Guo, C. K. Chui, and C.-H. Yeow, "Design, Characterization, and Implementation of a Two-DOF Fabric-Based Soft Robotic Arm," *IEEE Robot. Autom. Lett.*, vol. 3, no. 3, pp. 2702–2709, 2018.

[42] J. Ou *et al.*, "aeroMorph-Heat-sealing Inflatable Shape-change Materials for Interaction Design," in *Proceedings of the 29th Annual Symposium on User Interface Software and Technology*, 2016, pp. 121–132.

[43] R. F. Natividad, M. R. Del Rosario, P. C. Y. Chen, and C.-H. Yeow, "A hybrid plastic-fabric soft bending actuator with reconfigurable bending profiles," in *Robotics and Automation (ICRA), 2017 IEEE International Conference on*, 2017, pp. 6700–6705.

[44] C. Majidi, "Soft Robotics: A Perspective—Current Trends and Prospects for the Future," *Soft Robot.*, vol. 1, no. 1, pp. 5–11, 2014.

[45] D. Rus and M. T. Tolley, "Design, fabrication and control of soft robots," *Nature*, vol. 521, no. 7553, pp. 467–475, 2015.

[46] A. D. Marchese, K. Komorowski, C. D. Onal, and D. Rus, "Design and control of a soft and continuously deformable 2D robotic manipulation system," *Proc. - IEEE Int. Conf. Robot. Autom.*, pp. 2189–2196, 2014.

[47] D. Yang, M. S. Verma, E. Lossner, D. Stothers, and G. M. Whitesides, "Negative-Pressure Soft Linear Actuator with a Mechanical Advantage," *Adv. Mater. Technol.*, vol. 2, no. 1, 2017.

[48] D. Yang *et al.*, "Buckling Pneumatic Linear Actuators Inspired by Muscle," *Adv. Mater. Technol.*, vol. 1, p. 1600055, 2016.

[49] Y. Mengüç *et al.*, "Wearable soft sensing suit for human gait measurement," *Int. J. Rob. Res.*, vol. 33, no. 14, pp. 1748–1764, 2014.

[50] S. Sareh *et al.*, "Bio-inspired tactile sensor sleeve for surgical soft manipulators," *Proc. - IEEE Int. Conf. Robot. Autom.*, pp. 1454–1459, 2014.

[51] K. Elgeneidy, N. Lohse, and M. Jackson, "Bending angle prediction and control of soft pneumatic actuators with embedded flex sensors – A data-driven approach," *Mechatronics*, vol. 50, no. November 2016, pp. 234–247, 2018.

[52] Y. L. Park, C. Majidi, R. Kramer, P. Brard, and R. J. Wood, "Hyperelastic pressure sensing with a liquid-embedded elastomer," *J. Micromechanics Microengineering*, vol. 20, no. 12, 2010.

[53] Y.-L. Park, B. Chen, and R. J. Wood, “Design and Fabrication of Soft Aftificial Skin using Embedded Microchannels and Liquid Conductors,” *IEEE Sens J.*, vol. 12, no. 8, pp. 2711–2718, 2012.

[54] R. K. Kramer, “Soft electronics for soft robotics,” *Proc. SPIE 9467, Micro-Nanotechnol. Sensors, Syst. Appl. VII*, vol. 9467, p. 946707, 2015.

[55] C. Larson *et al.*, “Highly stretchable electroluminescent skin for optical signaling and tactile sensing,” *Science (80-.).*, vol. 351, no. 6277, pp. 1071–1074, 2016.

[56] L. O. Tiziani, T. W. Cahoon, and F. L. Hammond, “Sensorized pneumatic muscle for force and stiffness control,” *2017 IEEE Int. Conf. Robot. Autom.*, pp. 5545–5552, 2017.

[57] S. Li, D. M. Vogt, D. Rus, and R. J. Wood, “Fluid-driven origami-inspired artificial muscles,” *Proc. Natl. Acad. Sci.*, p. 201713450, 2017.

[58] C. T. O. Neill, N. S. Phipps, L. Cappello, S. Paganoni, and C. J. Walsh, “A Soft Wearable Robot for the Shoulder : Design , Characterization , and Preliminary Testing,” vol. 02129, pp. 1–7, 2017.

[59] C. S. Simpson, A. M. Okamura, and E. W. Hawkes, “Exomuscle: An inflatable device for shoulder abduction support,” *Proc. - IEEE Int. Conf. Robot. Autom.*, pp. 6651–6657, 2017.

[60] E. W. Hawkes, L. H. Blumenschein, J. D. Greer, and A. M. Okamura, “A soft robot that navigates its environment through growth,” *Sci. Robot.*, vol. 2, no. 8, p. eaan3028, 2017.

[61] J. D. Greer, T. K. Morimoto, A. M. Okamura, and E. W. Hawkes, “Series pneumatic artificial muscles (sPAMs) and application to a soft continuum robot,” in *Robotics and Automation (ICRA), 2017 IEEE International Conference on*, 2017, pp. 5503–5510.

[62] L. H. Blumenschein, L. T. Gan, J. A. Fan, A. M. Okamura, and E. W. Hawkes, “A Tip-Extending Soft Robot Enables Reconfigurable and Deployable Antennas,” *IEEE Robot. Autom. Lett.*, vol. 3, no. 2, pp. 949–956, 2018.

[63] N. S. Usevitch, A. Okamura, and E. W. Hawkes, “APAM : Antagonistic Pneumatic Arti cial Muscle,” *IEEE Int. Conf. Robot. Autom.*, 2018.

[64] W. H. Paulsen, “What is the shape of a Mylar balloon?,” *Am. Math. Mon.*, vol. 101, no. 10, pp. 953–958, 1994.

[65] Rohm and Hass, “Thixon 406 Solvent-Based Adhesive Datasheet,” 2006.

[66] “TPU Hot Melt Adhesive Film (#HM65-PA) Datasheet.” [Online]. Available: http://www.perfectex.com/tpuhotmeltadhesivefilm.html.

[67] “Polylactic Acid (PLA) Biopolymer Datasheet.” [Online]. Available: http://www.matweb.com/search/DataSheet.aspx?MatGUID=ab96a4c0655c4018a8785ac4031b9278.

[68] “A. Schulman Matrixx 54S7102 Polycarbonate, FR, 10% Glass Reinforced Datasheet.” [Online]. Available: http://www.matweb.com/search/DataSheet.aspx?MatGUID=b3bb5f10642944e9a729bda36b790d93.

[69] “Extruded Polycarbonate Datasheet.” [Online]. Available: http://www.matweb.com/search/DataSheet.aspx?MatGUID=501acbb63cbc4f748faa7490884cdbca.

[70] “Ensinger Hydex™ 202 Rigid Polyurethane (PU) Datasheet.” [Online]. Available: http://www.matweb.com/search/DataSheet.aspx?MatGUID=893f064e2e6a4648a7571a040627f652.

[71] “Extruded PVC Datasheet.”

[72] “Extruded Acrylonitrile Butadiene Styrene (ABS) Datasheet.” [Online]. Available: http://www.matweb.com/search/DataSheet.aspx?MatGUID=3a8afcddac864d4b8f58d40570d2e5aa.

[73] B. Heinrichs, N. Sepehri, and A. B. Thornton-Trump, “Position-based impedance control of an industrial hydraulic manipulator,” *IEEE Control Syst.*, vol. 17, no. 1, pp. 46–52, 1997.

[74] J. Iqbal, R. U. Islam, S. Z. Abbas, A. A. Khan, and S. A. Ajwad, “Automating industrial tasks through mechatronic systems–A review of robotics in industrial perspective,” *Teh. Vjesn.*, vol. 23, no. 3, pp. 917–924, 2016.

[75] S. Li, S. Chen, B. Liu, Y. Li, and Y. Liang, “Decentralized kinematic control of a class of collaborative redundant manipulators via recurrent neural networks,” *Neurocomputing*, vol. 91, pp. 1–10, 2012.

[76] W. T. Miller, R. P. Hewes, F. H. Glanz, and L. G. Kraft, “Real-time dynamic control of an industrial manipulator using a neural network-based learning controller,” *IEEE Trans. Robot. Autom.*, vol. 6, no. 1, pp. 1–9, 1990.

[77] E. Magrini, F. Flacco, and A. De Luca, “Control of generalized contact motion and force in physical human-robot interaction,” in *Robotics and Automation (ICRA), 2015 IEEE International Conference on*, 2015, pp. 2298–2304.

[78] V. Villani, F. Pini, F. Leali, and C. Secchi, “Survey on human–robot collaboration in industrial settings: Safety, intuitive interfaces and applications,” *Mechatronics*, 2018.

[79] A. M. Zanchettin, N. M. Ceriani, P. Rocco, H. Ding, and B. Matthias, “Safety in human-robot collaborative manufacturing environments: Metrics and control,” *IEEE Trans. Autom. Sci. Eng.*, vol. 13, no. 2, pp. 882–893, 2016.

[80] X. Li, Y. Pan, G. Chen, and H. Yu, “Adaptive Human-Robot Interaction Control for Robots Driven by Series Elastic Actuators.,” *IEEE Trans. Robot.*, vol. 33, no. 1, pp. 169–182, 2017.

[81] H. Yu, S. Huang, G. Chen, Y. Pan, and Z. Guo, “Human–robot interaction control of rehabilitation robots with series elastic actuators,” *IEEE Trans. Robot.*, vol. 31, no. 5, pp. 1089–1100, 2015.

[82] C. Laschi, B. Mazzolai, and M. Cianchetti, “Soft robotics: Technologies and systems pushing the boundaries of robot abilities,” *Sci. Robot.*, vol. 1, no. 1, p. eaah3690, 2016.

[83] P. Polygerinos *et al.*, “Soft robotics: Review of fluid-driven intrinsically soft devices; manufacturing, sensing, control, and applications in human-robot interaction,” *Adv. Eng. Mater.*, vol. 19, no. 12, p. 1700016, 2017.

[84] R. Pfeifer, M. Lungarella, and F. Iida, “The challenges ahead for bio-inspired’soft’robotics,” *Commun. ACM*, vol. 55, no. 11, pp. 76–87, 2012.

[85] B. Gorissen, D. Reynaerts, S. Konishi, K. Yoshida, J. Kim, and M. De Volder, “Elastic Inflatable Actuators for Soft Robotic Applications,” *Adv. Mater.*, vol. 29, no. 43, p. 1604977, 2017.

[86] B. N. Peele, T. J. Wallin, H. Zhao, and R. F. Shepherd, “3D printing antagonistic systems of artificial muscle using projection stereolithography,” *Bioinspir. Biomim.*, vol. 10, no. 5, p. 55003, 2015.

[87] X. Liang, H. K. Yap, J. Guo, R. C. H. Yeow, Y. Sun, and C. K. Chui, “Design and characterization of a novel fabric-based robotic arm for future wearable robot application,” in *Robotics and Biomimetics (ROBIO), 2017 IEEE International Conference on*, 2017, pp. 367–372.

[88] H. K. Yap *et al.*, “A fully fabric-based bidirectional soft robotic glove for assistance and rehabilitation of hand impaired patients,” *IEEE Robot. Autom. Lett.*, vol. 2, no. 3, pp. 1383–1390, 2017.

[89] R. V Martinez *et al.*, “Robotic tentacles with three-dimensional mobility based on flexible elastomers,” *Adv. Mater.*, vol. 25, no. 2, pp. 205–212, 2013.

[90] D. Yang, M. S. Verma, E. Lossner, D. Stothers, and G. M. Whitesides, “Negative-Pressure Soft Linear Actuator with a Mechanical Advantage,” *Adv. Mater. Technol.*, vol. 2, no. 1, p. 1600164, 2017.

[91] S. Sareh *et al.*, “Bio-inspired tactile sensor sleeve for surgical soft manipulators,” *Proc. - IEEE Int. Conf. Robot. Autom.*, pp. 1454–1459, 2014.

[92] D. Rus and M. T. Tolley, “Design, fabrication and control of soft robots,” *Nature*, vol. 521, no. 7553, p. 467, 2015.

[93] R. Deimel and O. Brock, “A compliant hand based on a novel pneumatic actuator,” in *Robotics and Automation (ICRA), 2013 IEEE International Conference on*, 2013, pp. 2047–2053.

[94] P. Polygerinos, Z. Wang, K. C. Galloway, R. J. Wood, and C. J. Walsh, “Soft robotic glove for combined assistance and at-home rehabilitation,” *Rob. Auton. Syst.*, vol. 73, pp. 135–143, 2015.

[95] B. Mosadegh *et al.*, “Pneumatic networks for soft robotics that actuate rapidly,” *Adv. Funct. Mater.*, vol. 24, no. 15, pp. 2163–2170, 2014.

[96] K. C. Galloway, P. Polygerinos, C. J. Walsh, and R. J. Wood, “Mechanically programmable bend radius for fiber-reinforced soft actuators,” in *Advanced Robotics (ICAR), 2013 16th International Conference on*, 2013, pp. 1–6.

[97] M. A. Robertson and J. Paik, “New soft robots really suck: Vacuum-powered systems empower diverse capabilities,” *Sci. Robot.*, vol. 2, no. 9, p. eaan6357, 2017.

[98] Z. Zhakypov, F. Heremans, A. Billard, and J. Paik, “An Origami-Inspired Reconfigurable Suction Gripper for Picking Objects with Variable Shape and Size,” *IEEE Robot. Autom. Lett.*, vol. PP, no. c, pp. 1–1, 2018.

[99] Z. Jiao, C. Ji, J. Zou, H. Yang, and M. Pan, “Vacuum-Powered Soft Pneumatic Twisting Actuators to Empower New Capabilities for Soft Robots,” *Adv. Mater. Technol.*, p. 1800429, 2018.

[100] H. K. Yap, F. Sebastian, C. Wiedeman, and C.-H. Yeow, “Design and characterization of low-cost fabric-based flat pneumatic actuators for soft assistive glove application,” in *Rehabilitation Robotics (ICORR), 2017 International Conference on*, 2017, pp. 1465–1470.

[101] J. H. Low *et al.*, “A bidirectional soft pneumatic fabric-based actuator for grasping applications,” in *2017 IEEE/RSJ International Conference on Intelligent Robots and Systems (IROS)*, 2017, pp. 1180–1186.

[102] L. Cappello *et al.*, “Exploiting textile mechanical anisotropy for fabric-based pneumatic actuators,” *Soft Robot.*, vol. 5, no. 5, pp. 662–674, 2018.

[103] N. S. Usevitch, A. M. Okamura, and E. W. Hawkes, “APAM: Antagonistic Pneumatic Artificial Muscle,” in *2018 IEEE International Conference on Robotics and Automation (ICRA)*, 2018, pp. 1539–1546.

[104] N. Oh, Y. J. Park, S. Lee, H. Lee, and H. Rodrigue, “Design of Paired Pouch Motors for Robotic Applications,” *Adv. Mater. Technol.*, vol. 4, no. 1, p. 1800414, 2019.

[105] W. Park, S. Seo, and J. Bae, “A Hybrid Gripper With Soft Material and Rigid Structures,” *IEEE Robot. Autom. Lett.*, vol. 4, no. 1, pp. 65–72, 2019.

[106] L. Belding *et al.*, "Slit Tubes for Semisoft Pneumatic Actuators," *Adv. Mater.*, vol. 30, no. 9, p. 1704446, 2018.

[107] A. A. Faudzi, N. I. Azmi, M. Sayahkarajy, W. L. Xuan, and K. Suzumori, "Soft manipulator using thin McKibben actuator," in *2018 IEEE/ASME International Conference on Advanced Intelligent Mechatronics (AIM)*, 2018, pp. 334–339.

[108] S. Voisembert, N. Mechbal, A. Riwan, and A. Aoussat, "Design of a novel long-range inflatable robotic arm: Manufacturing and numerical evaluation of the joints and actuation," *J. Mech. Robot.*, vol. 5, no. 4, p. 45001, 2013.

[109] X. Liang, H. K. Yap, J. Guo, R. C. H. Yeow, Y. Sun, and C. K. Chui, "Design and characterization of a novel fabric-based robotic arm for future wearable robot application," *Robot. Biomimetics (ROBIO), 2017 IEEE Int. Conf.*, pp. 367–372, 2017.

[110] A. Stilli, H. A. Wurdemann, and K. Althoefer, "Shrinkable, stiffness-controllable soft manipulator based on a bio-inspired antagonistic actuation principle," in *Intelligent Robots and Systems (IROS 2014), 2014 IEEE/RSJ International Conference on*, 2014, pp. 2476–2481.

[111] J. D. Greer, T. K. Morimoto, A. M. Okamura, and E. W. Hawkes, "Series pneumatic artificial muscles (sPAMs) and application to a soft continuum robot," in *IEEE International Conference on Robotics and Automation*, 2017.

[112] M. Hofer and R. D'Andrea, "Design, Modeling and Control of a Soft Robotic Arm," in *2018 IEEE/RSJ International Conference on Intelligent Robots and Systems (IROS)*, 2018, pp. 1456–1463.

[113] W. Zhang and P. Polygerinos, "Distributed planning of multi-segment soft robotic arms," in *2018 Annual American Control Conference (ACC)*, 2018, pp. 2096–2101.

[114] R. J. Webster III and B. A. Jones, "Design and kinematic modeling of constant curvature continuum robots: A review," *Int. J. Rob. Res.*, vol. 29, no. 13, pp. 1661–1683, 2010.

[115] H. D. Yang and A. T. Asbeck, "A New Manufacturing Process for Soft Robots and Soft/Rigid Hybrid Robots," *2018 IEEE/RSJ Int. Conf. Intell. Robot. Syst.*, 2018.

[116] N. Giri and I. Walker, "Continuum robots and underactuated grasping," *Mech. Sci.*, vol. 2, no. 1, pp. 51–58, 2011.

[117] H. Jiang, X. Liu, X. Chen, Z. Wang, Y. Jin, and X. Chen, "Design and Simulation Analysis of a Soft Manipulator based on Honeycomb Pneumatic Networks," *2016 IEEE Int. Conf. Robot. Biomimetics*, pp. 350–356, 2016.